Synthesis and characterization of high-performance supercapacitor devices based on carbon/MnO_2 composite and carbonized iron cations adsorbed onto polyaniline/nickel graphene foam

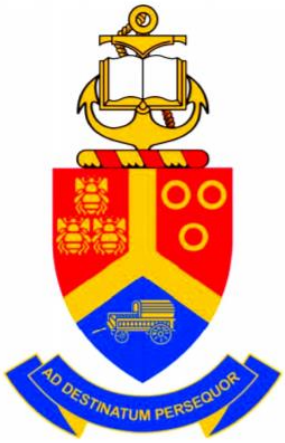

by

Mologadi Nkiyasi Rantho

Submitted in partial fulfilment of the requirements for the degree

DOCTOR OF PHILOSOPHY (Ph.D.)

in the Department of Physics

in the Faculty of Natural and Agricultural Sciences

University of Pretoria

Supervisor/Promoter: Prof. N.I. Manyala

September 2020

Declaration

I, **Mologadi Nkiyasi Rantho** hereby declare that this thesis, which I submit for the **degree of Doctor of Philosophy (Ph.D.)** at the University of Pretoria, is my own work and has not been submitted elsewhere for the award of any degree or diploma.

SIGNATURE STUDENT:_____ DATE:_____

Dedication

Dear God, Almighty, Thank You for helping me achieve this PhD.

Thanks to all my sisters and my husband (Katlego Cassey Nkuna) for the support.

Acknowledgements

I would like to express my profound and deepest appreciation to my supervisor, Prof. N. Manyala, for his efforts to make sure the quality of this work, which included creative ideas and constructive feedback, inspiration, and encouragement.

Many thanks to the sponsors for financial support. The research was funded by the South African Research Chairs Initiative of the Department of Science and Technology, the National Research Foundation (NRF) of South Africa (Grant No. 97994) and financial assistance from the University of Pretoria.

My sincere gratitude to the entire Microscopy Center at the University of Pretoria.

I would like to express my gratitude to Prof. N. Manyala's group members at the University of Pretoria for their help, encouragement, and helpful discussions.

Finally, I would like to thank my husband and my sisters for their help, moral support, devotion, and prayers.

Kind regards

Mologadi Nkiyasi Rantho

ABSTRACT

Due to the increasing demands for energy-storage systems, supercapacitors (SCs) have received significant attention due to their properties/electrochemical performance. Many research papers and technical reports on the development of electrochemical supercapacitors have been published in recent years, inspired by their low specific energy and high production costs. Consequently, research focus in supercapacitors is on improving the specific energy (i.e. ~5-8 Wh kg^{-1}) without compromising its high specific power (i.e. ~5-30 kW kg^{-1}).

In this work, the electrochemical properties of both carbonized iron-polyaniline/nickel graphene foam (C-Fe/PANI/Ni-GF) and birnessite-type MnO_2/carbon composite electrode materials were investigated for supercapacitor applications. The C-Fe/PANI/Ni-GF electrode material was directly synthesized on a current collector by pyrolysis of the iron-PANI mixture coated on nickel graphene foam in a tube furnace under the N_2 atmosphere, and the MnO_2-C electrode material with hierarchical nanostructures was successfully synthesized using $KMnO_4$ solution and spent printing carbon grains method. The structural and morphological characterization of the as-synthesized electrode materials was carried out using scanning electron microscopy (SEM), transmission electron microscopy (TEM), energy-dispersive X-ray spectrometer (EDS), X-ray diffraction (XRD), Raman spectroscopy, and X-ray photoelectron spectroscopy (XPS).

The electrochemical characterization of the as-prepared electrode material was evaluated in both three and two-electrode (i.e. symmetric) cell configurations using 1 M $NaNO_3$ electrolyte. The C-Fe/PANI/Ni-GF symmetric device exhibited a maximum specific energy of 68.0 W h kg^{-1} and specific power of 718.2 W kg^{-1}, at a specific current of 1.0 A g^{-1} and the maximum potential of 1.7 V. The device further displayed long-term cycling stability with capacity retention of 91% over 10 000 galvanostatic charge-discharge cycles at 5 A g^{-1}. The stability of

the device was also tested using the voltage holding and self-discharge approach whereby a slow-discharging process was observed, which suggests the practical application of the device.

To further evaluate the electrochemical performance of C-Fe/PANI/Ni-GF electrode with MnO_2-carbon composites electrode, a hybrid electrochemical supercapacitor device was fabricated based on birnessite-type MnO_2-C composite electrode and C-Fe/PANI/Ni-GF as the positive and negative electrodes, respectively. At the lowest specific current of 1.0 A g^{-1} and cell potential of 2.2 V in 2.5 M KNO_3 electrolyte, the MnO_2-C//C-Fe/PANI/Ni-GF asymmetric device displayed a high specific energy and power of 34.6 W h kg^{-1} and 1100.0 W kg^{-1} respectively. The device further displayed long-term cycling stability with capacitance retention of 98% over 10 000 galvanostatic charge-discharge cycles at 10 A g^{-1}. This device is displaying the overall excellent electrochemical performance.

Table of Contents

List of Figures

List of Tables

SECTION 1

INTRODUCTION

Chapter 1

1.1 Introduction

1.1.1 General background and motivation

The energy demand is increasing rapidly globally; this is due to economic development and population growth. The high energy demand is leading to exhaustion of natural resources. The world economy adopted the transition to alternative energy to meet the high energy demand for socio-economic development, by moving away from non-renewable energy sources to renewable energy sources. Generally, non-renewable energy sources are unsustainable because they will eventually run out; hence we cannot rely on them forever. As they become rare will only lead to rising prices, and the demand continues to remain high, which will become a significant issue sooner or later. However, renewable energy is sustainable and eco-friendly; this include wind, solar, plant biomass energy, hydropower energy, and geothermal energy [1,2]. Figure 1.2 shows the energy diagram of renewable and non-renewable sources.

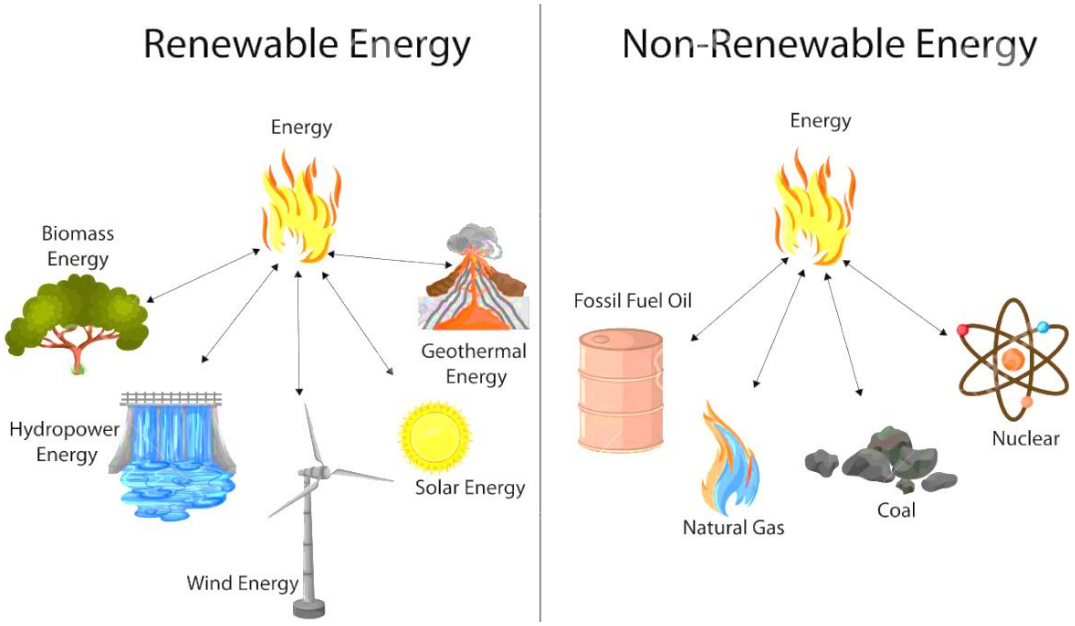

Figure 1.1. *Energy diagram of renewable and non-renewable sources.*

Due to high energy demand, there is currently the development of many exciting renewable energy technologies such as physical, thermal, chemical, mechanical, and electrochemical energy storage systems. Batteries are the most used devices to store energy, but they have disadvantages. These include short life cycles, weak charge/discharge, and low specific power; hence, they do not meet the increasing demands in technological applications. Supercapacitors (SCs), on the other hand, are energy storage devices with a long life cycle, fast charge/discharge, high specific power, although they cannot store as much energy as lithium-ion batteries, SCs can compensate for that with the speed of charge. Therefore, they have the potential capacity to be used as an alternative to batteries for energy storage applications [3–8].

In view of the demands for energy-storage systems, SCs have received great attention due to their electrochemical performance/properties [9]. SCs can be classified into three categories, viz: electric double-layer capacitors (EDLCs), pseudocapacitors or redox SCs, and hybrid capacitors [10–12]. Hybrid capacitor is the combination of both the EDLC and

pseudocapacitive electrode materials to form asymmetric SCs or hybrid systems [12]. Recently, there have been numerous studies/researches on the development of supercapacitors (SCs) due to their low specific energy [4–9,13]. In SCs, the research focus is on increasing the specific energy (i.e., ~5-8 Wh kg^{-1}) without compromising its high-specific power (i.e., ~5-30 kW kg^{-1}) (Figure 1.2). Unlike in rechargeable batteries, which already have a high specific energy in the range of 120-200 Wh kg^{-1}, the focus will be on improving the specific power which is in the range of 0.4-3 kW kg^{-1} [12,14–16].

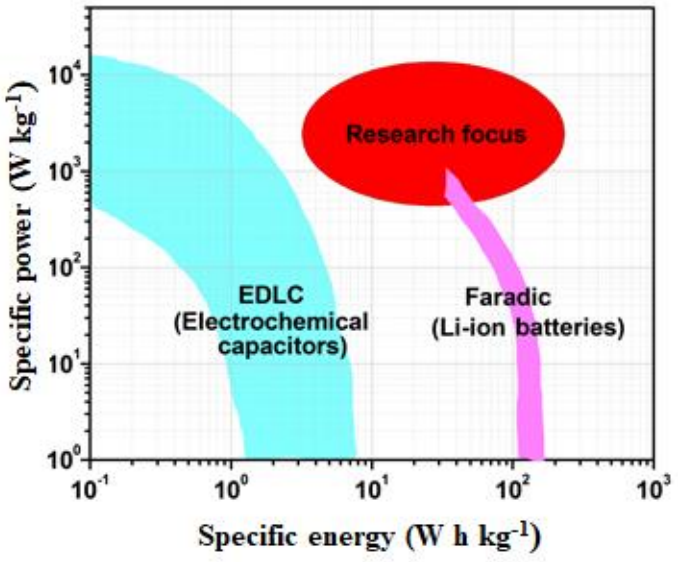

Figure 1.2. *Ragone plot illustrating the relationship between specific energy and specific power for electrochemical capacitors and lithium-ion batteries, including the research focus region [17].*

There are various ways to improve the low specific energy of SCs: (1) by developing new electrode materials. For example, in energy research, the foundation and development of renewable energy conversion and energy storage systems focus on innovative electrode materials for SCs and batteries. These materials are being studied in nano- and micro- scale [11,12]. Since electrode materials in nano- or rather micro-scale for electrochemical energy

storage systems, show an increase in the surface area-to-volume ratio, which leads to an increase in the rate of transport phenomena and a rise in the number of interfaces. Yielding electrodes with much higher specific currents are essential for electrochemical energy conversion [11,12]. Furthermore, the specific energy can also be improved by (2) exploring asymmetric (hybrid) capacitors to increase the operating potential window[10–12], and (2) using battery-electrode materials and the pseudocapacitive electrodes to develop hybrid SCs to exhibit high capacitance [18][19].

In recent reports, conducting polymers are considered as pseudocapacitive materials suitable for the next generation of SCs [13,20–23]. Among these conducting polymers, polyaniline (PANI) has attractive properties, due to its morphological variety, good reversible redox, low cost, and simple synthesis [13,24]. The conducting polymers have a wide range of tunable properties since their conductivity is linked with the molecular structure, the level of doping, and the ordering of molecular packing [13,25–27]. It has been shown that PANI containing iron achieves high electrocatalytic and electrochemical performance with long-cycling stability [13,28–30]. Iron cations easily adsorb onto PANI due to PANI's functional groups, which act as active sites [13,31–34]. Available reports also show that carbon nanotubes can enhance PANI's electrical conduct through π–π interactions [35,36].

Moreover, graphene has attracted great attention due to its remarkable properties, such as high specific surface area, high electrical conductivity, and chemical stability [37–42]. Polymer/graphene interactions (nanocomposites) are expected to exhibit excellent electrochemical performance owing to a stronger π–π conjugation interactions and graphene properties. Yu et al. [43] have reported a remarkably high capacitance value of 1341 F g^{-1} for a PANI/3D graphene framework in an acidic electrolyte. Wang et al. [44] have demonstrated that the PANI/graphene nanocomposites show much better capacitance performance than that

of individual PANI and the synergy effect of PANI and graphene greatly improves the retention life of the composite material. The key factors determining the PANI/graphene nanocomposites' electrochemical performances, such as morphologies, synthesis methods, and synthesis conditions are detailed in the review titled: Polyaniline/graphene nanocomposites towards high-performance supercapacitors by Huang et al. [45].

Among several metal oxides, the birnessite-type manganese dioxide (MnO_2) has been studied extensively for SCs application due to its low cost, naturally abundant, highly redox-active, environmentally friendly; and exhibit high pseudocapacitive performance in aqueous neutral electrolytes [1,46–48]. Despite the high electrochemical performance displayed by MnO_2 in aqueous neutral electrolytes, it has low electrical conductivity resulting in low cycling stability [47,49]. The low cycling stability of the MnO_2 is improved by using carbon-based materials with excellent conductivity as support during MnO_2 synthesis [50–53].

1.1.2 Aim and objectives

The aim and objectives of the study are divided into two sections:

Section 1:

The study is aimed at structural, composition, and morphological characterization of the as-synthesized electrode material, and the electrochemical properties of carbonized iron-polyaniline/nickel graphene foam (C-Fe/PANI/Ni-GF) symmetric device.

Section 2:

Although studies about birnessite-type MnO_2-based materials as the positive electrode and activated carbon (AC) as negative electrode have been reported in the literature there are rare studies done on C-Fe/PANI/Ni-GF as a negative electrode. In this work, we report on a hybrid

electrochemical supercapacitor device based on birnessite-type MnO_2-C composite as the positive electrode and C-Fe/PANI/Ni-GF as a negative electrode. This study is aimed at the structural and morphological characterization of the as-synthesized electrode materials and the electrochemical properties of MnO_2-C//C-Fe/PANI/Ni-GF asymmetric device.

The objectives are:

i. Synthesis of C-Fe/PANI/Ni-GF by pyrolysis of the iron-PANI mixture coated on nickel graphene foam in a tube furnace under the N_2 atmosphere.
ii. Synthesis of MnO_2-C with hierachical nanostructures using $KMnO_4$ solution and spent printing carbon grains.
iii. Structural and morphological characterization of the as-synthesized samples using X-ray diffraction (XRD), Raman spectrometer, scanning electron microscopy (SEM), energy-dispersive X-ray spectrometer (EDS), transmission electron microscopy (TEM) and X-ray photoelectron spectroscopy (XPS).
iv. Electrochemical characterization of the active electrodes using Biologic VMP-300 potentiostat (Knoxville TN 37,930, USA) controlled by the EC-Lab V10.37 software at room temperature.

1.1.3 Outline of the thesis

Chapter 1: It presents the general introduction of energy storage systems, the aim, and the objectives of the study.

Chapter 2: It presents a literature overview of supercapacitors.

Chapter 3: The synthesized materials that were investigated in this study were characterized using various techniques, namely, XRD, Raman spectroscopy, SEM, EDS, TEM, and XPS, and this chapter presents an introductory overview of these techniques. This chapter also describes the experimental procedures and techniques used for the synthesis and characterizations of as-synthesized materials. The first section of this chapter focuses on the characterization of C-Fe/PANI/Ni-GF and the symmetric device's electrochemical properties based on C-Fe/PANI/Ni-GF. The last section of this chapter focuses on the synthesis of MnO_2-C and C-Fe/PANI/Ni-GF, and the characterization of the as-synthesized electrodes. This includes the fabrication and electrochemical properties of the asymmetric supercapacitor (MnO_2-C//C-Fe/PANI/Ni-GF) based on MnO_2-C nanosheets as a positive electrode and C-Fe/PANI/Ni-GF as a negative electrode.

Chapter 4: Presents results and a detailed discussion of the results obtained in this work.

Chapter 5: Presents a summary of the research and recommendations for future work.

REFERENCES

[1] L. Demarconnay, E. Raymundo-Piñero, F. Béguin, Adjustment of electrodes potential window in an asymmetric carbon/MnO_2 supercapacitor, J. Power Sources. 196 (2011) 580–586. doi:10.1016/j.jpowsour.2010.06.013.

[2] F.O. Ochai-Ejeh, M.J. Madito, D.Y. Momodu, A.A. Khaleed, O. Olaniyan, N. Manyala, High performance hybrid supercapacitor device based on cobalt manganese layered double hydroxide and activated carbon derived from cork (Quercus Suber), Electrochim. Acta. 252 (2017) 41–54. doi:10.1016/j.electacta.2017.08.163.

[3] P. Anastas, N. Eghbali, Green Chemistry: Principles and Practice, Chem. Soc. Rev. 39 (2010) 301–312. doi:10.1039/b918763b.

[4] E. Frackowiak, Carbon materials for supercapacitor application, Phys. Chem. Chem. Phys. 9 (2007) 1774. doi:10.1039/b618139m.

[5] L.L. Zhang, X.S. Zhao, Carbon-based materials as supercapacitor electrodes, Chem. Soc. Rev. 38 (2009) 2520. doi:10.1039/b813846j.

[6] H. Pan, J. Li, Y.P. Feng, Carbon Nanotubes for Supercapacitor, Nanoscale Res. Lett. 5 (2010) 654–668. doi:10.1007/s11671-009-9508-2.

[7] E. Frackowiak, F. Béguin, Carbon materials for the electrochemical storage of energy in capacitors, Carbon N. Y. 39 (2001) 937–950. doi:10.1016/S0008-6223(00)00183-4.

[8] S.W. Zhang, G.Z. Chen, Manganese oxide based materials for supercapacitors, Energy Mater. 3 (2008) 186–200. doi:10.1179/174892409X427940.

[9] S. Mondal, U. Rana, S. Malik, Reduced Graphene Oxide/Fe_3O_4/Polyaniline Nanostructures as Electrode Materials for an All-Solid-State Hybrid Supercapacitor, J. Phys. Chem. C. 121 (2017) 7573–7583. doi:10.1021/acs.jpcc.6b10978.

[10] G. Zhang, M. Kong, Y. Yao, L. Long, M. Yan, One-pot synthesis of γ -MnS / reduced graphene oxide with enhanced performance for aqueous asymmetric supercapacitors, Nanotechnology 28 (2017) 065402. https://doi.org/10.1088/1361-6528/aa52a5.

[11] G. Feng, S. Li, V. Presser, P.T. Cummings, Molecular Insights into Carbon Supercapacitors Based on Room-Temperature Ionic Liquids, J. Phys. Chem. Lett. 4 (2013) 3367–3376. https://doi.org/10.1021/jz4014163.

[12] P. Simon, Y. Gogotsi, Materials for electrochemical capacitors, Nat. Mater. 7 (2008) 845–854. https://doi.org/10.1142/9789814287005_0033.

[13] M.N. Rantho, M.J. Madito, N. Manyala, High-performance symmetric supercapacitor device based on carbonized iron-polyaniline / nickel graphene foam, J. Alloys Compd. 819 (2019) 152993. https://doi.org/10.1016/j.jallcom.2019.152993.

[14] X. Rui, H. Tan, Q. Yan, Nanostructured metal sulfides for energy storage, Nanoscale. 6 (2014) 9889. https://doi.org/10.1039/C4NR03057E.

[15] B.E. Conway, Electrochemical Supercapacitors Scientific Fundamentals and Technological Applications 1999.pdf, Kluwer Academic/Plenum: New York, 1999.

[16] J.R.J. Miller, A.F.A. Burke, Electrochemical capacitors: challenges and opportunities for real-world applications, Electrochem. Soc. Interface. 17 (2008) 53.

[17] Mologadi Nkiyasi Rantho, Synthesis and characterization of vanadium disulfide nanosheets and carbonized iron cations adsorbed onto polyaniline for high-perfomance supercapacitor applications,Masters dessertation, University of Pretoria, (2017.

[18] W. Zuo, R. Li, C. Zhou, Y. Li, J. Xia, J. Liu, Battery-Supercapacitor Hybrid Devices : Recent Progress and Future Prospects, Adv. Sci. 4 (2017) 1–21. https://doi.org/10.1002/advs.201600539.

[19] F. Wang, X. Wu, X. Yuan, Z. Liu, Latest advances in supercapacitors: From new electrode materials to novel device designs, Chem. Soc. Rev. 46 (2017) 6816–6854. https://doi.org/10.1039/c7cs00205j.

[20] G. Wang, L. Zhang, J. Zhang, A review of electrode materials for electrochemical supercapacitors, Chem. Soc. Rev. 41 (2012) 797–828. https://doi.org/10.1039/C1CS15060J.

[21] K. Lota, V. Khomenko, E. Frackowiak, Capacitance properties of poly(3,4-ethylenedioxythiophene)/carbon nanotubes composites, J. Phys. Chem. Solids. 65 (2004) 295–301. https://doi.org/10.1016/J.JPCS.2003.10.051.

[22] J.Y. Kim, K.H. Kim, K.B. Kim, Fabrication and electrochemical properties of carbon nanotube/polypyrrole composite film electrodes with controlled pore size, J. Power Sources. 176 (2008) 396–402. https://doi.org/10.1016/J.JPOWSOUR.2007.09.117.

[23] I. Shown, A. Ganguly, L.-C. Chen, K.-H. Chen, Conducting polymer-based flexible supercapacitor, Energy Sci. Eng. 3 (2015) 2–26. https://doi.org/10.1002/ese3.50.

[24] X. Wang, J. Deng, X. Duan, D. Liu, J. Guo, P. Liu, Crosslinked polyaniline nanorods with improved electrochemical performance as electrode material for supercapacitors, J. Mater. Chem. A. 2 (2014) 12323. https://doi.org/10.1039/C4TA02231A.

[25] G. Giri, E. Verploegen, S.C.B. Mannsfeld, S. Atahan-Evrenk, D.H. Kim, S.Y. Lee, H.A. Becerril, A. Aspuru-Guzik, M.F. Toney, Z. Bao, Tuning charge transport in solution-sheared organic semiconductors using lattice strain, Nature. 480 (2011) 504–508. https://doi.org/10.1038/nature10683.

[26] G. Sabouraud, S. Sadki, N. Brodie, Guillaume Sabouraud, The mechanisms of pyrrole electropolymerization, Chem. Soc. Rev. 29 (2000) 283–293.

https://doi.org/10.1039/a807124a.

[27] D. Li, J. Huang, R.B. Kaner, Polyaniline Nanofibers: A Unique Polymer Nanostructure for Versatile Applications, Acc. Chem. Res. 42 (2009) 135–145. https://doi.org/10.1021/ar800080n.

[28] H. Mi, X. Zhang, X. Ye, S. Yang, Preparation and enhanced capacitance of core–shell polypyrrole/ polyaniline composite electrode for supercapacitors, J. Power Sources. 176 (2008) 403–409. https://doi.org/10.1016/j.jpowsour.2007.10.070.

[29] C. Portet, P.L. Taberna, P. Simon, E. Flahaut, C. Laberty-Robert, High power density electrodes for Carbon supercapacitor applications, Electrochim. Acta. 50 (2005) 4174–4181. https://doi.org/10.1016/j.electacta.2005.01.038.

[30] M.N. Rantho, M.J. Madito, N. Manyala, Symmetric supercapacitor with supercapattery behavior based on carbonized iron cations adsorbed onto polyaniline, Electrochim. Acta. 262 (2018) 82-96. https://doi.org/10.1016/j.electacta.2018.01.001.

[31] B. Yanwu Zhu, S. Murali, W. Cai, X. Li, J. Won Suk, J.R. Potts, R.S. Ruoff, Y. Zhu, S. Murali, W. Cai, X. Li, J.W. Suk, J.R. Potts, R.S. Ruoff, Graphene and Graphene Oxide: Synthesis, Properties, and Applications, Adv. Mater. 22 (2010) 3906–3924. https://doi.org/10.1002/adma.201001068.

[32] J. Wang, B. Deng, H. Chen, X. Wang, J. Zheng, Removal of Aqueous Hg(II) by Polyaniline: Sorption Characteristics and Mechanisms, Environ. Sci. Technol. 43, 14 (2009) 5223–5228. https://doi.org/10.1021/es803710k.

[33] J. Zhang, C. Liu, G. Shi, Raman spectroscopic study on the structural changes of polyaniline during heating and cooling processes, J. Appl. Polym. Sci. 96 (2005) 732–739. https://doi.org/10.1002/app.21520.

[34] M. Sawangphruk, M. Suksomboon, K. Kongsupornsak, J. Khuntilo, P. Srimuk, Y. Sanguansak, P. Klunbud, P. Suktha, P. Chiochan, High-performance supercapacitors based on silver nanoparticle–polyaniline–graphene nanocomposites coated on flexible carbon fiber paper, J. Mater. Chem. A. 1 (2013) 9630. https://doi.org/10.1039/c3ta12194a.

[35] Q. Yao, L. Chen, W. Zhang, S. Liufu, X. Chen, Enhanced Thermoelectric Performance of Single-Walled Carbon Nanotubes/Polyaniline Hybrid Nanocomposites, ACS Nano. 4 (2010) 2445–2451. https://doi.org/10.1021/nn1002562.

[36] Q. Wang, Q. Yao, J. Chang, L. Chen, Enhanced thermoelectric properties of CNT/PANI composite nanofibers by highly orienting the arrangement of polymer chains, J. Mater. Chem. 22 (2012) 17612. https://doi.org/10.1039/c2jm32750c.

[37] H. Huang, J. Zhang, L. Jiang, Z. Zang, Preparation of cubic Cu2O nanoparticles wrapped by reduced graphene oxide for the efficient removal of rhodamine B, J. Alloys Compd. 718 (2017) 112–115. https://doi.org/10.1016/j.jallcom.2017.05.132.

[38] X. Liu, T. Xu, Y. Li, Z. Zang, X. Peng, H. Wei, W. Zha, F. Wang, Enhanced X-ray photon response in solution-synthesized CsPbBr 3 nanoparticles wrapped by reduced graphene oxide, Sol. Energy Mater. Sol. Cells. 187 (2018) 249-254. https://doi.org/10.1016/j.solmat.2018.08.009.

[39] C. Lee, X. Wei, J.W. Kysar, J. Hone, of Monolayer Graphene, (2008).

[40] B.Z.J.Æ.A. Zhamu, Processing of nanographene platelets (NGPs) and NGP nanocomposites : a review, (2008) 5092–5101. https://doi.org/10.1007/s10853-008-2755-2.

[41] M.J. Madito, A. Bello, J.K. Dangbegnon, C.J. Oliphant, W.A. Jordaan, D.Y. Momodu,

T.M. Masikhwa, F. Barzegar, M. Fabiane, N. Manyala, atmospheric pressure chemical vapour deposition A dilute Cu (Ni) alloy for synthesis of large-area Bernal stacked bilayer graphene using atmospheric pressure chemical vapour deposition, J. Appl. Phys., (2016) 015306. https://doi.org/10.1063/1.4939648.

[42] K. S. Novoselov, A. K. Geim, S. V. Morozov, D. Jiang, Y. Zhang, S. V. Dubonos, I. V. Grigorieva, A. A. Firsov, Electric Field Effect in Atomically Thin Carbon Films, Science, (2004) 666-669. doi:10.1126/science.1102896 .

[43] M. Yu, Y. Huang, C. Li, Y. Zeng, W. Wang, Y. Li, P. Fang, X. Lu, Y. Tong, Building Three-Dimensional Graphene Frameworks for Energy Storage and Catalysis, Adv. Funct. Mater. 25 (2015) 324–330. https://doi.org/10.1002/adfm.201402964.

[44] H. Wang, Q. Hao, X. Yang, L. Lu, X. Wang, A nanostructured graphene/polyaniline hybrid material for supercapacitors, Nanoscale. 2 (2010) 2164. https://doi.org/10.1039/c0nr00224k.

[45] Z. Huang, L. Li, Y. Wang, C. Zhang, T. Liu, Polyaniline/graphene nanocomposites towards high-performance supercapacitors: A review, Compos. Commun. 8 (2018) 83–91. https://doi.org/10.1016/J.COCO.2017.11.005.

[46] M. Huang, Y. Zhang, F. Li, L. Zhang, R.S. Ruoff, Z. Wen, Q. Liu, Self-assembly of mesoporous nanotubes assembled from interwoven ultrathin birnessite-type MnO_2 nanosheets for asymmetric supercapacitors., Sci. Rep. 4 (2014) 3878. https://doi.org/10.1038/srep03878.

[47] L. Li, Z.A. Hu, N. An, Y.Y. Yang, Z.M. Li, H.Y. Wu, Facile Synthesis of MnO_2 /CNTs Composite for Supercapacitor Electrodes with Long Cycle Stability, J. Phys. Chem. C. 118 (2014) 22865–22872. https://doi.org/10.1021/jp505744p.

[48] T. Brousse, P.L. Taberna, O. Crosnier, R. Dugas, P. Guillemet, Y. Scudeller, Y. Zhou, F. Favier, D. Bélanger, P. Simon, Long-term cycling behavior of asymmetric activated carbon/MnO_2 aqueous electrochemical supercapacitor, J. Power Sources. 173 (2007) 633–641. https://doi.org/10.1016/j.jpowsour.2007.04.074.

[49] Y. Jin, H. Chen, M. Chen, N. Liu, Q. Li, Graphene-Patched CNT/MnO_2 Nanocomposite Papers for the Electrode of High-Performance Flexible Asymmetric Supercapacitors, ACS Appl. Mater. Interfaces. 5 (2013) 3408–3416. https://doi.org/10.1021/am400457x.

[50] D. Gueon, J.H. Moon, MnO_2 Nanoflake-Shelled Carbon Nanotube Particles for High-Performance Supercapacitors, ACS Sustain. Chem. Eng. 5 (2017) 2445–2453. https://doi.org/10.1021/acssuschemeng.6b02803.

[51] B. Brown, I.A. Cordova, C.B. Parker, B.R. Stoner, J.T. Glass, Optimization of Active Manganese Oxide Electrodeposits Using Graphenated Carbon Nanotube Electrodes for Supercapacitors, Chem. Mater. 27 (2015) 2430–2438. https://doi.org/10.1021/cm504519m.

[52] J. Jiang, Y. Li, J. Liu, X. Huang, C. Yuan, X.W.D. Lou, Recent Advances in Metal Oxide-based Electrode Architecture Design for Electrochemical Energy Storage, Adv. Mater. 24 (2012) 5166–5180. https://doi.org/10.1002/adma.201202146.

[53] G. Lota, K. Fic, E. Frackowiak, Carbon nanotubes and their composites in electrochemical applications, Energy Environ. Sci. 4 (2011) 1592. https://doi.org/10.1039/c0ee00470g.

SECTION 2

LITERATURE OVERVIEW

Chapter 2

Literature overview

2.1 Introduction

This chapter presents a literature overview of supercapacitors (SCs), principles of charge storage mechanism in SCs, electrode and electrolyte materials for supercapacitor applications and electrochemical device fabrication are reviewed. A brief discussion on the testing, fabrication of an electrochemical cell and evaluating electrode materials for SCs is also given.

2.2 Supercapacitors (SCs)

Supercapacitors (SCs), also known as electrochemical capacitors (ECs) have attracted considerable interest as the important application in the area of electrochemical energy storage because of increasing demand for digital communication, electric vehicles and other electronic devices at high pulse power level [1–3]. However, SCs, unlike conventional batteries, are high power-delivery storage devices that can charge-discharge in a shorter time by exploiting their fast surface or near-surface reactions [4–7]. Even though SCs have high specific power, they have low specific energy compared to rechargeable batteries [4,8]. Since SCs have high specific power, the research focuses on improving their specific energy, and rechargeable batteries, on the other hand, have high specific energy, the research focuses on enhancing their specific power [4–6,9]. The specific energy of SCs can be increased by increasing the operating voltage by exploring hybrid systems, exploring high-voltage electrolytes and new electrode materials. Figure 2.1 shows the Ragone plot with the difference in specific energy and specific power for various energy storage systems.

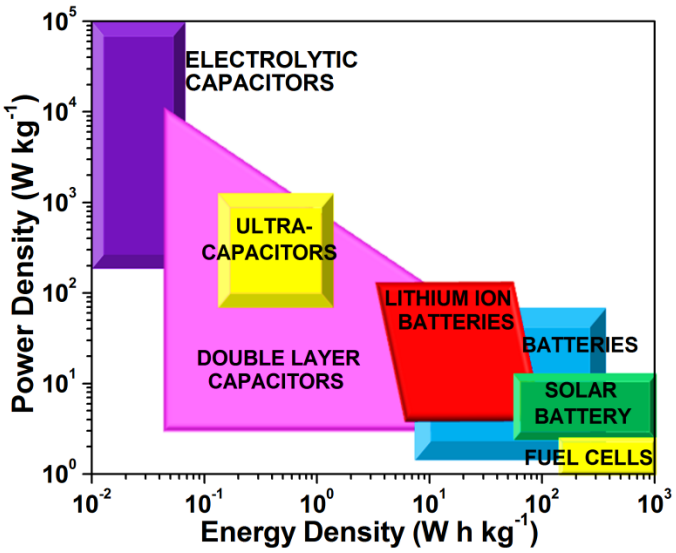

Figure 2.1. *Illustration of Ragone plot relating specific energy versus specific power for different energy storage systems [10].*

2.3 Principle of energy storage in supercapacitors

The SCs can be divided into three categories based on charge storage mechanism, also the type of material used, the electrolyte, or the device fabrication [4,8,11–13], i.e.:

i. Electric double-layer capacitors (EDLCs)

ii. Pseudocapacitors

iii. Hybrid capacitors

An illustration of the categories of SCs based on the charge storage mechanism is presented in Figure 2.2.

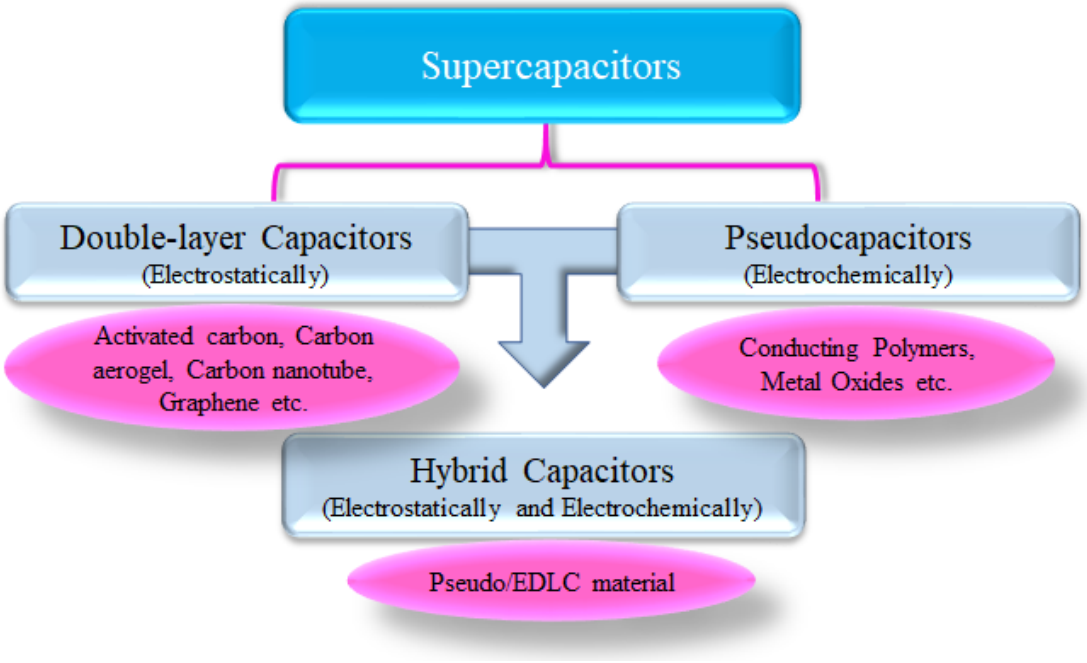

Figure 2.2. *The classification of supercapacitors is based on the charge storage mechanism.*

2.3.1 Electric double-layer capacitors (EDLCs)

The EDLCs is the type of supercapacitor charge storage mechanism that store energy electrostatically and is generally attained by double-layer capacitance. In this charge storage mechanism, there is no transfer of charges across the electrode/electrolyte interface. This implies that during the charging process, the electrons travel from the negative electrode to the positive electrode through an external circuit, and during the discharging process, the reverse process take place. SCs consist of a positive and negative electrode, a separator, and an electrolyte (see figure 2.3). In general, the potential applied to the negative electrode in the EDLC cell attracts the positive ions in the electrolyte; likewise, if the same potential is applied to the positive electrode, it attracts the negative ions. The typical electrodes used in EDLCs are carbon materials and are separated by a dielectric separator, the electronic conductivity, but only ionic conductivity is allowed [14]. Separation of charges occurs after

polarization at the EDLC generating electrode/electrolyte interface. As a result, the EDLCs store charges at the electrode/electrolyte interface based on pure electrostatic charge accumulation, as shown in Figure 2.3 [14]. Hence, this interface can be seen as a capacitor with an electrical double-layer capacitance, which can be expressed as [14]:

$$C = \frac{A\varepsilon}{4\pi d} \tag{1}$$

where A is the surface area of the electrode, ε is the medium (electrolyte) dielectric constant ($\varepsilon = 1$ for a vacuum and $\varepsilon > 1$ for all other materials), and d is the effective thickness of the electrical double layer.

From equation 1 it can be shown that the electrodes with high surface area and high porosity may have a high capacitance hence EDLCs store a very large amount of energy, due to the porous surface structure of the electrode, the composition of the electrolyte and the potential field between the interface charges [14].

The mechanism for storing energy does not involve a chemical reaction in EDLCs. The EDLCs are electrochemically stable due to the physical and highly reversible energy-storage process. on the movement of ions hence the EDLCs can store and release energy faster than batteries that relies on slower chemical reactions. Consequently, in EDLCs, the amount of charge and discharging process depends only on the movement of ions so that the EDLCs can store and release energy faster than the batteries that rely on slower chemical reactions.

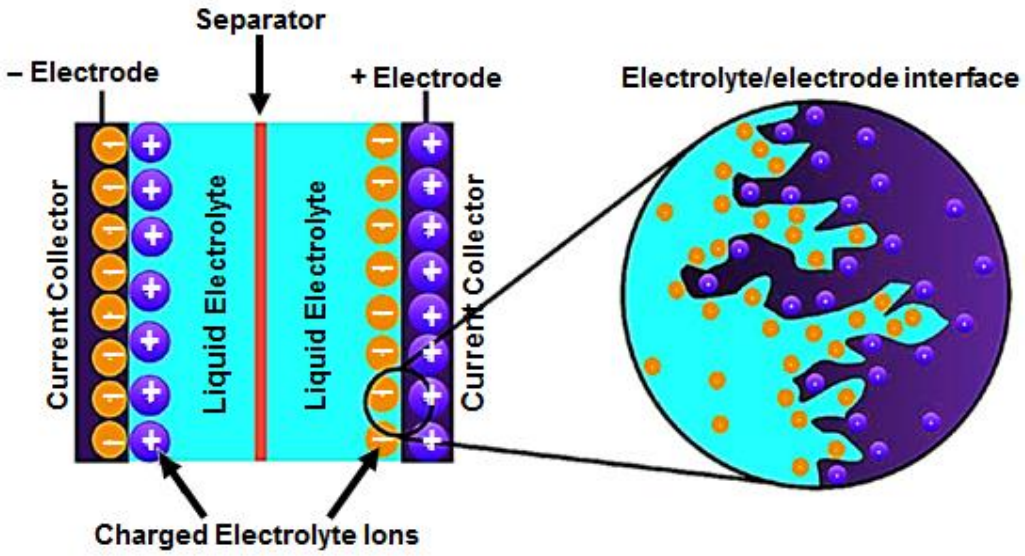

Figure 2.3. *Schematic illustration of energy storage mechanism in EDLCs [10].*

2.3.2 Pseudocapacitors

Pseudocapacitors are supercapacitors that store energy electrochemically. The electrical energy in pseudocapacitors is stored faradaically by electron charge transfer between electrode and electrolyte. This is accomplished through reduction-oxidation reactions (redox reactions), electro-sorption processes, and intercalation processes (see figure 2.4) [4]. Underpotential deposition describes the formation of a monolayer of the adsorbed surface from ions contained within the electrolyte on the electrode composed of various metals with redox potential [4]. The electrochemical adsorption of ions to the surface or near the surface of an electrode material is defined as redox pseudocapacitance accompanied by a related faradaic charge transfer. In contrast, pseudocapacitance intercalation arises from the intercalation of ions into the layers or pores of pseudocapacitive materials accompanied by a faradaic transfer of charge without any change in the crystallographic phase [4]. Pseudocapacitors typically fill the void between batteries and double layer capacitors and can charge and discharge from seconds to

minutes. Their main advantage is that while running much quicker, they can carry as much charge as other batteries.

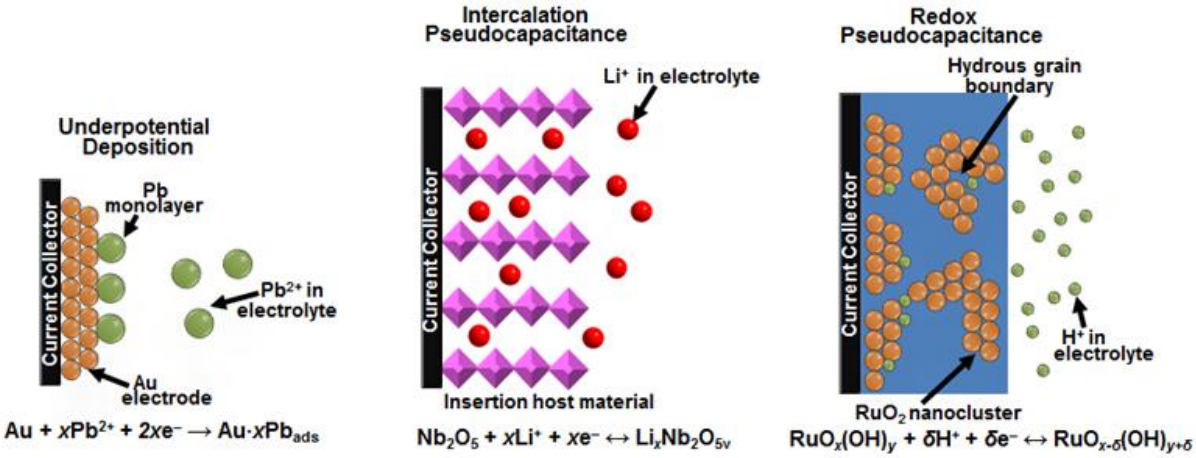

Figure 2.4. *Different types of reversible redox mechanisms that give rise pseudocapacitors.*

2.3.3 Hybrid capacitors

Other than capacitance, the other two important parameters of the supercapacitor are its specific energy and specific power. Faradaic materials have high specific energy but lower specific power compared to EDLCs which have a high specific power, but lower specific energy due to discharging energy faster than batteries and the active surface redox reaction. To achieve high electrochemical performance (e.g., high specific energy and specific power) hybrid capacitors are the way to go because they integrate both EDLC and pseudocapacitive energy storage mechanisms. Generally, hybrid capacitors refer to the combination of both EDLC and pseudocapacitive electrode materials to form asymmetric SCs or hybrid systems. In hybrid capacitors, both EDLC and pseudocapacitive mechanisms co-exist.

In these mechanisms, the electrode materials' essential properties are high conductivity, an appropriate pore-size distribution, and specific large surface area. Hybrid capacitors can also

be fabricated using two different mixed metal oxide or doped conducting polymer materials. For instance, a composite hybrid capacitor consists of an electrode fabricated from a carbon material incorporated into a conducting polymer or metal oxide material. Moreover, it can also be fabricated using the EDLC-type material as a negative electrode and pseudocapacitive-type material as a positive electrode (i.e., asymmetric capacitor). Therefore, hybrid capacitors can be categorized into three classes: battery-type, composites, and asymmetric hybrids [4,8,11] as shown in figure 2.5 below.

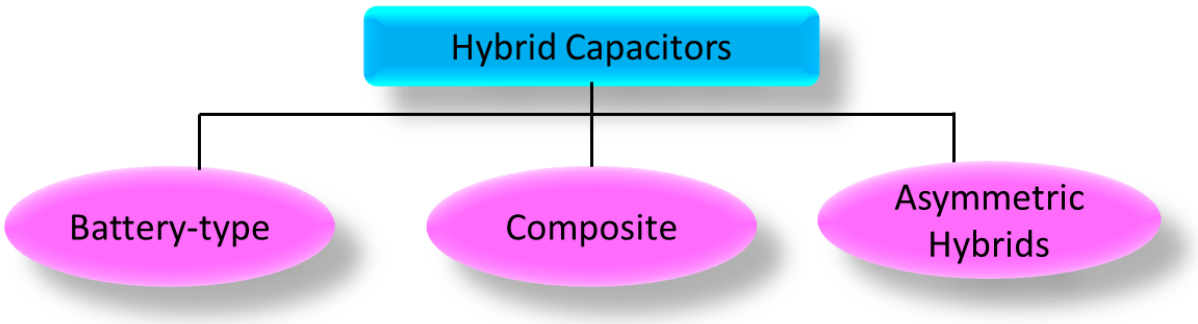

Figure 2.5. *The categorization of hybrid capacitors into three types according to their design and working mechanism.*

The hybrid battery-type is a combination of two different electrodes (supercapacitor electrode with battery electrode). This system has been set up to use both supercapacitors and batteries properties in a single cell. The Composite electrodes combine carbon-based materials in one electrode with either metal oxides or conducting polymer. Asymmetric hybrid on the other hand is the combination of non-faradic and Faradic processes with a Pseudocapacitors electrode through coupling and EDLC. They are set up in such a way as to use the carbon material as a negative electrode, while either metal oxide or polymer as a positive electrode. Typically, the charge-discharge characteristics of hybrid capacitors are nonlinear.

2.4 Electrode material for supercapacitor

SCs consists of three essential components, viz., electrode, electrolyte, and the separator as seen in figure 2.3. In SCs, the electrode material plays an important role in determining the energy and power of supercapacitors. Its electrochemical performances strongly depend on surface area, electrical conductivity, wetting of electrode, and permeability of electrolyte solutions. There have been large number of research studies on electrode materials of SCs which includes: (1) Carbon materials, (2) Conducting polymers, and (3) Metal oxides/hydroxides [15–31].

Carbon materials are widely employed as the electrode materials for SCs owing to their low cost and versatile existing forms (e.g., powders, fibers, felts, composites, mats, monoliths, and foils), good electronic conductivity, high chemical stability, high specific surface area and wide operating temperature range [32,33]. In carbon materials, the energy is stored by an electrochemical double layer which is formed at the interface between the electrode and electrolyte. Carbon materials have a high specific surface area resulting in a high capability for charge accumulation at the interface of electrode and electrolyte. To improve the specific capacitance of carbon materials, other than the porosity of the material and high specific surface area, functional groups must be considered. Their presence on the surface of carbon materials may induce faradaic redox reactions of oxygenated groups on the surface of the material leading to an increase in the total capacitance of the electrode [12]. Another way to increase the capacitance and enhance stability is to synthesis carbon-supported transition metal oxides composites.

Due to their low cost, high voltage window, high conductivity in a doped state and high storage capacity/porosity/reversibility, conducting polymers have been considered for electrochemical energy storage applications. [33–36]. They give capacitance through the redox cycle due to the

high content of functional groups in conducting polymers. During the redox reactions involving the whole polymer, ions are moved to the polymer backbone during oxidation and, during reduction, from the polymer backbone to the electrolyte [37]. The common conducting polymers in supercapacitor applications are polyaniline, polypyrrol, polythiophene [38–41]. However, the electrode may experience a fading electrochemical output during cycling due to swelling and shrinking of conductive polymers that may occur during the charging/discharging process. This compromise conducting polymers as electrode materials for supercapacitor applications. A few approaches have been investigated to improve the challenge of low stability. For example, improving the structures, morphologies of polymer materials [42], and fabricating composite electrode materials [43–50]. The electrochemical performance of conducting polymers can be greatly enhanced by preparing a conducting polymer-based composite using carbon, inorganic oxides/hydroxides, and metal compounds.

Metal oxides/hydroxides/sulfides (layered transition-metal dichalcogenides) as electrode materials in SCs received attention because of their high capacity potential, as well as their excellent physico-chemical properties and cycling stability. In the supercapacitor applications, the key criteria for metal oxides/hydroxides/sulfides as electrode materials are: (1) The metal oxide/hydroxides/sulfides should be electronically conductive, (2) the metal can occur in two or more oxidation states with no phase changes, and (3) the protons can freely intercalate into and out of the oxide/sulfide lattice on reduction and oxidation respectively [33,51]. In general, metal oxides/hydroxides/sulfides in SCs have high capacity than carbon materials and greater electrochemical stability than polymer materials due to electrochemical faradaic reactions within sufficient potential windows between electrode materials and ions [52–58].

The electrode materials of SCs used in this work are found in carbon materials, conductive polymers (graphene, polyaniline (PANI) and metal oxides (birnessite-type manganese dioxide (MnO2)/carbon composite), respectively. However, PANI is unstable because of the

charge/discharge process and to avoid this restriction, combination of PANI with carbon materials has proven to improve the stability of PANI as well as maximize the capacitance value [76, 77]. PANI/graphene nanocomposites have a far better capacitance efficiency than that of individual PANI and the synergy effect of PANI and graphene significantly enhances the composite material's retention life. On the other hand, the metal oxide birnessite-type manganese dioxide (MnO_2) has low electrical conductivity resulting in low cycling stability [59,60]. The low cycling stability of the MnO_2 is improved by using carbon-based materials with excellent conductivity as support during MnO_2 synthesis [61–64].

2.5 Electrolytes for supercapacitors

The electrolyte placed between the positive and negative electrode of a supercapacitor plays a very significant role in supercapacitors (Figure 2.3). It is worth mentioning that in two-electrode configuration the electrolyte is between two electrodes and its ions are transported between two electrodes through a separator, but in three-electrode configuration, the electrodes (i.e. working, reference and counter electrode) are immersed in the electrolyte. For the electrolyte to be suitable for supercapacitors it has to meet the requirements such as having wide voltage window, high electrochemical stability, high ionic conductivity, small solvated ionic radius, low resistivity, low viscosity, low volatility, low toxicity, low cost as well as availability at high purity [33]. The electrolyte used in supercapacitors can be classified into three types: aqueous, organic, and ionic liquids (ILs) electrolytes.

In this study, aqueous electrolytes (such as $NaNO_3$ and KNO_3 aqueous solution) were preferred compared to organic electrolytes, since they can provide a higher ionic conductivity and lower resistance. In addition, aqueous electrolytes can be processed and used without strict supervision of the processes and conditions of preparation, whereas organic electrolytes require

specific processes and conditions to obtain ultra-pure electrolytes. Aqueous electrolyte supercapacitors can show higher capacitance and higher power than organic electrolytes, possibly due to higher ionic conductivity and lower ionic radius [33]. Nevertheless, because of the decomposition of water at high applied voltages, the aqueous electrolytes have a limited operating voltage of 1.23 V (theoretical value) which may limit the potential window of the supercapacitor. However, due to the synergy between the electrodes and the electrolyte, SCs using aqueous electrolytes have shown the ability to achieve higher operating voltages, ~2.0 V [65–67].

Ionic liquids (ILs) also known as room temperature ionic liquids (RTILs) are organic salts which are liquids at room temperature [68]. This type of salts is called molten salts and their attractive properties make them promising candidates for SCs electrolytes. They possess interesting properties, such as thermal stability at high temperatures, environmentally friendly, non-flammability, and a wide potential window (typically about 4.5 V).

2.6 Testing an electrochemical cell

For research purposes the electrochemical efficiency of the single electrode is measured first in three electrode configurations to obtain the electrochemical properties of each electrode, also in two-electrode configuration. The device is generally referred to as a half-cell in the three-electrode configuration, and as a full-cell in the two-electrode configuration. Figure 2.6 shows the three-electrode configuration scheme diagram. The three-electrode configuration consists of a working electrode (WE), a counter electrode (CE) and a reference electrode (RE). The counter type and the reference electrode are based on the electrolyte used. The WE typically consist of active materials that are pasted onto the current collector, which function as a substrate where the electrochemical reaction takes place. Normally, the RE electrode which

has a stable and known electrode potential is used as a benchmark in determining a WE 's potential without allowing current through it while the CE is used to complete the circuit and allowing the necessary amount of current through the circuit to match the current produced at the WE. A CE may be a glassy carbon plate or platinum wire and silver / silver chloride electrode (Ag / AgCl) or saturated calomel electrode (SCE) acts as the RE in the three-electrode system depending on the electrolyte used, (e.g. in an acid electrolyte or neutral electrolyte). The current collector plays an important role in cycle stability and electrochemical performance of SCs. It supports the electrode material and accumulates electrons. Conductivity of the current collector with electrode material has influence on specific power and capacitance of SCs. Current collector have characteristics such as high electrochemical stability, high thermal stability, high electrical conductivity, lightweight, high mechanical strength, and low cost [69]. Metal foam or foil type (e.g. Ni, Cu, Al, etc.) current collector are commonly used. In this study Ni foil or foam was preferred as a current collector.

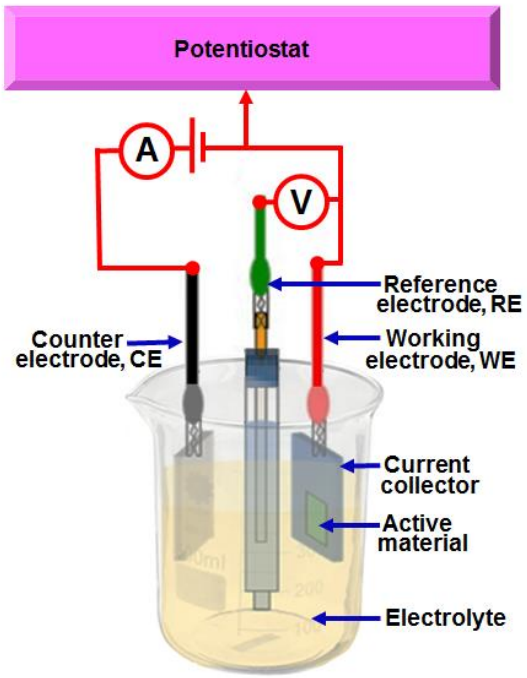

Figure 2.6. *Schematic diagram of three electrode cell setup [10].*

Figure 2.7 illustrates the setup of two-electrode cells. The current and sense (S) leads are paired together as can be seen from the figure: CE and RE are paired to one of the electrodes while WE and S are both connected to the opposite electrode. The potential across the entire cell is measured in this configuration, including inputs from the electrolyte/CE interface and from the electrolyte itself. The S leads measure the voltage by the working electrode, electrolyte, and counter electrode lowered by the current, i.e. a whole cell. This system is usually used for energy storage or conversion devices.

The two electrode cells may also be either symmetric, asymmetric, or hybrid. As illustrated in figure 2.7, the asymmetric device generally refers to any combination of positive and negative electrodes, when the two electrodes differ in mass, thickness, material type, etc. On the other hand, because the two electrodes are constructed from the same material, with the same density, thickness and other identical electrochemical properties, the symmetric structure they refer to is a mixture of positive and negative. Thus, it is important to note that when designing the supercapacitors, symmetric systems are not the best. This is because electrodes made of different materials may be used to expand the potential operating window. Different storage mechanisms are applied in a hybrid device in the positive and negative electrode materials which are the focus of asymmetric devices' special case [70]. This concept of an asymmetric interface is also exciting, because it enables us to create a mixture of positive and negative electrode materials and to achieve a smart balancing of their weight/volume, so that overall device efficiency can be significantly improved in terms of voltage window, capacitance and longevity compared to their symmetrical counterparts [70,71].

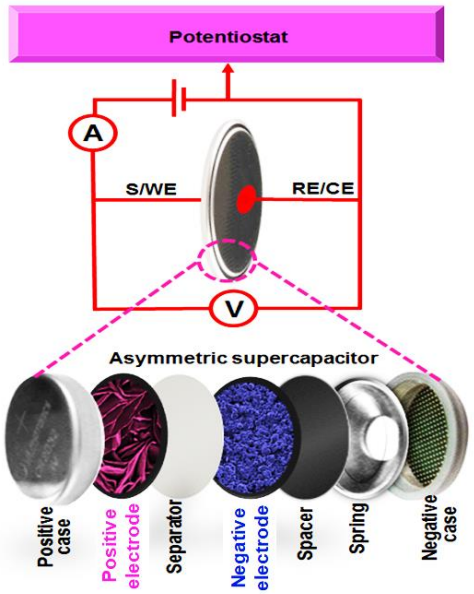

Figure 2.7. *Schematic diagram of the two-electrode cell setup including the design of the assembled structure of supercapacitor devices.*

The cell's electrochemical performance is determined by an electrode, which is the cell 's main engine. That is determined in terms of life expectancy, self-discharge, capacity, and resistance, to mention a few. The most critical stage is the fabrication of electrodes using an active material coating process. As a result, to achieve both high performance and durability a strict control of the preparation process is required. Nickel foam has been recently used as a current collector to study electrochemical performance of electrodes for applications in supercapacitors [72–76]. Due to its high conductivity, chemical stability in the electrolyte and mechanical strength, the nickel foam is preferred as the current collector since these are the requirements of a current collector in supercapacitor application.

Firstly, binders, active materials and conductive additives are combined in the process of coating electrodes (production electrodes) to achieve a homogeneous slurry with the desired density, and then the slurry is coated on annealed nickel foam, the electrode is then dried and roll pressed to achieve a uniform electrode coating layer. They are brought into a glove box with ultra-low moisture once the electrodes are prepared. A pair of these electrodes is wrapped

in the desired shape around a central mandrel, with a separator layer placed between them. So, this separator is filled in with the electrolyte. Special care is generally required for the electrolyte-filling process. The amount of electrolyte in the cell is important since excess electrolyte in action can lead to excessive gassing and leakage. The cell is subjected to cycling test after electrolyte filling and sealing of the cell is done.

2.7 Evaluation of electrode material for electrochemical capacitors

The electrochemical performance of the electrodes is evaluated by cyclic voltammetry (CV), galvanostatic chronopotentiometry (GCP) and electrochemical impedance spectroscopy (EIS).

2.7.1 Cyclic voltammetry (CV)

CV is a potentiodynamic electroanalytical technique that offers qualitative information on the thermodynamics of redox processes, the kinetics of heterogeneous electron transfer reactions, and the processes of adsorption that occur in an electrochemical cell at the electrode/electrolyte interphase. The CV measurements are performed by cycling a WE 's potential and the resulting current is measured. Therefore, a CV curve is a plot of a current response versus the applied potential, as shown in figure 2.8, which describe the nature of the processes that can occur at the electrode/electrolyte interphase. For instance, in figure 2.7, the CV plot reveals the behavior of the electrode as either electrochemical double layer capacitive (i.e. rectangular CV curve) or pseudocapacitive (i.e. CV curve with redox peaks due to faradic reactions) [77]. The reverse scan of an ideal EDLC electrode in electrochemical double-layer capacitive action is a mirror image of the forward scan, indicating that the measured current in CV is independent of the potential applied [78]. However, the accumulation of charge on the electrode (the measured current) is dependent on the potential applied in the pseudocapacitive electrode [79]. In CV,

there are three processes of electron transfer that occur on the electrode surface depending on the nature of the material being evaluated, that is, reversible, quasi-reversible or irreversible. The difference between the processes of electron transfer are as follows: (1) The reversible electron transfer occurs when electron transfer rate is very high (fast). (2) The irreversible electron transfer on the other hand occurs when electron transfer rate is very low (slow). (3) Quasi-reversible or irreversible falls between completely reversible and irreversible electron transfer.

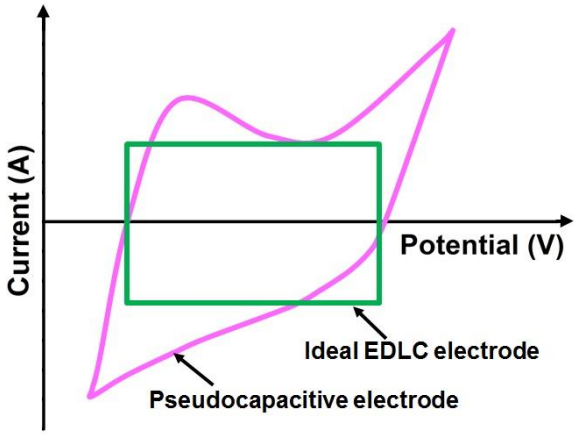

Figure 2.8. *Typical CV curves of an ideal EDLC electrode and pseudocapacitive electrode [10].*

Furthermore, using CV curves the specific capacitance (C_S) of the electrodes for three-electrode configuration can be calculated from the CV curves integrals using the following equation [4,80,81]:

$$C_S(\mathrm{F\ g^{-1}}) = \frac{\int I(V)dV}{mv\Delta V} \qquad (2)$$

where m is the total mass of the active material (g), v is the scan rate (V s^{-1}), $\Delta V = V_f - V_i$, and V_f and V_i are the integration potential limits of the CV curve (V), and I (V) is the CV current (A).

2.7.2 Galvanostatic charge-discharge (GCD)

The GCD is one of the most essential characterizing methods for evaluating the electrochemical performance of the electrodes of the supercapacitors. This test is performed by applying a regulated current pulse (*I*) between the working electrode and the counter electrode and measuring the corresponding induced voltage (*V*) as time function relative to the reference electrode, as shown in figure 2.9. The upper and lower potential limits for the working electrodes are set in GCD measurements (Figure 2.9). Similar to the CV plot, the GCD curve shows the electrode's behavior as either capacitive electrochemical double layer (i.e. linear GCD curve) or pseudocapacitive (i.e. nonlinear GCD curve due to faradic reactions) [77], as shown in Figure 2.9.

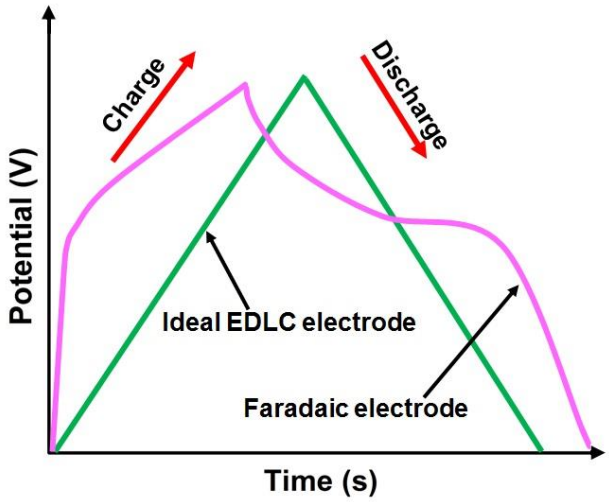

Figure 2.9. *Typical CD curves of an ideal EDLC electrode and faradaic electrode [10].*

The specific capacitance can also be calculated from GCD curves depending on the behavior the material is displaying. In GCD curves, the specific capacitance of the EDLC electrode can be calculated using the following equation [4,80–83]:

$$C_s = \frac{I \times \Delta t}{m \times \Delta V} \quad (3)$$

where Δt is the time taken for a complete discharge cycle (s), m is the total mass of the active material (g), ΔV is the potential window (V), and I is the current (A).

Moreover, if the working electrode shows EDLC behavior the specific capacitance can be calculated by integrating the area under the GCD curve using the following equation:

$$C_s = \frac{2I}{mV^2} \int V dt \quad (4)$$

where I is the applied current (A), m is the total mass of the active material (g), t is the time taken for a complete discharge cycle (s), and V is maximum cell voltage (V).

In the case of faradaic material, it is preferred to report the specific capacity (Q_S). The specific capacity of the electrodes (i.e. faradaic) can be calculated from the GCD curves, using the following equation [4,80–83]:

$$Q_S(\text{mA h g}^{-1}) = \left(\frac{I}{m}\right)\frac{t}{3.6} \quad (5)$$

where I is the applied current (A), m is the total mass of the active material (g), and t is the time taken for a complete discharge cycle (s).

Furthermore, since in two-electrode devices (i.e. both Faradic and EDLC electrode materials) there is difference in the specific capacitance of the two electrodes, a charge balance, $Q_+ = Q_-$ can be done, where Q_+ and Q_- are charges stored in both positive and negative electrodes respectively, expressed as:

$$Q = C_S m \Delta V. \quad (6)$$

The charge balance is necessary to acquire the optimal performance of the device. Based on charge balancing, the mass balance between the positive and negative electrode can be expressed using the following equation [40]:

$$\frac{m_+}{m_-} = \frac{C_{s(-)} \times V_-}{C_{s(+)} \times V_+} \quad (7)$$

where $C_{S(+)}$ and $C_{S(-)}$ are the specific capacitance of the electrodes in positive and negative potential window respectively, m_+ and m_- are the masses of the electrodes in positive and negative potential window, and V_+ and V_- are the positive and negative potential windows of the working electrodes respectively.

For faradic materials, the mass balancing is accomplished by using the following equation:

$$\frac{m_+}{m_-} = \frac{(It_d)_-}{(It_d)_+} \quad (8)$$

where $\frac{(It_d)_+}{3.6}$ and $\frac{(It_d)_-}{3.6}$ are the specific capacity of the electrode.

For the device where the positive electrode is faradic material and negative electrode is EDLC material, the mass balancing is accomplished by the following equation:

$$\frac{m_+}{m_-} = \frac{C_{s-} \Delta V_-}{Q_+ \Delta V_+} \quad (9)$$

where C_{s-} is the specific capacitance of the EDLC material, Q_+ is the specific capacity of the faradic material, ΔV_- and ΔV_+ are maximum voltages of the EDLC and faradic electrodes, respectively.

Moreover, the specific energy, E and the specific power, P can be calculated from the GCD curves, using the following equations:

$$E(W\ h\ kg^{-1}) = \left(\frac{I}{m}\right)\frac{\int V(t)dt}{3.6} \quad (10)$$

$$P(W\ kg^{-1}) = \frac{3.6\ E_d}{\Delta t} \quad (11)$$

However, for EDLC electrode material equation (8) reduce to:

$$E\ (W\ h\ kg^{-1}) = C\frac{1}{2}\Delta V^2 \quad (12)$$

The equation below is only valid for EDLC symmetric device:

$$E\ (W\ h\ kg^{-1}) = \frac{C_S \Delta V^2}{28.8} \quad (13)$$

where *I* is the applied current (A), m is the total mass of the active material (g), $\int V(t)dt$ is the integral under the discharge curve from GCD of the device, and Δ*t* is the discharge time (s).

2.7.3 Electrochemical impedance spectroscopy (EIS)

The EIS is used to further evaluate the electrochemical behavior of the electrode materials (i.e., the conductivity and transport charging properties at the electrode/electrolyte interface). EIS is a tool used for investigating the electron and ion mobility in an electrode material. It can be performed at different voltages and thus analyzing the material's response in the pure double layer range or in the redox regime at different stages. As shown in Figure 2.10, this is often represented as the Nyquist plot (imaginary component, Z'' versus the real component, Z' of the impedance). Because of the concept of electrical resistance in electrical systems EIS has attracted many researchers. The electrical resistance is basically the circuit element's ability to resist the electrical current flow. Furthermore, the EIS has also gained popularity as it can measure and provide feedback on electrical resistance in systems such as supercapacitors and LIBs. The wide range of physical and chemical phenomena in EIS is characterized by running a single experiment that covers a sufficient frequency range. The Bode plot is one of the

important EIS plots that shows a frequency dependence of the impedance phase angle. It emphasizes the correlation between the frequency and the imaginary part of the impedance, $Z''(\omega)$, and the capacitance of the material can be deduced from the linear portion of a graph of log Z'' against log f using the equation below:

$$C = \frac{1}{2\pi f|Z''|} \tag{14}$$

where C is the capacitance (F), f is the frequency, and Z'' is the imaginary impedance. The Nyquis plot consists of the low-frequency region and high-frequency region, as shown in figure 2.10.

The equivalent series (solution) resistance, R_S and the charge transfer resistance, R_{CT}, can be obtained in the high-frequency region [84]. The R_S is resistance for current flow through the solution/electrolyte by the movement of ions. The R_{CT} is formed by a single kinetically controlled electrochemical reaction. In the low frequency region, an ideal supercapacitor exhibits a vertical line parallel to the imaginary axis, but in practice supercapacitors exhibit a deviation from this ideal behavior attributed to a leakage resistance, R_L resulting from the faradaic charge transfer process [85,86]. The small R_S and R_{CT} values, i.e. ~1 Ω indicates that the electrodes have good chemical stability and low charge transfer resistance which suggest nearly an ideal capacitive performance of the electrodes/cell.

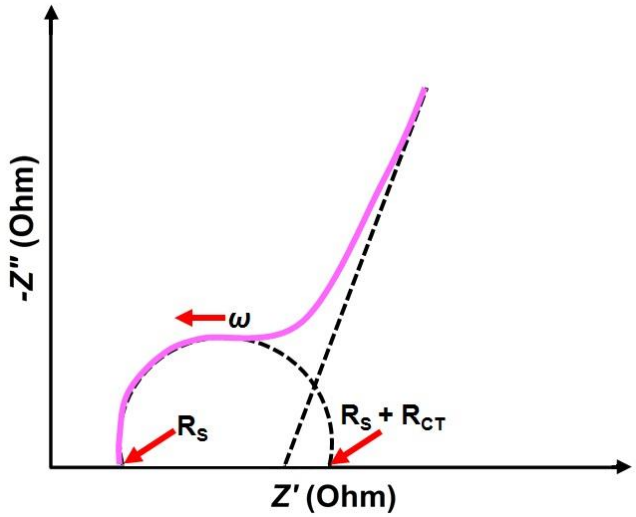

Figure 2.10. *Nyquist impendance plot [10].*

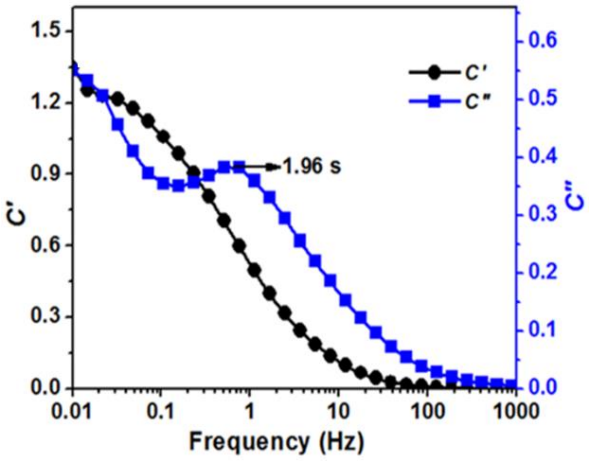

Figure 2.11. *The frequency dependence of the C'(ω) and C''(ω) capacitances (adopted from this study) [87].*

Furthermore, in the low-frequency region, the frequency dependence of the real and imaginary part of the capacitances ($C'(\omega)$ and $C''(\omega)$) can be evaluated using a complex capacitance model presented by the following equations [23,88]:

The impedance, $Z(\omega)$ given by:

$$Z(\omega) = \frac{1}{j\omega \times C(\omega)} \tag{15}$$

can be written in the complex form as

$$Z(\omega) = Z'(\omega) + jZ"(\omega) \tag{16}$$

Therefore, equation (11) and (12) gives:

$$C(\omega) = \frac{1}{\omega \times (jZ'(\omega) - Z"(\omega))}$$

$$= \frac{-(Z"(\omega) + jZ'(\omega))}{\omega |Z(\omega)|^2} \tag{17}$$

Thus, $C(\omega)$ in the complex form can be written as:

$$C(\omega) = C'(\omega) - jC"(\omega) \tag{18}$$

which gives:

$$C'(\omega) = \frac{Z"(\omega)}{\omega |Z(\omega)|^2} \tag{19}$$

$$C"(\omega) = \frac{Z'(\omega)}{\omega |Z(\omega)|^2} \tag{20}$$

where Z' and Z'' are the real part and the imaginary part of the impedance, respectively, defined as:

$$|Z(\omega)|^2 = Z'(\omega)^2 + Z"(\omega)^2 \tag{21}$$

and $\omega = 2\pi f$. The $C'(\omega)$, which is the actual accessible capacitance of the device that can be delivered, corresponds to the deliverable capacitance of 1.35 F in Figure 2.11 [87]. The $C''(\omega)$ provides a relaxation time of 1.96 s which suggests that the device can be charged within few seconds [87].

REFERENCES

[1] Y. Xie, Z. Song, S. Yao, H. Wang, W. Zhang, Y. Yao, B. Ye, C. Song, J. Chen, Y. Wang, High capacitance properties of electrodeposited PANI-Ag nanocable arrays, Materials Letters 86 (2012) 77–79.

[2] W. Sun, X. Chen, Fabrication and tests of a novel three dimensional micro supercapacitor, Microelectron. Eng. 86 (2008) 1307–1310. https://doi.org/10.1016/j.mee.2008.12.010.

[3] D.P. Dubal, S. V Patil, W.B. Kim, C.D. Lokhande, Supercapacitors based on electrochemically deposited polypyrrole nanobricks, Mater. Lett. 65 (2011) 2628–2631. https://doi.org/10.1016/j.matlet.2011.05.114.

[4] P. Simon, Y. Gogotsi, Materials for electrochemical capacitors, Nat. Mater. 7 (2008) 845–854. https://doi.org/10.1142/9789814287005_0033.

[5] B.E. Conway, Electrochemical Supercapacitors Scientific Fundamentals and Technological Applications 1999.pdf, Kluwer Academic/Plenum: New York, 1999.

[6] J.R.J. Miller, A.F.A. Burke, Electrochemical capacitors: challenges and opportunities for real-world applications, Electrochem. Soc. Interface. 17 (2008) 53.

[7] A. Burke, R&D considerations for the performance and application of electrochemical capacitors, Electrochim. Acta. 53 (2007) 1083–1091. https://doi.org/10.1016/j.electacta.2007.01.011.

[8] G. Feng, S. Li, V. Presser, P.T. Cummings, Molecular Insights into Carbon Supercapacitors Based on Room-Temperature Ionic Liquids, J. Phys. Chem. Lett. 4 (2013) 3367–3376. https://doi.org/10.1021/jz4014163.

[9] X. Rui, H. Tan, Q. Yan, Nanostructured metal sulfides for energy storage, Nanoscale. 6

(2014) 9889. https://doi.org/10.1039/C4NR03057E.

[10] Mologadi Nkiyasi Rantho, Synthesis and characterization of vanadium disulfide nanosheets and carbonized iron cations adsorbed onto polyaniline for high-perfomance supercapacitor applications,Masters dessertation, University of Pretoria, (2017.

[11] G. Zhang, M. Kong, Y. Yao, L. Long, M. Yan, X. Liao, G. Yin, Z. Huang, A.M. Asiri, X. Sun, One-pot synthesis of γ -MnS / reduced graphene oxide with enhanced performance for aqueous asymmetric supercapacitors, Nanotechnology 28 (2017) 065402. https://doi.org/10.1088/1361-6528/aa52a5.

[12] R. Kötz, M. Carlen, Principles and applications of electrochemical capacitors, Electrochim. Acta. 45 (2000) 2483–2498. https://doi.org/10.1016/S0013-4686(00)00354-6.

[13] T. Brousse, D. Bélanger, J.W. Long, To Be or Not To Be Pseudocapacitive?, J. Electrochem. Soc. 162 (2015) A5185–A5189. https://doi.org/10.1149/2.0201505jes.

[14] G. Wang, L. Zhang, J. Zhang, A review of electrode materials for electrochemical supercapacitors, Chem. Soc. Rev. 41 (2012) 797–828. https://doi.org/Doi 10.1039/C1cs15060j.

[15] E. Frackowiak, S. Delpeux, K. Jurewicz, K. Szostak, D. Cazorla-Amoros, F. Béguin, Enhanced capacitance of carbon nanotubes through chemical activation, Chem. Phys. Lett. 361 (2002) 35–41. https://doi.org/10.1016/S0009-2614(02)00684-X.

[16] V. Ruiz, C. Blanco, E. Raymundo-Piñero, V. Khomenko, F. Béguin, R. Santamaría, Effects of thermal treatment of activated carbon on the electrochemical behaviour in supercapacitors, Electrochim. Acta. 52 (2007) 4969–4973. https://doi.org/10.1016/J.ELECTACTA.2007.01.071.

[17] C. Peng, S. Zhang, D. Jewell, G.Z. Chen, Carbon nanotube and conducting polymer composites for supercapacitors, Prog. Nat. Sci. 18 (2008) 777–788. https://doi.org/10.1016/J.PNSC.2008.03.002.

[18] C. Peng, J. Jin, G.Z.Chen, A comparative study on electrochemical co-deposition and capacitance of composite films of conducting polymers and carbon nanotubes, Electrochim. Acta. 53 (2007) 525–537. https://doi.org/10.1016/J.ELECTACTA.2007.07.004.

[19] A. Malinauskas, J. Malinauskiene, A. Ramanavičius, Conducting polymer-based nanostructurized materials: electrochemical aspects, Nanotechnology. 16 (2005) R51–R62. https://doi.org/10.1088/0957-4484/16/10/R01.

[20] S. Il Cho, S.B. Lee, Fast Electrochemistry of Conductive Polymer Nanotubes: Synthesis, Mechanism, and Application, Acc. Chem. Res. 41 (2008) 699–707. https://doi.org/10.1021/ar7002094.

[21] Y.R. Ahn, M.Y. Song, S.M. Jo, C.R. Park, D.Y. Kim, Electrochemical capacitors based on electrodeposited ruthenium oxide on nanofibre substrates, Nanotechnology. 17 (2006) 2865–2869. https://doi.org/10.1088/0957-4484/17/12/007.

[22] V.D. Patake, C.D. Lokhande, O.S. Joo, Electrodeposited ruthenium oxide thin films for supercapacitor: Effect of surface treatments, Appl. Surf. Sci. 255 (2009) 4192–4196. https://doi.org/10.1016/J.APSUSC.2008.11.005.

[23] C.-C. Hu, Y.-H. Huang, K.-H. Chang, Annealing effects on the physicochemical characteristics of hydrous ruthenium and ruthenium–iridium oxides for electrochemical supercapacitors, J. Power Sources. 108 (2002) 117–127. https://doi.org/10.1016/S0378-7753(02)00011-3.

[24] J. Yan, T. Wei, J. Cheng, Z. Fan, M. Zhang, Preparation and electrochemical properties of lamellar MnO_2 for supercapacitors, Mater. Res. Bull. 45 (2010) 210–215. https://doi.org/10.1016/J.MATERRESBULL.2009.09.016.

[25] J. Jiang, A. Kucernak, Electrochemical supercapacitor material based on manganese oxide: preparation and characterization, Electrochim. Acta. 47 (2002) 2381–2386. https://doi.org/10.1016/S0013-4686(02)00031-2.

[26] P.A. Nelson, J.R. Owen, A High-Performance Supercapacitor/Battery Hybrid Incorporating Templated Mesoporous Electrodes, J. Electrochem. Soc. 150 (2003) A1313. https://doi.org/10.1149/1.1603247.

[27] M. Nakayama, A. Tanaka, Y. Sato, T. Tonosaki, K. Ogura, Electrodeposition of Manganese and Molybdenum Mixed Oxide Thin Films and Their Charge Storage Properties, Langmuir, 21, 13 (2005) 5907–5913. https://doi.org/10.1021/LA050114U.

[28] K. Krishnamoorthy, G.K. Veerasubramani, S. Radhakrishnan, S.J. Kim, Supercapacitive properties of hydrothermally synthesized sphere like MoS_2 nanostructures, Mater. Res. Bull. 50 (2014) 499–502. https://doi.org/10.1016/J.MATERRESBULL.2013.11.019.

[29] J. Feng, X. Sun, C. Wu, L. Peng, C. Lin, S. Hu, J. Yang, Y. Xie, Metallic Few-Layered VS_2 Ultrathin Nanosheets: High Two-Dimensional Conductivity for In-Plane Supercapacitors, J. Am. Chem. Soc. 133 (2011) 17832–17838. https://doi.org/10.1021/ja207176c.

[30] P. Justin, G.R. Rao, CoS spheres for high-rate electrochemical capacitive energy storage application, Int. J. Hydrogen Energy. 35 (2010) 9709–9715. https://doi.org/10.1016/J.IJHYDENE.2010.06.036.

[31] T.M. Masikhwa, F. Barzegar, J.K. Dangbegnon, A. Bello, M.J. Madito, D. Momodu, N.

Manyala, Asymmetric supercapacitor based on VS_2 nanosheets and activated carbon materials, RSC Adv. 6 (2016) 38990–39000. https://doi.org/10.1039/C5RA27155J.

[32] Y. Zhang, H. Feng, X. Wu, L. Wang, A. Zhang, T. Xia, H. Dong, X. Li, L. Zhang, Progress of electrochemical capacitor electrode materials: A review, Int. J. Hydrog. Energy, 34 (2009) 4889–4899. https://doi.org/10.1016/j.ijhydene.2009.04.005.

[33] G. Wang, L. Zhang, J. Zhang, A review of electrode materials for electrochemical supercapacitors, Chem. Soc. Rev. 41 (2012) 797–828. https://doi.org/10.1039/C1CS15060J.

[34] K.R. Prasad, K. Koga, and N. Miura, Electrochemical Deposition of Nanostructured Indium Oxide: High-Performance Electrode Material for Redox Supercapacitors, Chem. Mater. 16, 10 (2004) 1845–1847. https://doi.org/10.1021/CM0497576.

[35] M. Kalaji, P.J. Murphy, G.O. Williams, The study of conducting polymers for use as redox supercapacitors, Synth. Met. 102 (1999) 1360–1361. https://doi.org/10.1016/S0379-6779(98)01334-4.

[36] Y. Zhou, B. He, W. Zhou, J. Huang, X. Li, B. Wu, H. Li, Electrochemical capacitance of well-coated single-walled carbon nanotube with polyaniline composites, Electrochim. Acta. 49 (2004) 257–262. https://doi.org/10.1016/J.ELECTACTA.2003.08.007.

[37] P. Sharma, T.S. Bhatti, A review on electrochemical double-layer capacitors, Energy Convers. Manag. 51 (2010) 2901–2912. https://doi.org/10.1016/J.ENCONMAN.2010.06.031.

[38] K.S. Ryu, K.M. Kim, N.G. Park, Y.J. Park, S.H. Chang, Symmetric redox supercapacitor with conducting polyaniline electrodes, J. Power Sources. 103 (2002) 305–309. https://doi.org/10.1016/S0378-7753(01)00862-X.

[39] A. Clemente, S. Panero, E. Spila, B. Scrosati, Solid-state, polymer-based, redox capacitors, Solid State Ionics. 85 (1996) 273–277. https://doi.org/10.1016/0167-2738(96)00070-7.

[40] A. Laforgue, P. Simon, C. Sarrazin, J.-F. Fauvarque, Polythiophene-based supercapacitors, J. Power Sources. 80 (1999) 142–148. https://doi.org/10.1016/S0378-7753(98)00258-4.

[41] C. Arbizzani, M. Mastragostino, F. Soavi, New trends in electrochemical supercapacitors, J. Power Sources. 100 (2001) 164–170. https://doi.org/10.1016/S0378-7753(01)00892-8.

[42] Y.-G. Wang, H.-Q. Li, Y.-Y. Xia, Ordered Whiskerlike Polyaniline Grown on the Surface of Mesoporous Carbon and Its Electrochemical Capacitance Performance, Adv. Mater. 18 (2006) 2619–2623. https://doi.org/10.1002/adma.200600445.

[43] H. Mi, X. Zhang, S. An, X. Ye, S. Yang, Microwave-assisted synthesis and electrochemical capacitance of polyaniline/multi-wall carbon nanotubes composite, Electrochem. Commun. 9 (2007) 2859–2862. https://doi.org/10.1016/j.elecom.2007.10.013.

[44] M. Wu, G.A. Snook, V. Gupta, M. Shaffer, D.J. Fray, G.Z. Chen, Electrochemical fabrication and capacitance of composite films of carbon nanotubes and polyaniline, J. Mater. Chem. 15 (2005) 2297–2303. https://doi.org/10.1039/b418835g.

[45] M.J. Bleda-Martínez, C. Peng, S. Zhang, G.Z. Chen, E. Morallón, D. Cazorla-Amorós, Electrochemical Methods to Enhance the Capacitance in Activated Carbon/Polyaniline Composites, J. Electrochem. Soc. 155 (2008) A672. https://doi.org/10.1149/1.2956969.

[46] D. Salinas-Torres, J.M. Sieben, D. Lozano-Castelló, D. Cazorla-Amorós, E. Morallón,

Asymmetric hybrid capacitors based on activated carbon and activated carbon fibre-PANI electrodes, Electrochim. Acta. 89 (2013) 326–333. https://doi.org/10.1016/j.electacta.2012.11.039.

[47] K.S. Ryu, Y.-G. Lee, K.M. Kim, Y.J. Park, Y.-S. Hong, X. Wu, M.G. Kang, N.-G. Park, R.Y. Song, J.M. Ko, Electrochemical capacitor with chemically polymerized conducting polymer based on activated carbon as hybrid electrodes, Synth. Met. 153 (2005) 89–92. https://doi.org/10.1016/j.synthmet.2005.07.167.

[48] F. Chen, P. Liu, Q. Zhao, Well-defined graphene/polyaniline flake composites for high performance supercapacitors, Electrochim. Acta. 76 (2012) 62–68. https://doi.org/10.1016/j.electacta.2012.04.154.

[49] G.A. Snook, P. Kao, A.S. Best, Conducting-polymer-based supercapacitor devices and electrodes, J. Power Sources. 196 (2010) 1–12. https://doi.org/10.1016/j.jpowsour.2010.06.084.

[50] S. Bose, T. Kuila, A.K. Mishra, R. Rajasekar, N.H. Kim, J.H. Lee, Carbon-based nanostructured materials and their composites as supercapacitor electrodes, J. Mater. Chem. Mater. Chem. 22 (2012) 767–784. https://doi.org/10.1039/c1jm14468e.

[51] B.E. Conway, Electrochemical supercapacitors: scientific fundamentals and technological applications, Springer Science & Business Media Conway, 2013.

[52] A.A. Khaleed, A. Bello, J.K. Dangbegnon, M.J. Madito, O. Olaniyan, F. Barzegar, K. Makgopa, K.O. Oyedotun, B.W. Mwakikunga, S.C. Ray, N. Manyala, Solvothermal synthesis of surfactant free spherical nickel hydroxide/graphene oxide composite for supercapacitor application, J. Alloys Compd. 721 (2017) 80–91. https://doi.org/10.1016/J.JALLCOM.2017.05.310.

[53] D.-D. Zhao, S.-J. Bao, W.-J. Zhou, H.-L. Li, Preparation of hexagonal nanoporous nickel hydroxide film and its application for electrochemical capacitor, Electrochem. Commun. 9 (2007) 869–874. https://doi.org/10.1016/j.elecom.2006.11.030.

[54] Y. Tang, T. Chen, S. Yu, Y. Qiao, S. Mu, J. Hu, F. Gao, Synthesis of graphene oxide anchored porous manganese sulfide nanocrystals via the nanoscale Kirkendall effect for supercapacitors, J. Mater. Chem. A. 3 (2015) 12913–12919. https://doi.org/10.1039/C5TA02480C.

[55] P.-C. Chen, G. Shen, Y. Shi, H. Chen, C. Zhou, Preparation and Characterization of Flexible Asymmetric Supercapacitors Based on Transition-Metal-Oxide Nanowire/Single-Walled Carbon Nanotube Hybrid Thin-Film Electrodes, ACS Nano. 4 (2010) 4403–4411. https://doi.org/10.1021/nn100856y.

[56] Y. Tang, T. Chen, S. Yu, Y. Qiao, S. Mu, S. Zhang, Y. Zhao, L. Hou, W. Huang, F. Gao, A highly electronic conductive cobalt nickel sulphide dendrite/quasi-spherical nanocomposite for a supercapacitor electrode with ultrahigh areal specific capacitance, J. Power Sources. 295 (2015) 314–322. https://doi.org/10.1016/j.jpowsour.2015.07.035.

[57] Y. Tang, T. Chen, S. Yu, Morphology controlled synthesis of monodispersed manganese sulfide nanocrystals and their primary application in supercapacitors with high performances, Chem. Commun. 51 (2015) 9018–9021. https://doi.org/10.1039/C5CC01700A.

[58] L. Dong, C. Xu, Y. Li, Z.H. Huang, F. Kang, Q.H. Yang, Y. Liu, R. Wang, X. Yan, T. Chen, Y. Tang, Y. Qiao, Z. Liu, W. Guo, J. Song, S. Mu, S. Yu, Y. Zhao, F. Gao, A. Gencer Imer, All-solid-state high performance asymmetric supercapacitors based on novel MnS nanocrystal and activated carbon materials, Sci. Rep. 6 (2016) 23289. https://doi.org/10.1038/srep23289.

[59] Y. Jin, H. Chen, M. Chen, N. Liu, Q. Li, Graphene-Patched CNT/MnO_2 Nanocomposite Papers for the Electrode of High-Performance Flexible Asymmetric Supercapacitors, ACS Appl. Mater. Interfaces. 5 (2013) 3408–3416. https://doi.org/10.1021/am400457x.

[60] L. Li, Z.A. Hu, N. An, Y.Y. Yang, Z.M. Li, H.Y. Wu, Facile Synthesis of MnO_2 /CNTs Composite for Supercapacitor Electrodes with Long Cycle Stability, J. Phys. Chem. C. 118 (2014) 22865–22872. https://doi.org/10.1021/jp505744p.

[61] D. Gueon, J.H. Moon, MnO_2 Nanoflake-Shelled Carbon Nanotube Particles for High-Performance Supercapacitors, ACS Sustain. Chem. Eng. 5 (2017) 2445–2453. https://doi.org/10.1021/acssuschemeng.6b02803.

[62] B. Brown, I.A. Cordova, C.B. Parker, B.R. Stoner, J.T. Glass, Optimization of Active Manganese Oxide Electrodeposits Using Graphenated Carbon Nanotube Electrodes for Supercapacitors, Chem. Mater. 27 (2015) 2430–2438. https://doi.org/10.1021/cm504519m.

[63] J. Jiang, Y. Li, J. Liu, X. Huang, C. Yuan, X.W.D. Lou, Recent Advances in Metal Oxide-based Electrode Architecture Design for Electrochemical Energy Storage, Adv. Mater. 24 (2012) 5166–5180. https://doi.org/10.1002/adma.201202146.

[64] G. Lota, K. Fic, E. Frackowiak, Carbon nanotubes and their composites in electrochemical applications, Energy Environ. Sci. 4 (2011) 1592–1605. https://doi.org/10.1039/c0ee00470g.

[65] F.O. Ochai-Ejeh, A. Bello, J. Dangbegnon, A.A. Khaleed, M.J. Madito, F. Bazegar, N. Manyala, High electrochemical performance of hierarchical porous activated carbon derived from lightweight cork (Quercus suber), J. Mater. Sci. 52 (2017) 10600–10613. https://doi.org/10.1007/s10853-017-1205-4.

[66] A.A. Mirghni, M.J. Madito, T.M. Masikhwa, K.O. Oyedotun, A. Bello, N. Manyala, Hydrothermal synthesis of manganese phosphate/graphene foam composite for electrochemical supercapacitor applications, J. Colloid Interface Sci. J. of Colloid and Interface Science 494 (2017) 325–337. https://doi.org/10.1016/j.jcis.2017.01.098.

[67] F. Barzegar, A. Bello, D. Momodu, M.J. Madito, J. Dangbegnon, N. Manyala, Preparation and characterization of porous carbon from expanded graphite for high energy density supercapacitor in aqueous electrolyte, J. Power Sources. 309 (2016) 245–253. https://doi.org/10.1016/j.jpowsour.2016.01.097.

[68] J.S. Wilkes, A short history of ionic liquids - From molten salts to neoteric solvents, Green Chem. 4 (2002) 73–80. https://doi.org/10.1039/b110838g.

[69] K.D. Verma, P. Sinha, S. Banerjee, K.K. Kar, Characteristics of Current Collector Materials for Supercapacitors, Springer Series in Materials Science, 300 (2020) 327-340.

[70] M.R. Lukatskaya, B. Dunn, Y. Gogotsi, Multidimensional materials and device architectures for future hybrid energy storage, Nat. Commun. 7 (2016) 12647. https://doi.org/10.1038/ncomms12647.

[71] K. Naoi, W. Naoi, S. Aoyagi, J. Miyamoto, T. Kamino, New Generation "Nanohybrid Supercapacitor," Acc. Chem. Res. 46 (2013) 1075–1083. https://doi.org/10.1021/ar200308h.

[72] K. Chen, D. Xue, Electrochemically Stabilized Porous Nickel Foam as Current Collector and Counter Electrode in Alkaline Electrolyte for Supercapacitor, J. Nanoeng. Nanomanufacturing. 4 (2014) 50–55. https://doi.org/10.1166/jnan.2014.1168.

[73] Y.F. Yuana, X.H. Xia, J.B. Wu, J.L. Yang, Y.B. Chen, S.Y. Guo, Nickel foam-supported

porous $Ni(OH)_2$/NiOOH composite film as advanced pseudocapacitor material, Electrochim. Acta. 56 (2011) 2627–2632. https://doi.org/10.1016/J.ELECTACTA.2010.12.001.

[74] Y. Zhao, K. Chen, C. Sun, K. Li, C. Meng, D. Xue, Pseudocapacitance Performances of Naked Porous Nickel Foams, Mater. Focus. 2 (2013) 239–243. https://doi.org/10.1166/mat.2013.1081.

[75] L. Jiang, R. Zou, W. Li, J. Sun, X. Hu, Y. Xue, G. He, J. Hu, $Ni(OH)_2$ /CoO/reduced graphene oxide composites with excellent electrochemical properties, J. Mater. Chem. A. 1 (2013) 478–481. https://doi.org/10.1039/C2TA00265E.

[76] Y. Zhang, C. Sun, P. Lu, K. Li, S. Song, D. Xue, Crystallization design of MnO2 towards better supercapacitance, CrystEngComm. 14 (2012) 5892–5897. https://doi.org/10.1039/c2ce25610j.

[77] D. Weingarth, M. Zeiger, N. Jäckel, M. Aslan, G. Feng, V. Presser, Graphitization as a Universal Tool to Tailor the Potential-Dependent Capacitance of Carbon Supercapacitors, Adv. Energy Mater. 4 (2014) 1400316. https://doi.org/10.1002/aenm.201400316.

[78] R. Signorelli, D.C. Ku, J.G. Kassakian, J.E. Schindall, Electrochemical Double-Layer Capacitors Using Carbon Nanotube Electrode Structures, Proc. IEEE. 97 (2009) 1837–1847. https://doi.org/10.1109/JPROC.2009.2030240.

[79] B.E. Conway, W.G. Pell, Double-layer and pseudocapacitance types of electrochemical capacitors and their applications to the development of hybrid devices, J. Solid State Electrochem. 7 (2003) 637–644. https://doi.org/10.1007/s10008-003-0395-7.

[80] B. Akinwolemiwa, C. Peng, G.Z. Chen, Redox electrolytes in supercapacitors, J.

Electrochem. Soc. 162 (2015) A5054–A5059. https://doi.org/10.1149/2.0111505jes.

[81] A. Laheäär, P. Przygocki, Q. Abbas, F. Béguin, Appropriate methods for evaluating the efficiency and capacitive behavior of different types of supercapacitors, Electrochem. Commun. 60 (2015) 21–25. https://doi.org/10.1016/j.elecom.2015.07.022.

[82] K.O. Oyedotun, M.J. Madito, A. Bello, D.Y. Momodu, A.A. Mirghni, N. Manyala, Investigation of graphene oxide nanogel and carbon nanorods as electrode for electrochemical supercapacitor, Electrochim. Acta. 245 (2017) 268-278. https://doi.org/10.1016/j.electacta.2017.05.150.

[83] G. Godillot, L. Guerlou-Demourgues, P.-L. Taberna, P. Simon, C. Delmas, Original Conductive Nano-Co3O4 Investigated as Electrode Material for Hybrid Supercapacitors, Electrochem. Solid-State Lett. 14 (2011) A139. https://doi.org/10.1149/1.3609259.

[84] Y. Zhou, H. Xu, N. Lachman, M. Ghaffari, S. Wu, Y. Liu, A. Ugur, K.K. Gleason, B.L. Wardle, Q.M. Zhang, Advanced asymmetric supercapacitor based on conducting polymer and aligned carbon nanotubes with controlled nanomorphology, Nano Energy. 9 (2014) 176–185.

[85] W. Sun, X. Chen, Preparation and characterization of polypyrrole films for three-dimensional micro supercapacitor, 193 (2009) 924–929. https://doi.org/10.1016/j.jpowsour.2009.04.063.

[86] H. Li, J. Wang, Q. Chu, Z. Wang, F. Zhang, S. Wang, Theoretical and experimental specific capacitance of polyaniline in sulfuric acid, J. Power Sources, 190 (2009) 578–586. https://doi.org/10.1016/j.jpowsour.2009.01.052.

[87] M.N. Rantho, M.J. Madito, N. Manyala, High-performance symmetric supercapacitor

device based on carbonized iron-polyaniline / nickel graphene foam, J. Alloys Compd. 819 (2019) 152993. https://doi.org/10.1016/j.jallcom.2019.152993.

[88] P.L. Taberna, P. Simon, J.-F.F. Fauvarque, Electrochemical Characteristics and Impedance Spectroscopy Studies of Carbon-Carbon Supercapacitors, J. Electrochem. Soc. 150 (2003) A292-300. https://doi.org/10.1149/1.1543948.

SECTION 3

EXPERIMENTAL DETAILS

Chapter 3

Experimental techniques

3.1 Introduction

This chapter describes the experimental procedures and various techniques used for the synthesis and characterizations of the as-synthesized materials. It also provides an introductory overview of the devices used for materials synthesis and characterization.

3.2 Synthesis of the as-prepared electrodes

3.2.1 Hydrothermal synthesis technique

In the 1990's, the hydrothermal technique attracted great attention from scientists and technologists in different fields of study. In general, the hydrothermal synthesis technique involves the growth or synthesis of crystals from any heterogeneous reaction in the presence of aqueous solvents in a closed system. This takes place under high pressure and temperature conditions to recrystallize and dissolve materials that are relatively insoluble under normal conditions. Hydrothermal synthesis technique is affordable, simple, and effective process for the synthesis of bulk powders, single crystals, and nanocomposite materials with physical and chemical properties suitable for energy storage applications [1,2]. Under hydrothermal conditions water is used as the reaction medium in an autoclave system. An autoclave is a closed stainless-steel cylinder that can resist high-temperature conditions for an extended duration of time. Additionally, the use of water as a reaction medium has advantages such as non-toxicity, non-flammability, and thermodynamic stability. It also assists in the tuning of the temperature and pressure conditions for material formation. Figure 3.1 shows the schematic

diagram of stainless steel with the Teflon liner. In this study, the hydrothermal technique was used for the production of MnO_2/carbon composite.

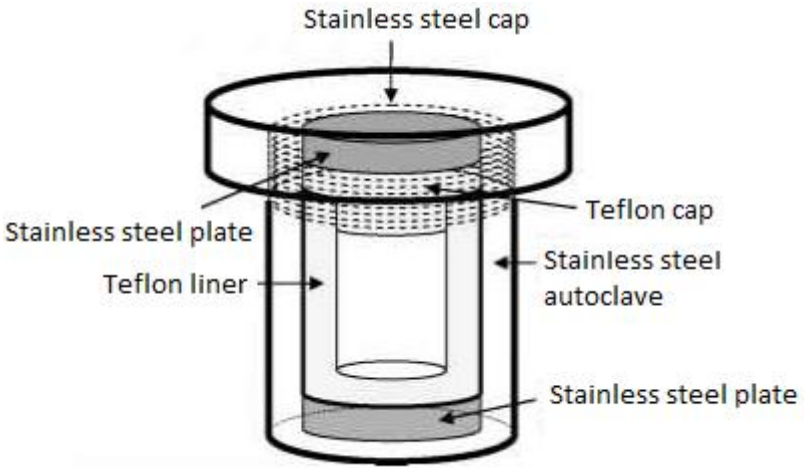

Figure 3.1. *Schematic diagram of Teflon-lined autoclave.*

3.2.2 Chemical vapour deposition (CVD) technique

CVD (Figure 3.2) is a widely used technology for processing materials. This device is suitable for the production of carbon fibers and carbon nanofibers. Briefly, CVD technique consist of the gas flow into a reaction chamber which contains one or two substrates where the gas will be deposited upon. Chemical reactions take place on or near the hot surfaces, leading to the material deposition on the substrate, followed by the production of chemical by-products that are flown out of the chamber together with the unreacted precursor gases [3]. For the purpose of this work, the CVD technique was used for the synthesis of graphene and production of carbonized iron-polyaniline/nickel graphene foam (C-Fe/PANI/Ni-GF).

Figure 3.2. *Image of the CVD system.*

3.2.3 Synthesis of MnO_2/carbon composite

MnO_2-C with hierarchical nanostructures was synthesized using $KMnO_4$ solution and spent printing carbon grains (Figure 3.3). In the synthesis, 0.6 g of spent printing carbon grains were dissolved in 32 ml of 2 M $KMnO_4$ solution [4]. The mixture was then transferred into a sealed 50 ml Teflon-lined autoclave and kept at 160 °C for 18 h. The recovered product MnO_2-C composite with nanowires/microsponges morphology was collected as a brown precipitant by several centrifugation and ethanol washing cycles. Briefly, the hydrothermal solid-liquid reaction is proposed as:

$$4MnO_4^- + 3C \rightarrow 4MnO_2 + 2CO_3^{2-} + CO_2 \qquad (1)$$

J. Fei *et al.* [4] referred to this hydrothermal method as a one-pot environmentally friendly process that changes toxic carbon grains from a spent inkjet cartridge into transition metal oxide hierarchical nanostructures through a limited hydrothermal redox reaction. Therefore,

this does not only avoid the disposal of toxic carbon grains but also provides metal oxide nanostructures for energy storage applications.

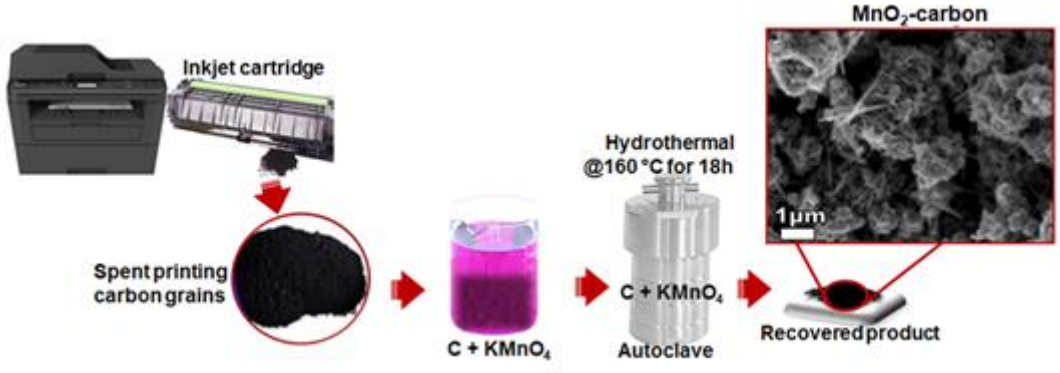

Figure 3.3. *Schematic illustration of the synthesis route for MnO_2/carbon composite.*

3.2.4 Synthesis of nickel graphene foam (Ni-GF)

The nickel foam-graphene current collector was synthesized using CVD technique. The nickel foam was first annealed at 800 °C in the presence of Ar and H_2 gas for 60 minutes, before introducing CH_4 gas at 1000 °C. Briefly, 3D scaffold template with an areal density of 420 g m^2 and thickness of 16 mm (purchased from Alantum (Munich, Germany)) was placed in a quartz tube for the CVD growth of graphene. The flow rates of the gases Ar:H_2:CH_4 were 300:9:15 SCCM respectively. After 60 minutes of deposition, the sample was cooled by manually pushing the quartz tube to a lower temperature region.

3.2.5 Synthesis of carbonized iron-polyaniline/nickel graphene foam (C-Fe/PANI/Ni-GF)

The polyaniline (PANI) used for the synthesis of for C-Fe/PANI was prepared as follows: 0.2 M aniline hydrochloride was added to a 50 ml solution of 1.0 M HCl, and in a separate beaker 0.25 M solution of ammonium persulphate was added to 1.0 M HCl. The prepared solutions were kept at room temperature for 1 h, thereafter, they were mixed and stirred for about an hour and left to polymerize. After polymerization, precipitated PANI was collected on a filter paper (after been washed several times with 100 ml of 0.2 M HCl and acetone) and dried at 60 °C overnight. Furthermore, PANI was used as a substrate for adsorbing carbonized Fe cations. Briefly, a 0.4 g of PANI and 0.2 g of iron nitrate nonahydrate ($Fe(NO_3)_3 \cdot 9H_2O$) were dissolved in a 50 mL of ethanol and dispersed until the Fe-PANI slurry was formed. The slurry was pasted on graphene supported by nickel foam and carbonized using CVD at 850 °C (ramp rate of 10 °C min^{-1}) for 2 h under nitrogen. After carbonization, the difference in the micrograph of the Ni-GF and that of Fe-PANI mixture on Ni-GF (C-Fe/PANI/Ni-GF) confirms a successful synthesis of the electrode which is expected to have strong metal-polymer/graphene interactions (see Figure 3.4). The as-prepared electrode material was used for both negative and positive electrodes in symmetric and asymmetric supercapacitor devices.

Figure 3.4. *Schematic illustration of the synthesis route for C-Fe/PANI/Ni-GF.*

3.3 Structural, and morphological characterization

3.3.1 X-ray diffraction

X-ray powder diffraction (XRD) is a non-destructive technique used to determine the atomic and molecular structure of material [10]. It can also be used to study grain size, lattice constants, and degree of crystallinity in a mixture of amorphous and crystalline materials [5],[10]. In the XRD process, X-rays generated by a cathode ray tube (X-ray tube) are filtered (to produce monochromatic radiation), collimated and directed towards the sample (Figure 3.5(a)) [10]. The interaction of the incident X-rays with the sample produces diffracted rays (constructive interference) when conditions satisfy Bragg's Law [10]. Briefly, considering the incident and diffracted X-rays from the atomic layers, as shown in Figure 3.5(b), where the angle of incidence is given by θ, and the angle 2θ gives the experimentally measured diffraction angle [10]. The total path difference, x, between the X-rays marked 1 and 2 when they arrive at the detector, point A and B respectively, is given by [5],[10]:

$$x = 2d \sin \theta. \tag{3.1}$$

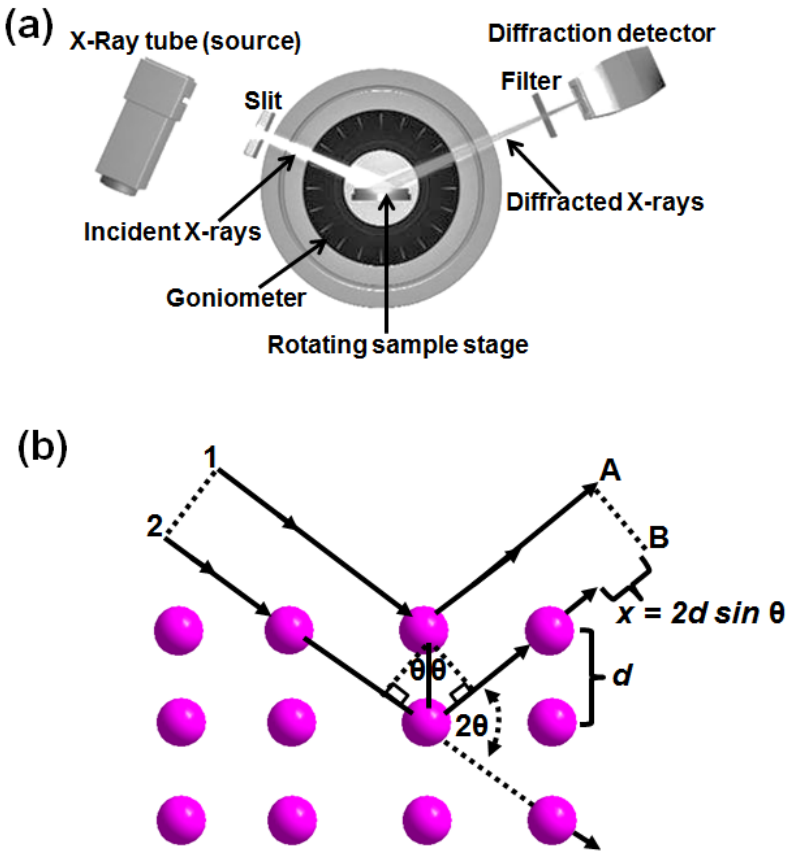

Figure 3.5. *(a) Basic components of X-ray diffractometers showing the X-Ray source/tube and detector relative to the sample. (b) Schematic illustration of the diffraction of incident X-rays by atomic planes (adopted from ref. [10]).*

For constructive interference the path difference is equal to a whole number of wavelengths, $n\lambda$, where n is a whole number. As a result, equation 3.1 becomes (Bragg's Law)

$$n\lambda = 2d \sin\theta, \quad n = 1, 2, 3,... \tag{3.2}$$

where n is a positive integer, λ is the wavelength of incident X-rays, d is the interplanar spacing and θ is the scattering angle [10].

3.3.2 Raman spectroscopy

Raman spectroscopy is a non-destructive technique that has high molecular specificity, which makes it an excellent technique for the analysis of materials[10]. It provides information on chemical structure/phase, crystallinity, and molecular interactions (i.e. structural information) [10]. In Raman spectroscopy, there is a scattering of incident photons (from the primary laser light source) by phonons (vibrational modes) during the interaction of photons with chemical bonds within a material, as shown in the figure 3.6 [10]. The interaction of incident photons of energy $\hbar\omega_L$ with the chemical bonds within a sample creates a time-dependent perturbation which increases the ground state energy (E_{GS}) to a total energy of $E_{GS} + \hbar\omega_L$ making a system (molecule) to be unstable [6,7],[10]. Since the system has no stationary state (i.e. is in the unstable situation), the photon is emitted by the perturbed system and the system goes back to the stationary state (ground state), and if the frequency of the emitted photon (ω_{Sc}) is the same as the incident one, ω_L (i.e. elastic scattering), this is referred to as Rayleigh scattering (Figure 3.6) [6,8],[10]. On the other hand, when the molecule returns to the ground state, the photon can lose part of its energy in the reaction process and disperse from the sample with a lower energy $\hbar\omega_{Sc} = \hbar\omega_L - \hbar\Omega$, where $\hbar\Omega$ is the phonon energy[10]. This process is referred to as the Stokes process (inelastic dispersion) [6,8],[10]. Additionally, if the molecule is in the excited vibrational state, and after the photon interaction the molecule returns to its ground state, the photon leaves the sample with an increased energy $\hbar\omega_{Sc} = \hbar\omega_L + \hbar\Omega$ [10]. This process is referred to as Anti-Stokes process [6,8],[10]. Therefore, between Stokes and Anti-Stokes processes, Stokes process is the most probable, hence Raman spectra are Stokes measurements plots of the intensity of the scattered photon as a function of the difference between incident and scattered photon energy [6],[10].

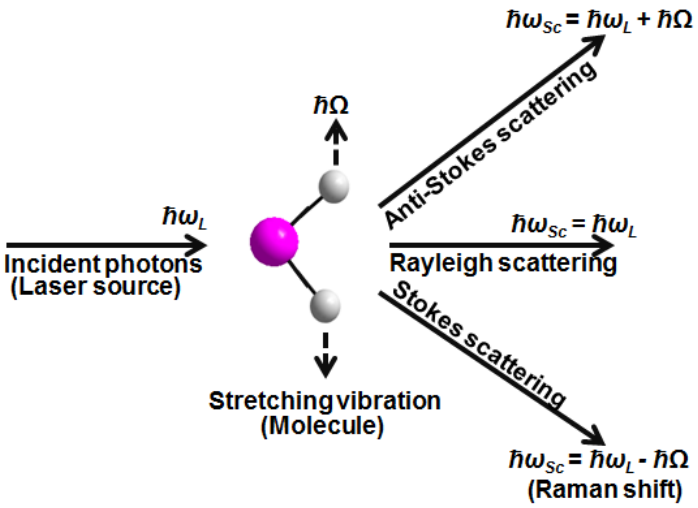

Figure 3.6. *Schematic illustration of light scattering by Rayleigh, Stokes and Anti-Stokes scattering processes in a vibrating molecule due to the time-dependent perturbation introduced by incident photons (adopted from ref. [10]).*

To illustrate briefly how the Rayleigh scattering is removed from the Raman measurements, figure 3.7 provides an overview of the main instrumental components of the standard Raman system[10]. In practice, however, various spectroscopic variations of Raman are available depending on the manufacture of the instrument[10]. For example, the beam path may be slightly different and may have additional optical components for different manufactures. It can be seen from the figure that Rayleigh scattering are optically filtered and filters are specific to the laser wavelength [9,10]. Filters are used in conjunction with diffraction grating which is used to disperse the Raman scattered light[10].

In addition , in order to detect the low intensity of the Raman scattering, the detector must be highly sensitive and hence the charge coupled devices (CCDs) are widely used in the Raman detector because they exhibit high quantum efficiencies and low signal-to-noise ratios [10]. In CCDs, the charge obtained from scattered photons is directly proportional to the intensity of

the Raman scattering[10]. There is a range of laser source options available within Raman systems or some of the Raman systems and the choice of each laser source is determined primarily by the desired wavelength and the desired spot size. Based on the choice of laser source and material, the Raman spectrum may consist of a fluorescence contribution (shown by black line in Figure 3.7(b)) that can be prevented by exciting a wavelength sample that falls outside the fluorescence region, e.g. UV (purple) and lower-energy IR (red) wavelength [10].

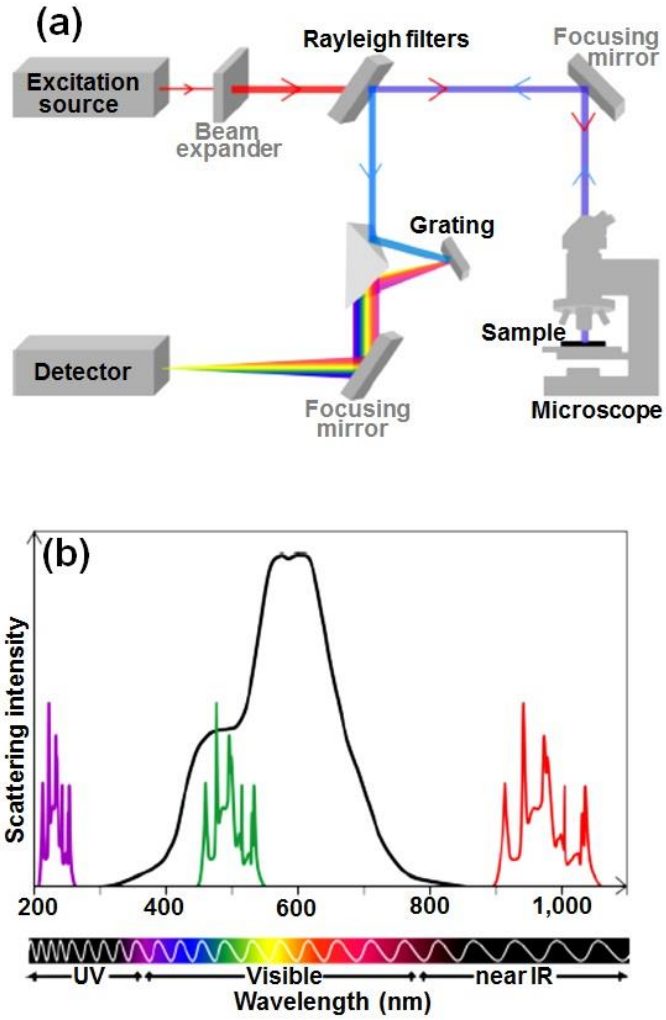

Figure 3.7. *(a) Schematic illustration of fundamental instrumental components of a typical Raman system, (b) an overview of the effect of laser excitation wavelength on the fluorescence background (adopted from ref. [10]).*

3.3.3 Scanning electron microscopy and energy dispersive X-ray spectroscopy

Scanning electron microscopy (SEM) is a non-destructive technique that is primarily used for imaging the surfaces of almost all materials at the micro-nanometer scale[10]. The technique uses an electron beam focused under ultra-high vacuum conditions to achieve high levels of magnification and resolution for imaging. The resolution of the image given by the SEM depends not only on the parameters of the electron beam, but also on the interaction of the electron beam with the sample[10]. There are two types of electrons that are primarily detected in SEM: back scattered electrons (BSE) and secondary electrons (SE). BSE is when electrons are reflected back after elastic interactions between the beam and the sample [11]. However, SE electrons originate from the atoms of the sample [11]. These are the results of inelastic interactions between the electron beam and the sample. The SEM can provide information on the morphology, topography, crystallography, and composition of materials using other analyzers in the SEM method [10,12]. When a focused beam of high-energy primary electrons impinges on the surface of the sample, among others (Figure 3.8), it produces low-energy secondary electrons with an energy usually less than 50 eV [10,13]. The image of the sample surface (morphology/topography) is constructed by measuring the intensity of these secondary electrons as a function of the position of the primary electron beam [10,12]. Field Emission SEM produces a depth of field, unique image contrast and high-resolution images[10].

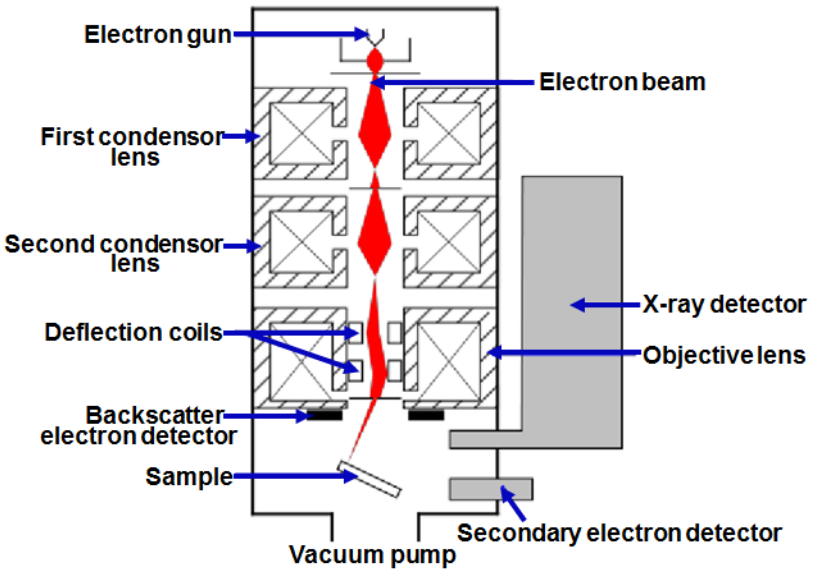

Figure 3.8. *A schematic diagram of a typical scanning electron microscopy (adopted from ref. [11]).*

Furthermore, X-rays which are ejected when an incident electron beam strikes a sample can be characterized by an energy dispersive X-ray spectroscopy (EDS), if the X-ray spectrometer (detector) is attached to the SEM system (Figure 3.8). Since each element has a unique energy difference between outer and inner electron shells, the X-rays that are detected yield elemental identification hence EDS analysis gives elemental composition of the sample.

3.3.4 Transmission electron microscopy

Transmission electron microscopy (TEM) is a non-destructive technique for the characterization of high spatial resolution[10]. It uses a beam of concentrated high-energy electrons (under ultra-high vacuum conditions) which is transmitted through a thin sample (Figure 3.9) and interacts with the sample as it passes through. Transmitted electrons are used to produce a sample image. In TEM, various types of images can be obtained from

different interactions between the electron beam and the sample[10]. For instance, an image of electron diffraction patterns is obtained from elastically scattered electrons (diffracted beam), bright field image from unscattered electrons (transmitted beam) and dark field image from elastically scattered electrons (diffracted beam) [12,14]. TEM can be used to characterize samples to obtain information about particle size, shape, crystallinity, and morphology.

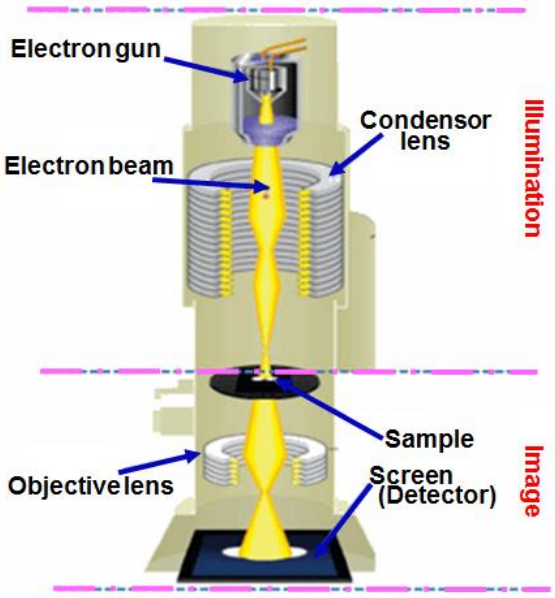

Figure 3.9. *Schematic diagram of a TEM (adopted from ref. [15]).*

3.3.5 X-ray photoelectron spectroscopy

X-ray photoelectron spectroscopy (XPS) is a surface-sensitive quantitative technique that tests the elemental composition, the chemical state, and the electronic state of the elements in the sample. The high surface specificity of XPS is achieved by using smaller angles of incidence or exit of the photoelectrons[10]. In addition, the mean free path of the detected photoelectrons is in the order of a few nm corresponding to the topmost surface atomic layers

of the sample [16]. XPS involves irradiation of the sample with a beam of X-rays (Al-Kα or Mg-Kα) while measuring the number and the kinetic energy of elastically scattered photoelectrons of the analysed sample [16]. The kinetic energy of the ejected electrons (photoelectrons) depends upon the photon energy ($h\nu$) and the binding energy of the electron in the core-shell of an atom and is usually analysed with a hemispherical energy analyser (see Figure 3.10(a)). Generally, XPS analysis is coupled with ion sputtering with noble gas ions (e.g. Ar^+) for surface cleaning and depth profiling and analysis are carried out under ultra-high vacuum conditions.

In XPS spectrum, peaks appear from atoms emitting electrons of a characteristic energy. The energies and intensities of these electrons (photoelectron peaks) enable identification and quantification of the surface chemistry of a material, as shown in figure 3.10(b). Figure 3.10(b) shows the Fe 2p XPS core level spectrum of the C-Fe/PANI/Ni-GF shows fitted Fe $2p_{3/2}$ binding energy peaks of Fe^0 (metallic Fe)/Fe^{2+} and Fe^{3+} ions.

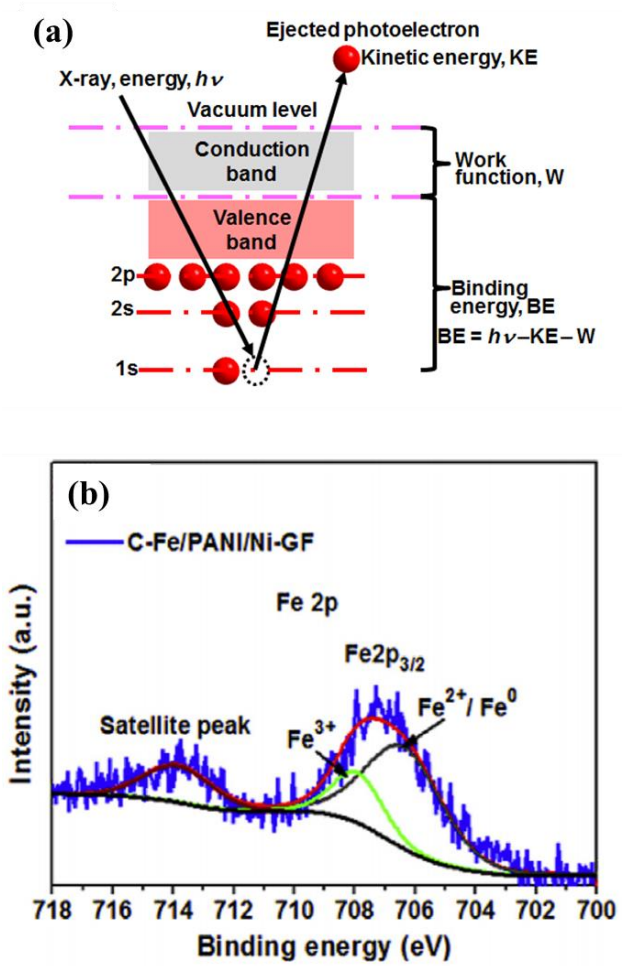

Figure 3.10. *(a) Schematic view of the photoemission process in XPS: Incident photon energy, hv is absorbed by a core level electron, if hv > BE then the electron is ejected from the atom with kinetic energy, KE. This is then detected by an analyser and the binding energy, BE of the ejected electron is determined by, BE = hv – KE – W, where W is the work function of the electron analyser, not the analysed material. (b) The XPS core level spectrum of iron, Fe 2p of the C-Fe/PANI/Ni-GF electrode material (adopted from this study).*

The characterization techniques used in this work are listed in table 3.1, including the systems settings.

Table 3.1. *Characterization techniques (apparatus and systems settings).*

Apparatus	Systems settings
XRD: XPERTPRO diffractometer (PANalytical BV, Netherlands)	• X-ray source: cobalt (Co) $K\alpha$ (λ = 0.17890 nm) • Generator operation: 50 kV and 30 mA • Measurement settings: 2θ range = 10 to 90°, step size = 0.017° and time per step = 15 s
Raman spectrometer: • T64000 micro-Raman spectrometer (HORIBA Scientific, Jobin Yvon Technology) • WiTec alpha300R confocal Raman microscope	• Laser wavelength: 514 nm • Laser power: 3 mW • Spectral acquisition time: 120 s • Objective: 100x/0.9 • Laser wavelength: 532 nm • Laser power: 4.0 mW • Spectral acquisition time: 10 s • Objective: 100x/0.9
	•
SEM: Zeiss Ultra Plus 55 field emission scanning electron microscope equipped with EDS	• Voltage: 2.0 kV
TEM: Jeol JEM-2100F Field Emission Electron Microscope	• Voltage: 200 kV
XPS: Physical Electronics VersaProbe 5000 spectrometer	• Beam voltage: 10 kV

3.4 Electrochemical characterizations

All electrochemical analysis were carried out on a Biologic VMP-300 potentiostat (Knoxville TN 37,930, USA) controlled by the EC-Lab V10.37 software at room temperature. In the three-electrode system, a glassy carbon plate was used as the counter electrode and Ag/AgCl (3 M KCl) electrode served as the reference electrode. The electrochemical performance of the electrodes was evaluated in both three and two electrode setup using the settings listed in table 3.2.

Table 3.2. *Electrochemical analysis settings for three and two electrode setup.*

Experiments	Settings
Cyclic voltammetry	• Scan rates: 5 to 100 mV s^{-1} in the • Potential (three-electrode) range: 0.0 – 1.1 V and -1.1 –0.0 V vs. Ag/AgCl; Cell potential (two-electrode) range: 0.0 – 2.2 V
Galvanostatic charge/discharge	• Specific current: 1 – 10 A g^{-1} • Potential (three-electrode) range: 0.0 – 1.1 V and -1.1 –0.0 V vs. Ag/AgCl; Cell potential (two-electrode) range: 0.0 – 2.2 V
Electrochemical impedance spectroscopy	• Frequency: 10 mHz to 100 kHz (Open circuit potential)

3.4.1 Preparation of the working electrodes

The working electrode of MnO_2-C composite was prepared by coating a mixture of 80 wt% active material, 10 wt% carbon black for conductivity enhancement and 10 wt% polyvinylidene fluoride (PVDF) binder dispersed in N-methylpyrrolidone (NMP) solution onto a piece of nickel foam (1 × 1 cm^2), as illustrated in figure 3.11. The slurry was coated on both sides of

the current collector for three-electrode and on one side for two-electrode measurements. After pasting, the electrode was dried at 60 °C overnight, and thereafter, the coated active material was pressed onto the nickel foam under a pressure of 30 MPa.

The C-Fe/PANI/Ni-GF working electrode was prepared as discussed in the synthesis method (see figure 4.2). Similar to preparation of MnO_2-C composite, the slurry was coated on both sides of the current collector for three-electrode and on one side for two-electrode measurements.

The masses of the working electrodes (both positive and negative) ranged between 2 and 4 mg. The electrochemical measurements of MnO_2-C composite and C-Fe/PANI/Ni-GF electrodes were carried out in the three-electrode system in 2.5 M KNO_3 and 1M NaNO3 electrolytes.

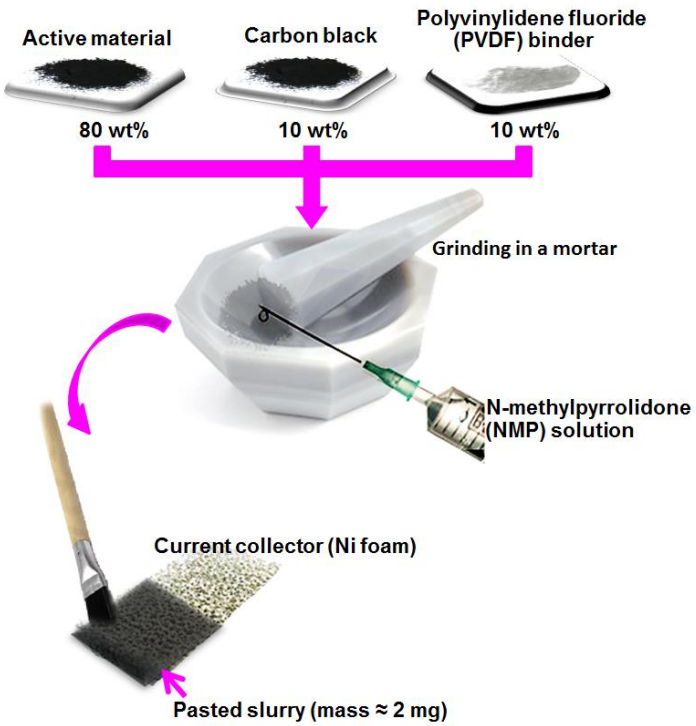

Figure 3.11. *Process scheme for MnO_2-C composite electrode preparation by coating a mixture of active material, carbon black and PVDF binder dispersed in NMP solution onto a piece of nickel foam[10].*

3.4.2 Fabrication of the supercapacitor device

The two electrode measurements were assembled using coin-type cell as illustrated in figure 3.12. The supercapacitor devices were fabricated based on MnO_2-C composite as a positive electrode and C-Fe/PANI/Ni-GF as a negative electrode (asymmetric supercapacitor) and C-Fe/PANI/Ni-GF electrode as both positive and negative electrode (symmetric supercapacitor) using 2.5 M KNO_3 and 1M NaNO3 electrolytes, respectively. Due to the difference in the specific capacity of the electrodes in positive and negative potential window, a charge balance, $Q_+ = Q_-$ was done (see equation 7 in chapter 2). Based on this, the mass balance between the electrode in positive and negative potential window was achieved and for MnO_2-C//C-Fe/PANI/Ni-GF asymmetric supercapacitor the mass ratio was $m_+/m_- \approx 4$, and for C-Fe/PANI/Ni-GF//C-Fe/PANI/Ni-GF symmetric supercapacitor the mass ratio was $m_+/m_- \approx 1$. The electrochemical performance of the fabricated supercapacitor devices was evaluated using the settings listed in table 3.2.

Figure 3.12. *Schematic illustration of the assembled structure of supercapacitor device.*

REFERENCES

[1] Y. Song, J. Wang, Z. Li, D. Guan, T. Mann, Q. Liu, M. Zhang, L. Liu, Self-assembled hierarchical porous layered double hydroxides by solvothermal method and their application for capacitors, Microporous Mesoporous Mater. 148 (2012) 159–165. doi:10.1016/j.micromeso.2011.08.013.

[2] Z. Gao, J. Wang, Z. Li, W. Yang, B. Wang, M. Hou, Y. He, Q. Liu, T. Mann, P. Yang, M. Zhang, L. Liu, Graphene nanosheet/Ni2+/Al3+ layered double-hydroxide composite as a novel electrode for a supercapacitor, Chem. Mater. 23 (2011) 3509–3516. doi:10.1021/cm200975x.

[3] J.R. Creighton, P. Ho, Chapter 1 Introduction to Chemical Vapor Deposition (CVD), Chem. Vap. Depos. (2001) 1–13.

[4] J. Fei, J. Zhao, H. Zhang, A. Wang, C. Qin, P. Cai, X. Feng, J. Li, One-pot mass self-assembly of MnO2 sponge-like hierarchical nanostructures through a limited hydrothermal reaction and their environmental applications, J. Colloid Interface Sci. 490 (2017) 621–627. doi:10.1016/j.jcis.2015.07.076.

[5] S.R.S. B.D. Cullity, Elements of X-Ray diffraction, 3rd ed., Prentice Hall, New Jersey, 2001.

[6] A.C. Ferrari, D.M. Basko, Raman spectroscopy as a versatile tool for studying the properties of graphene., Nat. Nanotechnol. 8 (2013) 235–46. doi:10.1038/nnano.2013.46.

[7] H. Aoki, M. S. Dresselhaus, eds., Physics of Graphene, Springer, New York, 2014.

[8] C. Casiraghi, A. Hartschuh, E. Lidorikis, H. Qian, H. Harutyunyan, T. Gokus, K.S.

Novoselov, A.C. Ferrari, Rayleigh imaging of graphene and graphene layers., Nano Lett. 7 (2007) 2711–7. doi:10.1021/nl071168m.

[9] T.D.H. Toporski, ed., Confocal Raman Microscopy, Springer, Heidelberg, 2010.

[10] H.J. Butler, L. Ashton, B. Bird, G. Cinque, K. Curtis, J. Dorney, K. Esmonde-White, N.J. Fullwood, B. Gardner, P.L. Martin-Hirsch, M.J. Walsh, M.R. McAinsh, N. Stone, F.L. Martin, Using Raman spectroscopy to characterize biological materials, Nat. Protoc. 11 (2016) 664–687. doi:10.1038/nprot.2016.036.

[11] M.J. Madito, A. Bello, J.K. Dangbegnon, C.J. Oliphant, W.A. Jordaan, D.Y. Momodu, et al., A dilute Cu(Ni) alloy for synthesis of large-area Bernal stacked bilayer graphene using atmospheric pressure chemical vapour deposition, J. Appl. Phys. 119 (2016) 015306. https://doi.org/10.1063/1.4939648.

[12] R.F. Egerton, Physical Principles of Electron Microscopy: An Introduction to TEM, SEM, and AEM, Springer Science & Business Media, 2006.

[13] A.R.S. Poole, Charles P, Owens Frank J, Introduction to Nanotechnology, Phys. Today. 57 (2004) 62–63. doi:10.1063/1.1809098.

[14] A.W. Robertson, J.H. Warner, Atomic resolution imaging of graphene by transmission electron microscopy., Nanoscale. 5 (2013) 4079–93. doi:10.1039/c3nr00934c.

[15] Y. Zhang, T. Tang, C. Girit, Z. Hao, M.C. Martin, A. Zettl, et al., Direct observation of a widely tunable bandgap in bilayer graphene, Nature. 459 (2009) 820-823. https://doi.org/10.1038/nature08105.

[16] M.P. Seah, Quantification of AES and XPS, in: D. Briggs, M.P. Seah (Eds.), Pract.

Surf. Anal. by Auger X-Ray Photo- Electron Spectrosc., 2nd ed., John Wiley & Sons Ltd., Chichester, 1990.

SECTION 4

RESULTS, DISCUSSION, AND CONCLUSION

Chapter 4

Results and discussion

4.1 Introduction

This chapter presents experimental findings on the structural and morphological characterization of the as-prepared electrode materials (C-Fe/PANI/Ni-GF and birnessite-type MnO_2/carbon composite). It also includes the electrochemical properties of the as-fabricated devices C-Fe/PANI/Ni-GF//C-Fe/PANI/Ni-GF and MnO_2-C//C-Fe/PANI/Ni-GF, symmetric and asymmetric device, respectively. The publication from each research study will also be presented.

4.2 High-performance symmetric supercapacitor device based on carbonized iron-polyaniline/nickel graphene foam

4.2.1 Summary

A comparison of the results for C-Fe/PANI/Ni-GF electrode, and C-Fe/PANI electrode confirms a successful synthesis of C-Fe/PANI/Ni-GF electrode. The results for the C-Fe/PANI/Ni-GF//C-Fe/PANI/Ni-GF symmetric device, fabricated as described in chapter 3, reveals the excellent electrochemical performance of the device.

The results are discussed in the attached published paper below in *Journal of Alloys and Compounds*.

4.2.2 Publication

Journal of Alloys and Compounds 819 (2020) 152993

Contents lists available at ScienceDirect

Journal of Alloys and Compounds

journal homepage: http://www.elsevier.com/locate/jalcom

High-performance symmetric supercapacitor device based on carbonized iron-polyaniline/nickel graphene foam

M.N. Rantho, M.J. Madito, N. Manyala*

Department of Physics, Institute of Applied Materials, SARChI Chair in Carbon Technology and Materials, University of Pretoria, 0028, South Africa

ARTICLE INFO

Article history:
Received 7 December 2018
Received in revised form
22 October 2019
Accepted 11 November 2019
Available online 12 November 2019

Keywords:
Supercapacitor
Symmetric device
Negative electrode
PANI
Graphene foam

ABSTRACT

The carbonized iron-polyaniline/nickel graphene foam (C–Fe/PANI/Ni-GF) electrode was prepared by pasting a mixture of iron-polyaniline (Fe/PANI) on nickel graphene foam (Ni-GF) and carbonized under the nitrogen. For electrochemical characterization, the as-prepared electrode material was evaluated in both three and two-electrode (i.e. symmetric) cell configurations using 1 M $NaNO_3$ electrolyte. The symmetric device exhibited a maximum energy density of 68.0 W h kg^{-1} and power density of 718.2 W kg^{-1}, at a specific current of 1.0 A g^{-1} and the maximum potential of 1.7 V. The device further displayed long-term cycling stability with capacity retention of 91% over 10 000 galvanostatic charge-discharge cycles at 5 A g^{-1}. The stability of the device was also tested using the voltage holding and self-discharge approach whereby a slow-discharging process was observed, which suggests the practical application of the device.

1. Introduction

Recently, there has been a demand for high-power performance, long cycle life, and enhanced safety energy-storage systems. In the view of the demands for energy-storage systems, supercapacitors (SCs) have received great attention due to their properties/electrochemical performance. SCs are high-power performance devices, and an extent of extensive research on SCs has been focusing on improving the energy density of SCs. In SCs, charges can be stored using three different mechanisms, viz., electric double-layer capacitors (EDLCs), pseudocapacitors or redox SCs and hybrid capacitors [1–3]. Asymmetric (hybrid) capacitors have been explored to increase the operating potential window to improve the energy density of the SCs [1–3]. Nowadays, ionic liquid electrolytes have been considered to provide the alternative improvement on SCs (high operating potential window) since they have a wider electrochemical stability window [4]. The main focus is also on developing hybrid SCs using the pseudocapacitive electrodes and battery-electrode materials since they exhibit high capacitance [[5,6]]. Therefore, both the high operating potential window and high capacitance of the pseudocapacitive electrodes and battery-electrode material significantly increase the energy density of the SCs while maintaining high power density. In addition, the development of the nanostructured materials has been explored to improve the rate capability of the battery-electrode materials.

In recent reports, conducting polymers are considered as pseudocapacitive materials suitable for the next generation of SCs [7–10]. Among these conducting polymers, polyaniline (PANI) has attractive properties, for instance, the morphological diversity, good redox reversibility, low cost, and simple synthesis [11]. The conducting polymers have a wide range of tunable properties since their conductivity is linked with the molecular structure, the level of doping and the ordering of molecular packing [12–14]. It has been shown that PANI containing iron achieves high electrocatalytic and electrochemical performance with long-cycling stability [15–17]. Iron cations easily adsorb onto PANI due to functional groups of PANI which acts as active sites [18–21]. Available reports also show that the electrical conductivity of PANI can be enhanced by carbon nanotubes through π–π interactions [22,23]. However, compared to graphene the mass production of carbon nanotubes has a higher production cost hence graphene is preferred. Moreover, graphene has attracted great attention due to its remarkable properties, for instance, a high specific surface area, high electrical conductivity, and chemical stability [24–29]. Polymer/graphene interactions (nanocomposites) are expected to exhibit excellent electrochemical performance owing to a stronger π–π conjugation interactions and graphene properties. In fact, Yu et al. [30] have reported a remarkably high capacitance value of

* Corresponding author.
E-mail address: ncholu.manyala@up.ac.za (N. Manyala).

https://doi.org/10.1016/j.jallcom.2019.152993
0925-8388/

1341 F g^{-1} for a PANI/3D graphene framework in an acidic electrolyte. Wang et al. [31], have demonstrated that the PANI/graphene nanocomposites show much better capacitance performance than that of individual PANI and the synergy effect of PANI and graphene greatly improves the retention life of the composite material. The key factors determining the electrochemical performances of the PANI/graphene nanocomposites, such as morphologies, synthesis methods, and synthesis conditions are detailed in the review titled: Polyaniline/graphene nanocomposites towards high-performance supercapacitors by Huang et al. [32].

This study reports on a high-performance symmetric supercapacitor based on the carbonized iron-polyaniline/nickel graphene foam electrode; prepared as shown in Scheme 1. The symmetric supercapacitor device was fabricated using 1 M $NaNO_3$ aqueous electrolyte. The C—Fe/PANI/Ni-GF symmetric device showed good electrochemical performance with a high energy density of 68.0 W h kg^{-1} and power density of 718.2 W kg^{-1}, at a specific current of 1.0 A g^{-1}; and excellent stability for both cycling and voltage holding stability test. The self-discharge approach was also used to test the stability of the device which showed a slow self-discharge process.

2. Experimental

2.1. Carbonization of an iron-polyaniline mixture on nickel graphene foam

The Fe-PANI mixture was synthesized as reported in our recent work [17]. Briefly, a 0.4 g of PANI and 0.2 g of iron nitrate nonahydrate ($Fe(NO_3)_3 \cdot 9H_2O$) were dissolved in a 50 mL of ethanol and dispersed until the Fe-PANI slurry was formed. The slurry was pasted on graphene supported by nickel foam and carbonized at 850 °C (ramp rate of 10 °C min^{-1}) for 2 h under nitrogen. After carbonization, the difference in the micrograph of the Ni-GF and that of Fe-PANI mixture on Ni-GF (C—Fe/PANI/Ni-GF) confirms a successful synthesis of the electrode which is expected to have strong metal-polymer/graphene interactions (see Scheme 1). The as-prepared electrode material was used for both negative and positive electrode, respectively. For electrochemical characterization in three-electrode configuration, the Fe-PANI slurry was pasted on both sides of Ni-GF and after carbonization, the active material of the electrode had a mass of 2 mg. For the symmetric device fabrication, the slurry was only pasted on one side of Ni-GF and after carbonization; the electrode materials had masses of 1.5 mg (negative electrode) and 1.7 mg (positive electrode).

The Ni-GF was grown using atmospheric pressure chemical vapour deposition (AP-CVD). Graphene growth was carried out for 10 min at 1000 °C using a mixture of gasses, Ar: H_2: CH_4 with flow rates of 300: 200: 10 sccm, respectively. All the reagents used were purchased from Sigma Aldrich and a 3D scaffold template of polycrystalline nickel foam (Ni—F) from Alantum.

2.2. Morphological, composition and structural characterization

The C—Fe/PANI/Ni-GF material was characterized using scanning electron microscopy (SEM, Zeiss Ultra Plus 55 field emission scanning electron microscope), energy-dispersive X-ray spectrometer (EDS), high-resolution transmission electron microscopy (HR-TEM), X-ray diffractometer (XRD, XPERTPRO diffractometer (PANalytical BV, Netherlands) and Raman spectroscopy. The HR-TEM analysis was carried out in a high-resolution transmission electron microscopy JEOL 2100 (from Tokyo Japan) equipped with LaB_6 filament, a Gartan U1000 camera of 2028 x 2028 pixels and was operated at 200 kV. The HR-TEM scanning transmission electron microscopy and the energy dispersive X-ray (STEM-EDX) were used for elemental distribution analysis. WITec alpha300 RAS + confocal Raman microscope was used for Raman analysis/imaging. The analysis was carried out using a 532 nm laser and laser power of 5 mW. Raman image scans were acquired over 30 × 30 μm^2 area with 100 points per line and 100 lines per image using an integration time of 5 s. WITec project plus version software was used for Raman data processing.

2.3. Electrochemical characterization

A Biologic VMP-300 potentiostat (Knoxville TN 37 930, USA) was used for the electrochemical characterization. For three-electrode configuration, the measurements were carried out using three different neutral aqueous electrolytes, i.e. 1 M $NaNO_3$, $NaSO_4$ and $LiSO_4$ electrolyte. Cyclic voltammetry (CV) at scan rates of 5—100 mV s^{-1} and galvanostatic charge-discharge (GCD) were carried out for positive and negative electrode in the potential range of 0.0—0.7 V vs. Ag/AgCl and −1.0 to 0.0 V vs. Ag/AgCl. The electrochemical impedance spectroscopy (EIS) analysis was obtained using an open circuit over 10 mHz to 100 kHz. For two-electrode measurements, the symmetric device was fabricated using 1 M $NaNO_3$ aqueous electrolyte.

3. Results and discussion

3.1. Morphological, composition and structural characterization

The morphologies of the Ni-GF and C—Fe/PANI/Ni-GF samples

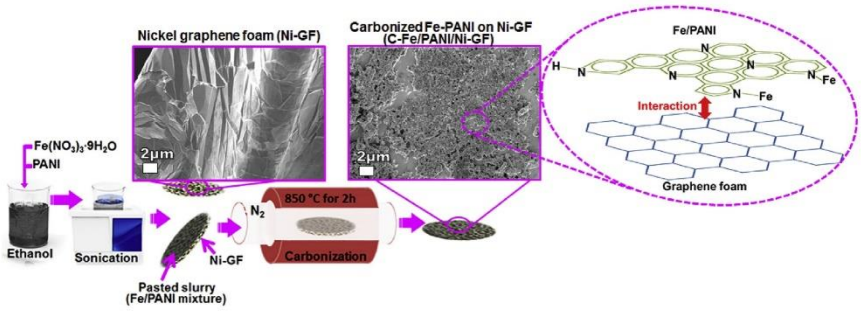

Scheme 1. The synthesis route for carbonized iron-polyaniline/nickel graphene foam electrode.

were examined using SEM, as shown in Fig. 1(a)–(b), respectively. From the SEM images, the Ni-GF displays wrinkles and ripples of as-grown graphene [33]. The C–Fe/PANI/Ni-GF sample comprises of agglomerated nanograins; this is also shown in high magnification image in Fig. 1(c). The elemental composition of the C–Fe/PANI/Ni-GF was obtained using EDS and the maps are displayed in Fig. 1(d). Fig. 1(d) shows the EDS maps of Ni, C, Fe, N, S, and O. Fig. 1(e) shows the secondary electron beam image with an overlay combined image of the EDS maps of evaluated elements. These maps suggest that Fe cations are distributed homogeneously on the PANI matrix in the C–Fe/PANI/Ni-GF electrode material. Fig. 1(f) displays the average EDS spectrum which shows Fe, S, O, N, C, and Ni. A high content of Ni result from the Ni-GF substrate. The presence of S in the sample is from PANI synthesis, ammonium persulphate in particular, which degraded during pyrolysis. In addition, O and N are typically found in PANI. The XRD pattern obtained from the carbonized Fe/PANI (Fig. S1), shows the diffraction peaks which matches Fe_3C, FeS, Fe and (002) graphitic plane.

Fig. 2(a)–(b)-(c) show high-resolution TEM images of the as-synthesized C–Fe/PANI (without Ni foam) and C–Fe/PANI/Ni-GF, respectively. From these figures, C–Fe/PANI shows Fe cations attributed to Fe_3C, FeS and Fe anchored on PANI which has a sheet-like morphology. On the other hand, C–Fe/PANI/Ni-GF shows Fe/PANI on graphene foam (GF) which is grown on Ni substrate. In Fig. 2(c), GF shows a thickness of about 5 nm corresponding to few-layer graphene. Furthermore, a scanning transmission electron microscopy along with energy dispersive X-ray maps are displayed in Fig. 2(d)–(e)–(j), respectively. The energy dispersive X-ray maps of the as-synthesized C–Fe/PANI/Ni-GF sample display the main elements of the sample (C, N, O, S, Fe and Ni) as seen from the EDS maps in Fig. 1.

Before pasting a slurry of Fe/PANI on the Ni-GF (see Scheme 1), a Ni-GF was analyzed using Raman spectroscopy to investigate the quality and the number of graphene layers in the as-grown graphene. Fig. 3(a–c) shows the Raman data of graphene on Ni foam. The main features of the Raman spectrum of graphene are the G-band (~1590 cm^{-1}), the 2D-band (~2690 cm^{-1}) and the D-band (disorder-induced band, 1350 cm^{-1}) [34–36]. In Fig. 3(a), the overlay image of the cluster analysis on the optical microscope image of the sample and the corresponding cluster average spectra (Fig. 3(b)) reveals that the as-grown graphene has significant fractions of monolayer, bilayer and few-layer graphene (i.e. « 10 monolayers). Certainly, Fig. 3(b) shows the typical Raman spectrum of monolayer, bilayer and few-layer graphene with 2D-to-G peaks intensity ratios of >2, ~1 and < 0.6, respectively. In addition, the 2D peaks Full Width at Half Maximum (FWHM) for monolayer, bilayer and few-layer graphene are 30, 50 and 72 cm^{-1}, respectively, which demonstrate the characteristics of monolayer, bilayer and few-layer graphene. Briefly, the cluster analysis of the acquired Raman image data set automatically finds similar spectra in an image spectrum data set and creates the cluster distribution maps and the corresponding cluster average spectra. Furthermore, Fig. 3(c) shows the mapping of the D-to-G peaks intensities ratio. The map shows an average value of approximately zero confirming the zero intensity of the D-band in the Raman spectra which demonstrates high-quality graphene foam.

Fig. 3(d–g) shows the Raman data of the C–Fe/PANI/Ni-GF. In Fig. 3(d), the overlay image of the cluster analysis on the optical microscope image and the corresponding cluster average spectra (Fig. 3(e)) display typical Raman spectra of PANI (blue line) and

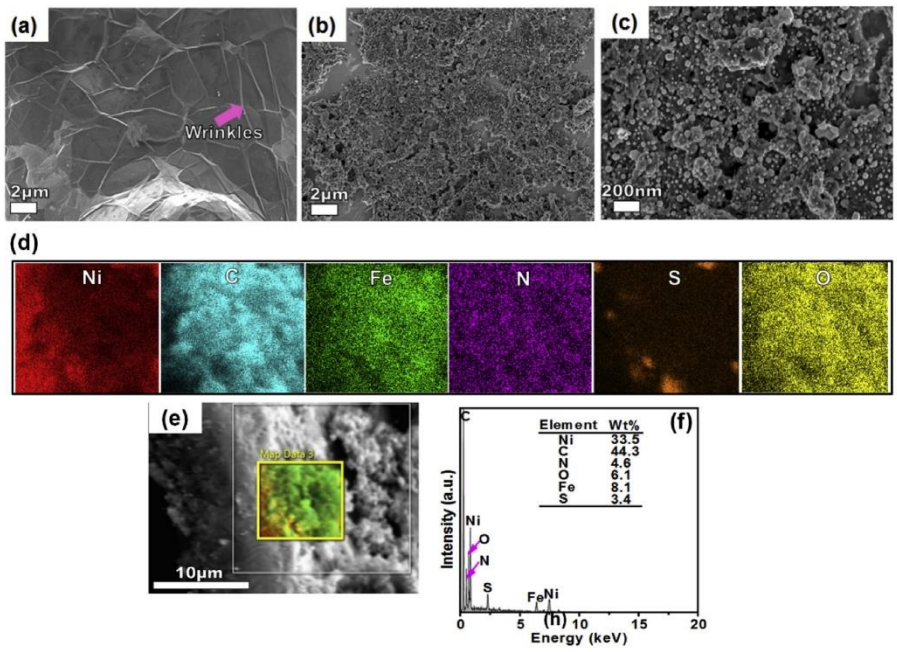

Fig. 1. (a) SEM image of the Ni-GF and (b) C–Fe/PANI/Ni-GF. (c) The high magnification image of the C–Fe/PANI/Ni-GF. (d) The EDS maps of Ni, C, Fe, N, S, and O, and (e) the corresponding secondary electron beam image with an overlay combined image of the EDS maps of evaluated elements. (f) An average EDS spectrum.

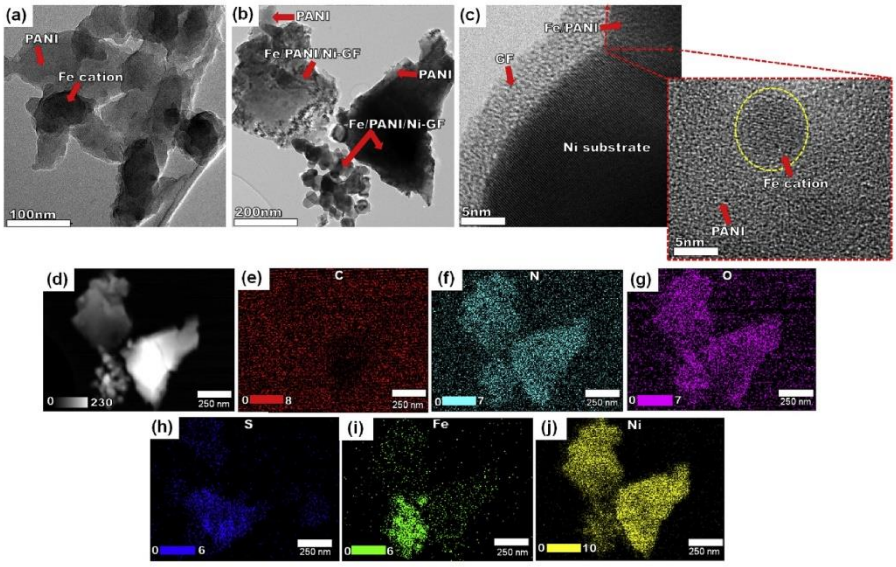

Fig. 2. High-resolution TEM images: (a) As-synthesized C–Fe/PANI (without Ni foam), (b) and (c) C–Fe/PANI/Ni-GF. (d) Scanning transmission electron microscopy image and (e)–(j) the corresponding energy dispersive X-ray maps of C, N, O, S, Fe and Ni obtained from the as-synthesized C–Fe/PANI/Ni-GF sample.

graphene (green and pink line). From the overlay image in Fig. 3(d), the small areas of graphene suggest that the coating of the PANI on Ni-GF is not completely uniform across the substrate and that could be due to the porous nature of the Ni foam. Moreover, in Fig. 3(e), the D band (which is due to the functional groups of PANI [20,21]) in the spectra of graphene confirms the interaction/incorporation of the PANI functional groups in the graphene lattice. This is further confirmed by mapping of the D-to-G peaks intensities ratio, as shown in Fig. 3(f), which displays an average value of ~0.8. This confirms a high intensity of the D-band in the Raman spectra of the C–Fe/PANI/Ni-GF.

The Raman peaks in the range of 100–700 cm^{-1} are due to Fe–PANI, as shown in Fig. 3(g) and Table 1. It is worth mentioning that the phases in Fig. 3(g) have X-ray diffraction peaks matching Inorganic Crystal Structure Database (ICSD) cards (α-S_8 ICSD #27261, α-FeOOH ICSD #77327, γ-FeOOH ICSD #93948, Fe_2O_3 ICSD #64599 and Fe_3O_4 ICSD #35000) which overlap with the diffraction peaks of the phases shown in the XRD data in Fig. S1.

In Fig. 4(a), the C 1s XPS core level spectrum of the C–Fe/PANI/Ni-GF shows different carbon compounds at 284.5 (C=C), 285.3 (C–C), 286.5 (C–OH/C–N), 287.6 (C–O–C) and 288.9 eV (C=O) attributed to the functional groups of PANI [43,44]. On the other hand, compared to the C–Fe/PANI/Ni-GF, the C 1s spectrum of the Ni-GF (Fig. 4(b)) shows a predominant narrow peak of sp^2 C=C bond and relatively low-intensity peaks of the oxide components which could be due to surface-adsorbed CO_2 and O_2, and the $\pi-\pi^*$ electrons transition [45–47]; and this shows a form of high-quality graphene. Nonetheless, in the C–Fe/PANI/Ni-GF, the C 1s spectrum of the Ni-GF would be similar to that of the C–Fe/PANI/Ni-GF due to the interaction between the Fe/PANI and graphene foam during pyrolysis which is energetically favourable owing to the unpaired π-electron in graphene and the high electronegativity of oxygen present in PANI. The Fe 2p XPS core level spectrum of the C–Fe/PANI/Ni-GF (Fig. 4(c)) shows fitted Fe $2p_{3/2}$ binding energy peaks at 706.5 and 708.1eV attributed to Fe^0 (metallic Fe)/Fe^{2+} and Fe^{3+} ions, respectively [48]. In Fig. 4(d), the N 1s core level spectrum shows characteristic nitrogen–carbon bond-related peaks which appears at 398.6 eV (pyridinic N), 400.2 eV (pyrrolic N), and 401.5 eV (graphitic N). A pyridinic N peak has the contribution of N–iron peak (399.3 eV) since the two peaks overlap [49]. The S 2p XPS core level spectrum shows peaks in the range of 160–65 eV attributed to the S^{2-} ions (160.7 and 161.9 eV fitted peaks of the S $2p_{3/2}$ and S $2p_{1/2}$ levels, respectively), S–C and/or S–S bonds (fitted peak at 163.3 eV of the S $2p_{3/2}$ level). S $2p_{1/2}$ fitted peak confirms a characteristic FeS bond-related peak which appears at 161.9 eV and in the S $2p_{3/2}$ peak, S–C, S–S and S–S/S–C bonds have characteristic peaks at 163.2, 163.8, and 164.8 eV respectively [50].

3.2. Electrochemical characterization

The as-prepared electrodes (C–Fe/PANI/Ni-GF) were evaluated as negative and positive electrodes using 1 M $NaNO_3$, $NaSO_4$ and $LiSO_4$ electrolyte in the three-electrode system, as shown in Fig. 5(a)–(b). The CV curves of the as-prepared electrode in both negative and positive potential window show pseudocapacitive behavior without obvious redox peaks. From Figs. 5 and 1 M $NaNO_3$ electrolyte is the best electrolyte since it gives high current response compared to that of 1 M $NaSO_4$ and 1 M $LiSO_4$ electrolyte. This could be due to the small hydrated ion size of Na^+ (0.359 nm) and high ionic conductivity of 50.11 S cm^2 mol^{-1} compared to the Li^+ which has ion size of 0.381 nm and ionic conductivity of 38.69 S cm^2 mol^{-1} [51,52]. On the other hand, The accumulation of NO_3^- ions on the positive electrode might be higher than that of SO_4^{2-} ions since it has small hydrated ion size of 0.335 nm compared to 0.379 nm of the SO_4^{2-} ions [52]. It worth mentioning that the negative electrodes in 1 M $NaSO_4$ and 1 M $LiSO_4$ electrolyte could not reach a potential of 1.0 V vs. Ag/AgCl as the electrode in 1 M $NaNO_3$ electrolyte.

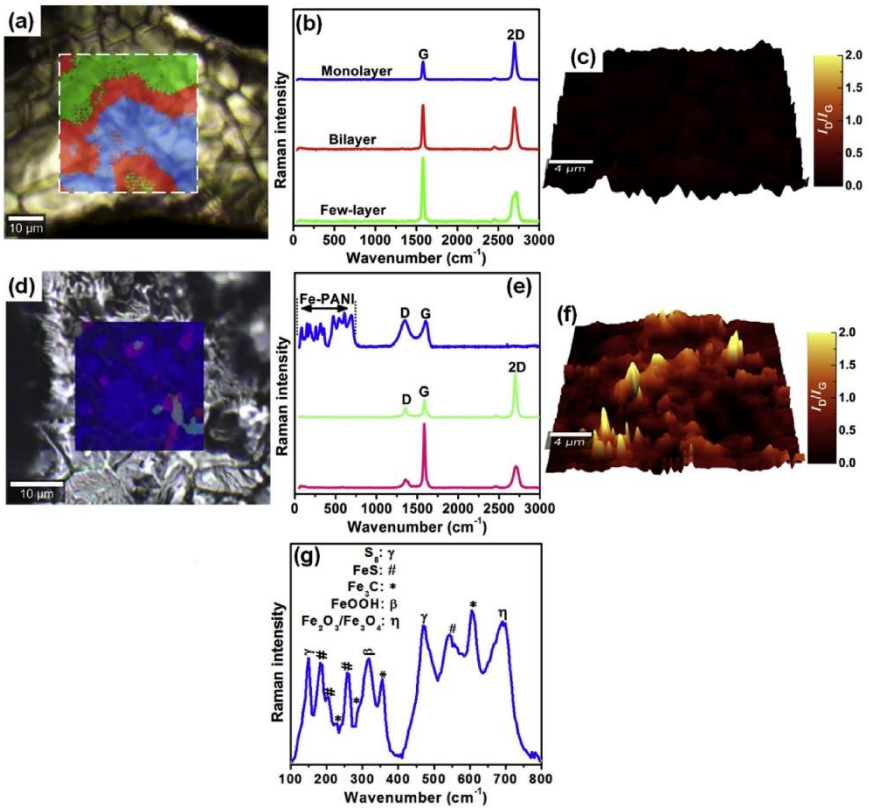

Fig. 3. (a–c) Raman data of as-grown graphene on Ni foam (Ni-GF): (a) The optical microscope image with an overlay image of cluster analysis, and (b) the corresponding cluster average spectra (each spectrum-color correspond to the image area of the same color in (a)). (c) Mapping of the D-to-G peaks intensities ratio. (d–g) Raman data of C–Fe/PANI/Ni-GF: (d) The optical microscope image with an overlay image of cluster analysis, and (e) the corresponding cluster average spectra (each spectrum-color correspond to the image area of the same color in (d)). (f) Mapping of the D-to-G peaks intensities ratio. (g) The cluster average spectrum of the Fe-PANI range in (e). (For interpretation of the references to color in this figure legend, the reader is referred to the Web version of this article.)

Table 1
Raman peak positions of the Fe-PANI range in Fig. 3(g) of the C–Fe/PANI/Ni-GF and the corresponding phases.

Peak positions (cm^{-1})	Phases	Ref.
153	α-S_8	[37]
191	FeS	[38]
205	FeS	[38,39]
223	Fe_3C/α-S_8	[39,40]
265	FeS	[38,39]
290	Fe_3C/FeS	[39,40]
310	α-FeOOH	[41]
360	Fe_3C/γ-FeOOH	[39,40]
471	α-S_8	[37]
540	γ-FeOOH	[39]
603	Fe_3C	[40]
680	γ-Fe_2O_3/Fe_3O_4	[41,42]

Based on the observation from Figs. 5 and 1 M $NaNO_3$ electrolyte showed the best performance compared to the other electrolytes it was used for further electrochemical evaluation. The as-prepared electrode was further evaluated in the three electrode configuration using 1 M $NaNO_3$ electrolyte, as shown in Figs. S2(a–d). For as-prepared electrode the specific capacitance, C_S, was calculated for both positive and negative electrode (Fig. S2(e)), from the GCD curves [3,53,54]:

$$C_S = \frac{I\Delta t}{m\Delta V} \quad (1)$$

where I/m is the specific current (A/g), m is the mass of the electrode material (g), Δt is the discharge time (s), and ΔV is the maximum potential.

From Fig. S2(e) it can be seen that in the positive potential window, the as-prepared electrode exhibited the high specific capacitance of 69.0 F g^{-1} at a specific current of 1 A g^{-1} and in the negative potential window it exhibits 139.9 F g^{-1}. For the as-prepared electrode, a symmetric supercapacitor device (scheme in Fig. 6(a)) was fabricated using 1 M $NaNO_3$ electrolyte; and the charge balance was done using equation S(1) (supporting information). From the three-electrode measurements (Fig. 6(b)), the as-

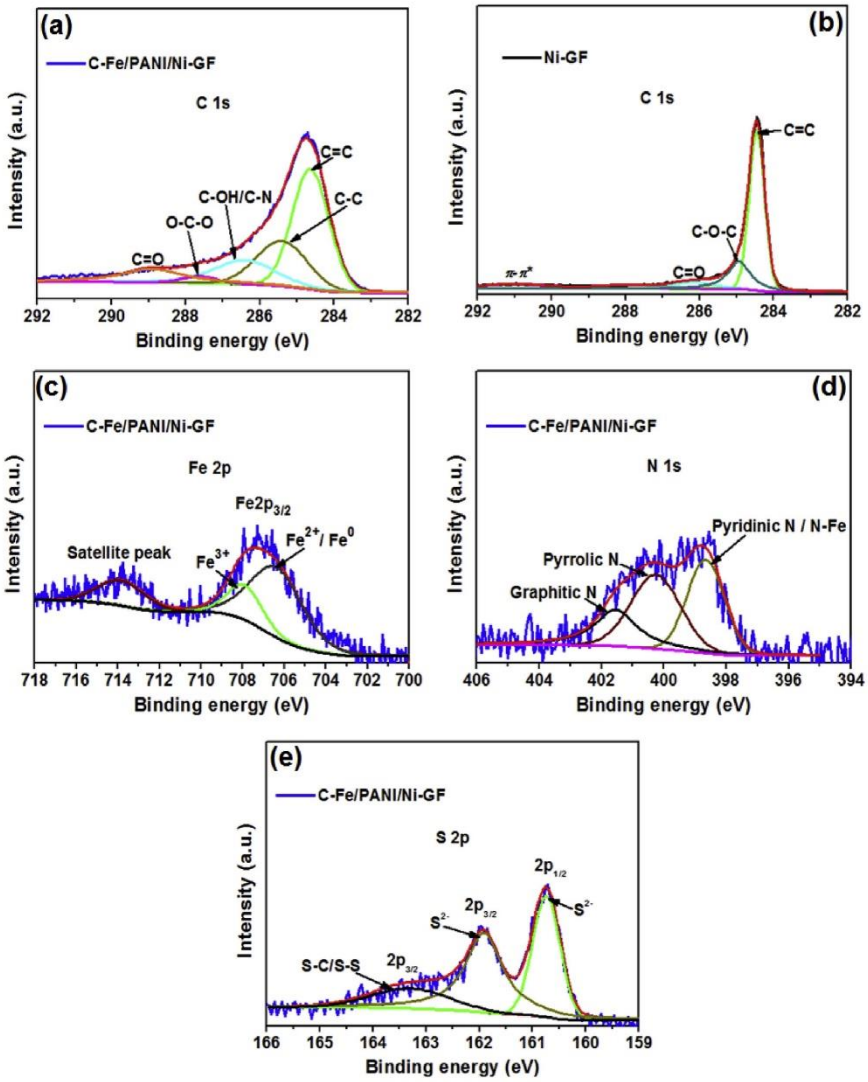

Fig. 4. The XPS core level spectra: (a) C 1s of the C–Fe/PANI/Ni-GF and (b) Ni-GF; (c) Fe 2p, (d) N 1s, and (e) S 2p of the C–Fe/PANI/Ni-GF electrode material.

prepared electrode in negative and positive potential window reaches −1.0 and 0.7 V vs. Ag/AgCl, respectively. Consequently, the symmetric device was able to reach the maximum potential of 1.7 V (Fig. 6(c)). It can be seen from the CV curves of the device (Fig. 6(c)) that it has a pseudocapacitive behavior; and these curves do not change with the increase in scan rate, which suggests that the device is stable. The GCD curves of the device shown in Fig. 6(d) at different specific currents in the range of 1–5 A g^{-1} which illustrates the pseudocapacitive behavior agreeing with the CV (Fig. 6(c)). Moreover, because of the pseudocapacitive nature of the device, the specific capacity (Q_S) of the device (Fig. 6(e)) was calculated using equation (2) [3,53–56]:

$$Q_S = \left(\frac{I}{m}\right)\frac{t}{3.6} \quad (2)$$

where I/m is the specific current (A/g), m is the mass of the electrode material (g), and t is the discharge time (s).

At a low specific current of 1 A g^{-1} the device exhibits a high specific capacity of 94.6 mA h g^{-1} which drops to 31.7 mA h g^{-1} at a

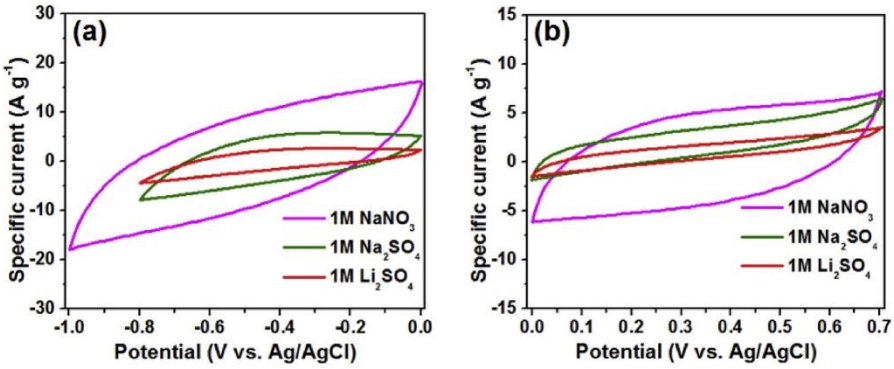

Fig. 5. (a) and (b) Cyclic voltammetry curves of the as-prepared electrode at the scan rate of 50 mV s^{-1} in different aqueous electrolytes.

high specific current of 5 A g^{-1}; such drop could be due to the limited time that ions have to access the surface of the electrode at high specific currents [57], and that could be due to the redox reactions (from the oxide phases present in the electrode) which limit the accessibility of the electrolyte ions. In addition, the observed drop in specific capacity values may be due to the increasing electronic field within the cell setup increased by an increase in the current density at a high cell potential window.

The energy density, E_d and the power density, P_d were calculated using the GCD curves, as shown in Fig. 7(a), using equations (3) and (4), respectively:

$$E_d \left(\mathrm{W\,h\,kg^{-1}}\right) = \left(\frac{I}{m}\right)\frac{\int V(t)dt}{3.6} \tag{3}$$

$$P_d \left(\mathrm{W\,kg^{-1}}\right) = \frac{3.6\ E_d}{\Delta t} \tag{4}$$

where I/m is the specific current (A/g), $\int V(t)dt$ is the integral under the discharge curve and Δt is the discharge time (s).

The fabricated device displayed a maximum energy density of 68.0 W h kg^{-1} and power density of 718.2 W kg^{-1}, at a specific current of 1.0 A g^{-1}. At a high power density of 3843.0 W kg^{-1}, the energy density remained as high as 24.4 W h kg^{-1} at 5.0 A g^{-1}. Fig. 7(b) shows the energy densities of the C–Fe/PANI (from our previous work [17]) and C–Fe/PANI/Ni-GF symmetric devices in the specific current range of 1.0–5.0 A g^{-1}. From the figure, the C–Fe/PANI/Ni-GF device shows higher energy density values compared to C–Fe/PANI device. Additionally, Table 2 and the Ragone plot (Fig. S3) also show that the energy and power densities for C–Fe/PANI/Ni-GF device are superior to those reported in the literature on PANI based symmetric devices. A high-performance of the C–Fe/PANI/Ni-GF device could be attributed to the synergy between Fe/PANI and graphene foam. Although the Ni-GF is well-recognized to possess high electrical conductivity compared to Ni foam, a high energy density exhibited by C–Fe/PANI/Ni-GF compared to C–Fe/PANI is mainly due to the synergistic effect of PANI and graphene and the contribution of the iron-composite layer. This is also reported in the literature that the PANI/graphene nanocomposites show much better capacitance performance than that of individual PANI and the synergy effect of PANI and graphene greatly improves the retention life of the composite material [30,31]. Also, studies have shown that iron-containing PANI, achieve high electrocatalytic performance and exhibit high cycling stability [58–60].

Fig. 7(c) shows the cycling stability test of the C–Fe/PANI/Ni-GF symmetric device performed at a specific current of 5.0 A g^{-1}. The cycling stability of the device exhibited a columbic efficiency of 99% and 91% capacity retention after a 10 000th galvanostatic charge-discharge cycle. In Fig. 7(d), the C–Fe/PANI/Ni-GF device shows a better cycling stability compared to C–Fe/PANI device [17], both performed at the same specific current of 5.0 A g^{-1}. This enhanced or long-cycling stability could also be due to the interactions between Fe/PANI and graphene foam. It is known that PANI–carbon (i.e., carbon nanotubes, nanofibers, graphene, etc.) based composites have long-cycling stability owing to the high stability of carbon [62,64–70]. The stability of the device was further tested via potentiostatic floating test (i.e. voltage holding) at 5.0 A g^{-1} and maximum operating potential of 1.7 V for 100 h, as shown in Fig. 7(e) and (f). Briefly, in voltage holding, a cell is kept at a specific fixed maximum operating potential for a long period of time, and the process includes a charge-discharge step for a few numbers of cycles in which the specific capacity of the device is monitored. Fig. 7(e) and (f) show a significant increase in the specific capacity and energy density of the device after voltage holding, and this could mean that the electrolyte ions access the electrodes pores more effectively after each holding period for intercalation into the electrode.

The electrical properties of the device before and after cycling stability, and after voltage holding were analyzed using EIS, as shown by the Nyquist plot in Fig. 8(a). In Fig. 8(a), the Nyquist plots do not show an obvious semi-circle in the high-frequency region (inset to the figure) demonstrating a lower electrode-electrolyte interface charge transfer resistance, R_{CT} hence a better capacitive behavior. The intersection of the Nyquist plots on the real component, Z' (see the inset to the figure), describes the equivalent series resistance, ESR or R_S, and the R_S values before stability ($R_S = 4.3\ \Omega$), after stability ($R_S = 5.5\ \Omega$) and after voltage holding ($R_S = 7.2\ \Omega$) are comparable suggesting good chemical stability of the device. A linear part of the plots (in the low-frequency) with angles greater than 45° deviates from an ideal capacitor. Furthermore, the Nyquist plot of the device was fitted (Fig. 8(b)) using the equivalent circuit diagram shown in the insert to Fig. 8(b). The equivalent circuit diagram presents R_S in series with R_{CT}, and Warburg impedance characteristic element, W parallel to the real capacitance (Q_1) [71]. A deviation of the supercapacitor behavior from an ideal capacitive behavior is attributed to a leakage resistance, R_L (i.e. parallel to the mass capacitance, Q_2) [72,73].

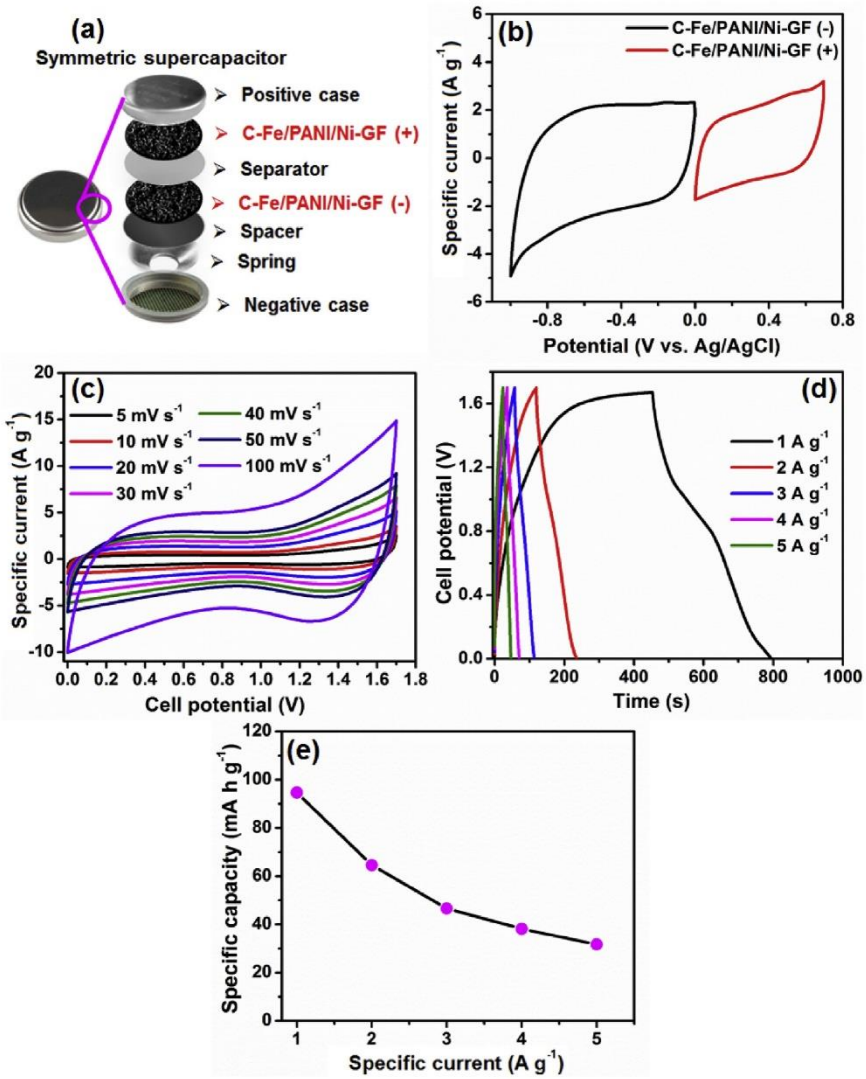

Fig. 6. (a) Scheme of the fabricated device. (b) CV curves of the as-prepared electrode from the three-electrode measurements at 5 mV s^{-1}. (c) and (d) CV and GCD curves of the fabricated device, respectively. (e) Specific capacity versus specific current for the device.

Moreover, Fig. 8(c) displays the phase angle value of −66° for the C−Fe/PANI/Ni-GF device. The frequency dependence of the $C'(\omega)$ and $C''(\omega)$ capacitances was calculated, as shown in Fig. 8(d), using the following expressions [74,75]:

The impedance, $Z(\omega)$ is expressed as

$$Z(\omega) = \frac{1}{j\omega \times C(\omega)} \quad (5)$$

Therefore,

$$C'(\omega) = \frac{Z''(\omega)}{\omega |Z(\omega)|^2} \quad (6)$$

$$C''(\omega) = \frac{Z'(\omega)}{\omega |Z(\omega)|^2} \quad (7)$$

where Z' and Z'' are defined as

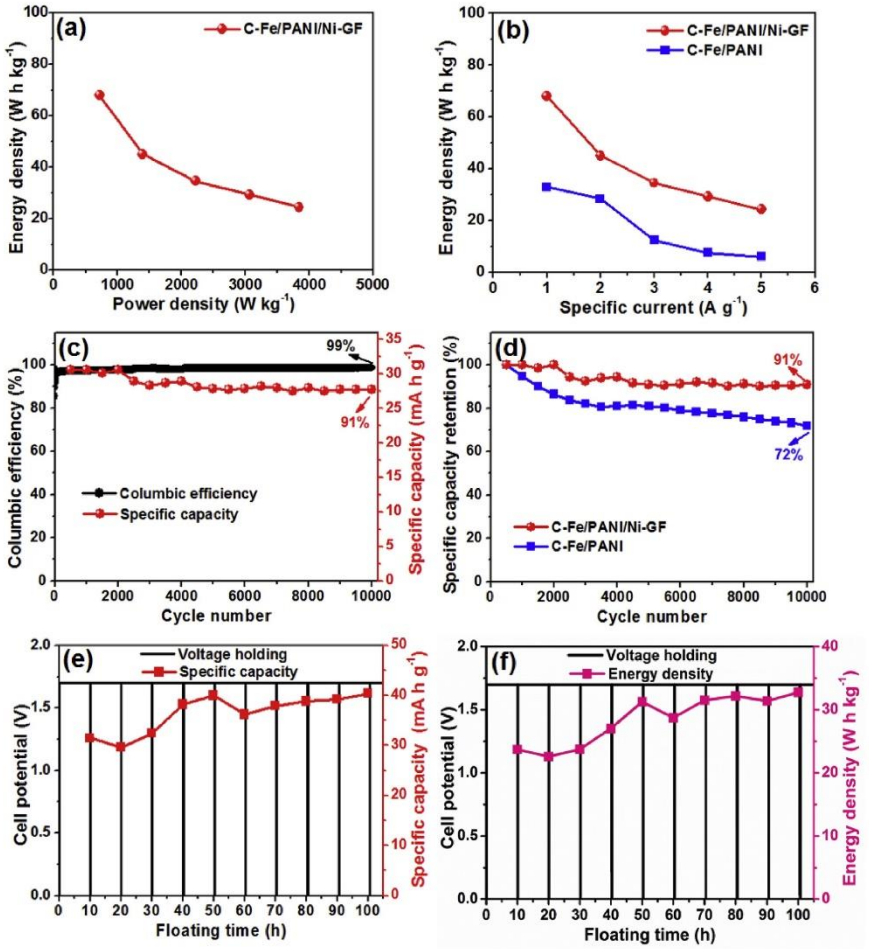

Fig. 7. (a) Energy and power densities of the C–Fe/PANI/Ni-GF device. (b) Energy densities of the C–Fe/PANI and C–Fe/PANI/Ni-GF symmetric devices versus specific current. (c) The cycling stability test for the C–Fe/PANI/Ni-GF device at a specific current of 5 A g^{-1}. (d) The cycling stability results of the C–Fe/PANI and C–Fe/PANI/Ni-GF symmetric devices at a specific current of 5 A g^{-1}. (e) Voltage holding and specific capacity as a function of floating time at 5 A g^{-1}. (f) Voltage holding and energy density as a function of floating time at 5 A g^{-1}.

Table 2
Electrochemical performance comparison of PANI based symmetric devices.

Electrode device	Electrolyte	Specific current ($A g^{-1}$)	Potential window (V)	Energy density ($W h kg^{-1}$)	Power density ($W kg^{-1}$)	Ref.
PANI	1 M H_2SO_4	1.0	1.0	23	180	M. Dirican et al., 2014 [61]
PANI/PCNF	1 M H_2SO_4	1.0	1.0	12	180	M. Dirican et al., 2014 [61]
PANI/MWNTs	1 M H_2SO_4	1 mA/cm^2	1.0	22	83	H. Mi et al., 2007 [62]
PANI/CNT	1 M H_2SO_4	0.5	0.8	7.11	201	K. Silas et al., 2016 [63]
C–Fe/PANI	6 M KOH	1.0	1.65	33.0	370.7	M.N. Rantho et al., 2018 [17]
C–Fe/PANI/Ni-GF	1 M $NaNO_3$	1.0	1.7	68.0	718.2	This work

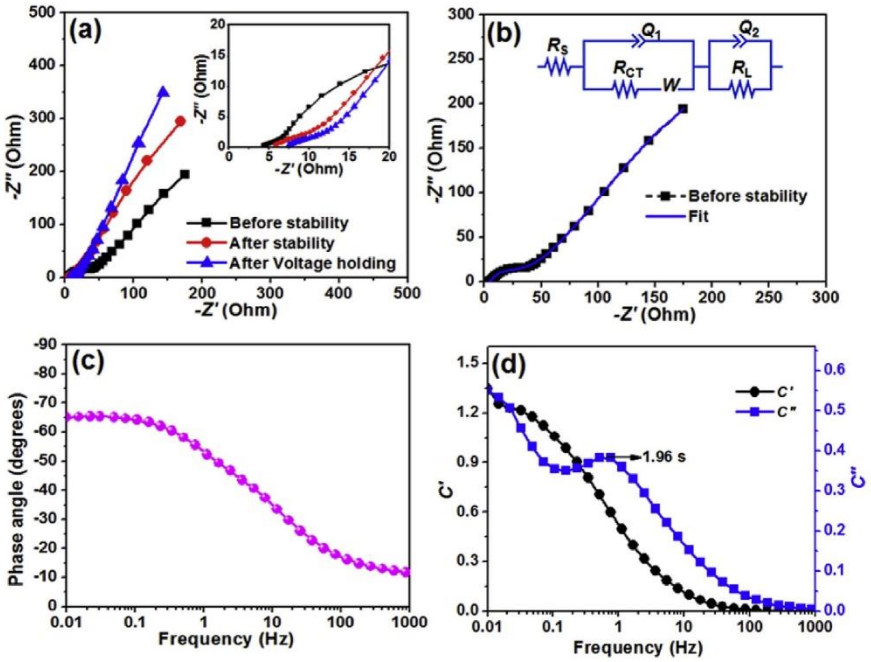

Fig. 8. (a) Nyquist plots before stability, after stability and after voltage holding (the inset shows the enlarged high-frequency region). (b) The Nyquist plot and the fit (blue solid-line) of the equivalent circuit diagram in the insert. (c) The Bode plot. (d) The frequency dependence of the $C'(\omega)$ and $C''(\omega)$ capacitances. (For interpretation of the references to color in this figure legend, the reader is referred to the Web version of this article.)

$$|Z(\omega)|^2 = Z'(\omega)^2 + Z''(\omega)^2 \tag{8}$$

and

$$\omega = 2\pi f$$

In Fig. 8(d), the $C'(\omega)$ which is the real accessible capacitance of the device that can be delivered corresponds to the deliverable capacitance of 1.35 F. The $C''(\omega)$ gives a relaxation time of 1.96 s which suggests that the device can be charged within few seconds.

Fig. 9(a) shows a self-discharge curve of the device after it was fully charged (i.e. up to 1.7 V) at the constant specific current of 5 A g^{-1} and subjected to open circuit voltage to observe the behavior of the device. The device within the first 30 min of the self-discharge curve drops and maintains a potential of 1.27 V, and after 76 h, the device still maintains the potential of 0.85 V. This good performance of the device (a slow self-discharge process) is attributed to the pseudocapacitive behavior (slow discharging process) and high cycling stability of the electrode material as shown for both cycling and voltage holding stability test. However, there is quick cell potential drop from 1.7 to 1.4 V within the 2 min and this could be due to the decomposition of the solvent [76]. Briefly, the solvent can be reduced on the negative electrode when the cell is fully charged. Thus, the reduction can continue even after the cut-off of current, which leads to the fast decrease in the negative electrode potential. The self-discharge curve can be explained further by applying two models [77]: Model 1 relates the current leakage to the resistance, R of the supercapacitor:

$$V = V_0 e^{\left(-\frac{t}{RC}\right)} \tag{9}$$

where the device parameters, V_0, C and t are the initial potential, the equivalent capacity and the self-discharge period, respectively. The fitting of the self-discharge curve with this model is shown in Fig. 9(b), which gives a linear trend. It is worth noting that the cell potential in Fig. 9(b) is plotted on the logarithm scale.

Model 2 which is basically based on a diffusion control process is shown in Fig. 9(c). In this model, the stored ionic charges are lost during the discharging of the device and the cell potential is expressed by:

$$V = V_0 - mt^{\frac{1}{2}} \tag{10}$$

where the device parameters, m, V_0 and t are the ions diffusion parameter, initial potential and self-discharge period, respectively.

Both model 1 and 2 show a better fit to the self-discharge curve. This suggests that the self-discharge process of the device is influenced by both current leakage and diffusion control process.

Furthermore, the practical application of C—Fe/PANI/Ni-GF symmetric device was demonstrated, as shown in Fig. 10. This was demonstrated by powering four a red light emitting diodes (LEDs) of 1.8 V and 30 mA each connected in parallel, as shown in Fig. 10(a). Two symmetric cells connected in series were charged to 1.7 V at a specific current of 2 A g^{-1}, thereafter, they were connected to LEDs. The change in the brightness of the LEDs is illustrated in Fig. 10(b).

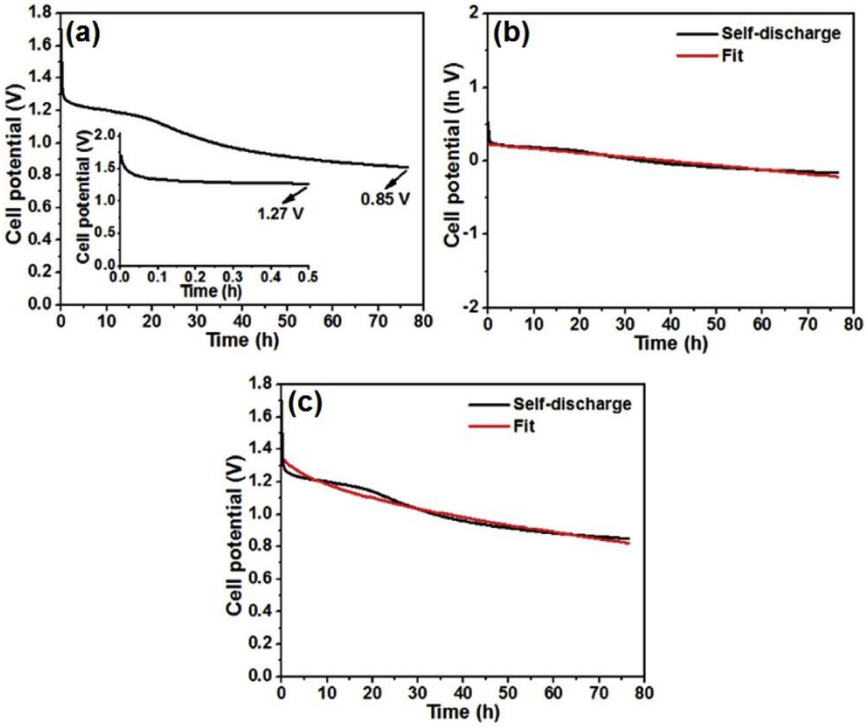

Fig. 9. (a) Self-discharge curve of the C–Fe/PANI/Ni-GF symmetric capacitor after the device was fully charged to 1.7 V at constant specific current of 5 A g^{-1} (the inset figure shows the self-discharge curve within the first 30 min of the evaluation).(b) and (c) are the fitted self-discharge curves with equations (9) and (10), respectively.

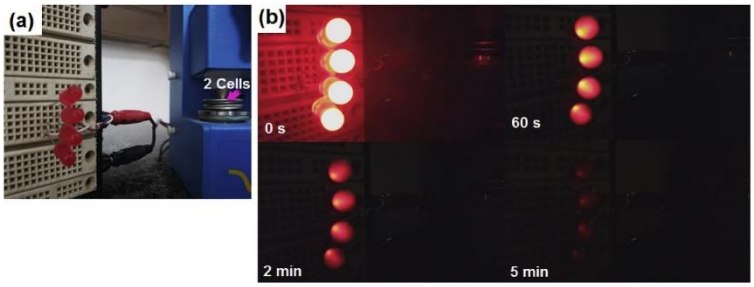

Fig. 10. (a) The setup of the two devices in series and four red LEDs in parallel; and (b) powered red LEDs at different stages after the devices were fully charged to 1.7 V. (For interpretation of the references to color in this figure legend, the reader is referred to the Web version of this article.)

The red LEDs at 0 s displayed high brightness which decreases after 60 s. These attractive results demonstrate a potential energy-storage of the device, it can be fully charged in a short time and discharge slow.

4. Conclusion

In this work, the nickel graphene foam (Ni-GF) was demonstrated to improve the electrochemical properties of the carbonized iron-polyaniline. We then successfully fabricated a symmetric supercapacitor device based on the carbonized iron-polyaniline/nickel graphene foam electrode using aqueous electrolyte. A fabricated symmetric device based on C–Fe/PANI/Ni-GF exhibited a maximum energy density of 68.0 W h kg^{-1} and power density of 718.2 W kg^{-1}, at a specific current of 1.0 A g^{-1} and cell potential window of 0.0–1.7 V. The device further displayed long-

term cycling stability with capacity retention of 91% over 10 000 galvanostatic charge-discharge cycles at 5 A g^{-1}. The stability of the device was also tested using the voltage holding and self-discharge approach whereby a slow-discharging process was observed which suggests a practical application of the device. The enhanced capacitive performance and the long-cycling stability of the device are due to the synergy effect of Fe-PANI and graphene foam, thus making this electrode material suitable for high-performance supercapacitor applications. The electrochemical performance of the carbonized iron-polyaniline/nickel graphene foam electrode can be improved by varying morphologies, synthesis methods and conditions [32]; and also by using ionic liquid electrolytes in the device to increase the potential window and hence the energy density.

Declaration of competing interest

Authors also declare that No conflict of interest of any form exists.

Acknowledgments

This work is based on research supported by the South African Research Chairs Initiative (SARChI) of the Department of Science and Technology and the National Research Foundation (NRF) of South Africa (Grant No. 61056). M. N. Rantho acknowledges the funding from University of Pretoria and NRF through SARChI in Carbon Technology and Materials.

Appendix A. Supplementary data

Supplementary data to this article can be found online at https://doi.org/10.1016/j.jallcom.2019.152993.

References

[1] G. Zhang, M. Kong, Y. Yao, L. Long, M. Yan, One-pot Synthesis of γ -MnS/Reduced Graphene Oxide with Enhanced Performance for Aqueous Asymmetric Supercapacitors, 065402 (n.d.). doi:10.1088/1361-6528/aa52a5.
[2] G. Feng, S. Li, V. Presser, P.T. Cummings, Molecular insights into carbon supercapacitors based on room-temperature ionic liquids, J. Phys. Chem. Lett. 4 (2013) 3367–3376, https://doi.org/10.1021/jz4014163.
[3] P. Simon, Y. Gogotsi, Materials for electrochemical capacitors, Nat. Mater. 7 (2008) 845–854.
[4] T.Y. Kim, H.W. Lee, M. Stoller, D.R. Dreyer, C.W. Bielawski, R.S. Ruoff, K.S. Suh, High-Performance Supercapacitors Based on Poly(ionic Liquid)-Modified Graphene Electrodes, 2010, https://doi.org/10.1021/NN101968P.
[5] W. Zuo, R. Li, C. Zhou, Y. Li, J. Xia, J. Liu, Battery-supercapacitor hybrid Devices : recent progress and future prospects, Adv. Sci. 4 (2017) 1–21, https://doi.org/10.1002/advs.201600539.
[6] F. Wang, X. Wu, X. Yuan, Z. Liu, Latest advances in supercapacitors: from new electrode materials to novel device designs, Chem. Soc. Rev. 46 (2017) 6816–6854, https://doi.org/10.1039/c7cs00205j.
[7] G. Wang, L. Zhang, J. Zhang, A review of electrode materials for electrochemical supercapacitors, Chem. Soc. Rev. 41 (2012) 797–828, https://doi.org/10.1039/C1CS15060J.
[8] K. Lota, V. Khomenko, E. Frackowiak, Capacitance properties of poly(3,4-ethylenedioxythiophene)/carbon nanotubes composites, J. Phys. Chem. Solids 65 (2004) 295–301, https://doi.org/10.1016/J.JPCS.2003.10.051.
[9] J.-Y. Kim, K.H. Kim, K.B. Kim, Fabrication and electrochemical properties of carbon nanotube/polypyrrole composite film electrodes with controlled pore size, J. Power Sources 176 (2008) 396–402, https://doi.org/10.1016/J.JPOWSOUR.2007.09.117.
[10] I. Shown, A. Ganguly, L.-C. Chen, K.-H. Chen, Conducting polymer-based flexible supercapacitor, Energy Sci. Eng. 3 (2015) 2–26, https://doi.org/10.1002/ese3.50.
[11] X. Wang, J. Deng, X. Duan, D. Liu, J. Guo, P. Liu, Crosslinked polyaniline nanorods with improved electrochemical performance as electrode material for supercapacitors, J. Mater. Chem. A 2 (2014) 12323, https://doi.org/10.1039/C4TA02231A.
[12] G. Giri, E. Verploegen, S.C.B. Mannsfeld, S. Atahan-Evrenk, D.H. Kim, S.Y. Lee, H.A. Becerril, A. Aspuru-Guzik, M.F. Toney, Z. Bao, Tuning charge transport in solution-sheared organic semiconductors using lattice strain, Nature 480 (2011) 504–508, https://doi.org/10.1038/nature10683.
[13] G. Sabouraud, S. Sadki, N. Brodie, Guillaume Sabouraud, The mechanisms of pyrrole electropolymerization, Chem. Soc. Rev. 29 (2000) 283–293, https://doi.org/10.1039/a807124a.
[14] D. Li, J. Huang, R.B. Kaner, Polyaniline nanofibers: a unique polymer nanostructure for versatile applications, Acc. Chem. Res. 42 (2009) 135–145, https://doi.org/10.1021/ar800080n.
[15] H. Mi, X. Zhang, X. Ye, S. Yang, Preparation and enhanced capacitance of core–shell polypyrrole/polyaniline composite electrode for supercapacitors, J. Power Sources 176 (2008) 403–409, https://doi.org/10.1016/j.jpowsour.2007.10.070.
[16] C. Portet, P.L. Taberna, P. Simon, E. Flahaut, C. Laberty-Robert, High power density electrodes for Carbon supercapacitor applications, Electrochim. Acta 50 (2005) 4174–4181, https://doi.org/10.1016/j.electacta.2005.01.038.
[17] M.N. Rantho, M.J. Madito, N. Manyala, Symmetric supercapacitor with supercapattery behavior based on carbonized iron cations adsorbed onto polyaniline, Electrochim. Acta 262 (2018), https://doi.org/10.1016/j.electacta.2018.01.001.
[18] B. Yanwu Zhu, S. Murali, W. Cai, X. Li, J. Won Suk, J.R. Potts, R.S. Ruoff, Y. Zhu, S. Murali, W. Cai, X. Li, J.W. Suk, J.R. Potts, R.S. Ruoff, Graphene and Graphene Oxide: Synthesis, Properties, and Applications, (n.d.). doi:10.1002/adma.201001068.
[19] Removal of Aqueous Hg(II) by Polyaniline: Sorption Characteristics and Mechanisms, (n.d.). doi:10.1021/es803710k.
[20] J. Zhang, C. Liu, G. Shi, Raman spectroscopic study on the structural changes of polyaniline during heating and cooling processes, J. Appl. Polym. Sci. 96 (2005) 732–739, https://doi.org/10.1002/app.21520.
[21] M. Sawangphruk, M. Suksomboon, K. Kongsupornsak, J. Khuntilo, P. Srimuk, Y. Sanguansak, P. Klunbud, P. Suktha, P. Chiochan, High-performance supercapacitors based on silver nanoparticle–polyaniline–graphene nanocomposites coated on flexible carbon fiber paper, J. Mater. Chem. A. 1 (2013) 9630, https://doi.org/10.1039/c3ta12194a.
[22] Q. Yao, L. Chen, W. Zhang, S. Liufu, X. Chen, Enhanced thermoelectric performance of single-walled carbon nanotubes/polyaniline hybrid nanocomposites, ACS Nano 4 (2010) 2445–2451, https://doi.org/10.1021/nn1002562.
[23] Q. Wang, Q. Yao, J. Chang, L. Chen, Enhanced thermoelectric properties of CNT/PANI composite nanofibers by highly orienting the arrangement of polymer chains, J. Mater. Chem. 22 (2012) 17612, https://doi.org/10.1039/c2jm32750c.
[24] H. Huang, J. Zhang, L. Jiang, Z. Zang, Preparation of cubic Cu2O nanoparticles wrapped by reduced graphene oxide for the efficient removal of rhodamine B, J. Alloy. Comp. 718 (2017) 112–115, https://doi.org/10.1016/j.jallcom.2017.05.132.
[25] X. Liu, T. Xu, Y. Li, Z. Zang, X. Peng, H. Wei, W. Zha, F. Wang, Enhanced X-ray photon response in solution-synthesized CsPbBr 3 nanoparticles wrapped by reduced graphene oxide, Sol. Energy Mater. Sol. Cells (2018), https://doi.org/10.1016/j.solmat.2018.08.009.
[26] C. Lee, X. Wei, J.W. Kysar, J. Hone, Of Monolayer Graphene, 2008.
[27] B.Z.JÆ.A. Zhamu, Processing of Nanographene Platelets (NGPs) and NGP Nanocomposites : a Review, 2008, pp. 5092–5101, https://doi.org/10.1007/s10853-008-2755-2.
[28] M.J. Madito, A. Bello, J.K. Dangbegnon, C.J. Oliphant, W.A. Jordaan, D.Y. Momodu, T.M. Masikhwa, F. Barzegar, M. Fabiane, N. Manyala, Atmospheric Pressure Chemical Vapour Deposition A Dilute Cu (Ni) Alloy for Synthesis of Large-Area Bernal Stacked Bilayer Graphene Using Atmospheric Pressure Chemical Vapour Deposition, 2016, https://doi.org/10.1063/1.4939648, 015306.
[29] K.S. Novoselov, A.K. Geim, S.V. Morozov, D. Jiang, Y. Zhang, S.V. Dubonos, I.V. Grigorieva, A.A. Firsov, Electric field effect in atomically thin carbon films, Science 666 (2004) 666–669, https://doi.org/10.1126/science.1102896.
[30] M. Yu, Y. Huang, C. Li, Y. Zeng, W. Wang, Y. Li, P. Fang, X. Lu, Y. Tong, Building three-dimensional graphene frameworks for energy storage and catalysis, Adv. Funct. Mater. 25 (2015) 324–330, https://doi.org/10.1002/adfm.201402964.
[31] H. Wang, Q. Hao, X. Yang, L. Lu, X. Wang, A nanostructured graphene/polyaniline hybrid material for supercapacitors, Nanoscale 2 (2010) 2164, https://doi.org/10.1039/c0nr00224k.
[32] Z. Huang, L. Li, Y. Wang, C. Zhang, T. Liu, Polyaniline/graphene nanocomposites towards high-performance supercapacitors: a review, Compos. Commun. 8 (2018) 83–91, https://doi.org/10.1016/J.COCO.2017.11.005.
[33] C. Mattevi, H. Kim, M. Chhowalla, A review of chemical vapour deposition of graphene on copper, J. Mater. Chem. 21 (2011) 3324.
[34] Y. Zhang, T. Tang, C. Girit, Z. Hao, M.C. Martin, A. Zettl, M.F. Crommie, Y.R. Shen, F. Wang, Direct observation of a widely tunable bandgap in bilayer graphene, Nature 459 (2009) 820–823.
[35] W. Fang, A.L. Hsu, R. Caudillo, Y. Song, A.G. Birdwell, E. Zakar, M. Kalbac, M. Dubey, T. Palacios, M.S. Dresselhaus, P.T. Araujo, J. Kong, Rapid identification of stacking orientation in isotopically labeled chemical-vapor grown bilayer graphene by Raman spectroscopy, Nano Lett. 13 (2013) 1541–1548.
[36] M.J. Madito, A. Bello, J.K. Dangbegnon, C.J. Oliphant, W.A. Jordaan, T.M. Masikhwa, D.Y. Momodu, N. Manyala, Raman analysis of bilayer graphene film prepared on commercial Cu(0.5 at% Ni) foil, J. Raman Spectrosc. (2015), https://doi.org/10.1002/jrs.4848.
[37] C. Avril, V. Malavergne, R. Caracas, B. Zanda, B. Reynard, E. Charon, E. Bobocioiu, F. Brunet, S. Borensztajn, S. Pont, M. Tarrida, F. Guyot, Raman spectroscopic properties and Raman identification of CaS-MgS-MnS-FeS-Cr $_2$

FeS $_4$ sulfides in meteorites and reduced sulfur-rich systems, Meteorit. Planet. Sci. 48 (2013) 1415–1426, https://doi.org/10.1111/maps.12145.
[38] G. Genchev, A. Erbe, Raman spectroscopy of mackinawite FeS in anodic iron sulfide corrosion products, J. Electrochem. Soc. 163 (2016) C333–C338, https://doi.org/10.1149/2.1151606jes.
[39] J.-A. Bourdoiseau, M. Jeannin, R. Sabot, C. Rémazeilles, P. Refait, Characterisation of mackinawite by Raman spectroscopy: effects of crystallisation, drying and oxidation, Corros. Sci. 50 (2008) 3247–3255, https://doi.org/10.1016/J.CORSCI.2008.08.041.
[40] X. Yang, C. Li, J. Huang, Y. Liu, W. Chen, J. Shen, Y. Zhu, C. Li, Nitrogen-doped Fe $_3$ C@C particles as an efficient heterogeneous photo-assisted Fenton catalyst, RSC Adv. 7 (2017) 15168–15175, https://doi.org/10.1039/C7RA00486A.
[41] P. Colomban, S. Cherifi, G. Despert, Raman identification of corrosion products on automotive galvanized steel sheets, J. Raman Spectrosc. 39 (2008) 881–886, https://doi.org/10.1002/jrs.1927.
[42] M.K. Nieuwoudt, J.D. Comins, I. Cukrowski, The growth of the passive film on iron in 0.05 M NaOH studied in situ by Raman micro-spectroscopy and electrochemical polarisation. Part I: near-resonance enhancement of the Raman spectra of iron oxide and oxyhydroxide compounds, J. Raman Spectrosc. 42 (2011) 1335–1339, https://doi.org/10.1002/jrs.2837.
[43] X. Feng, Z. Yan, N. Chen, Y. Zhang, X. Liu, Y. Ma, X. Yang, W. Hou, Synthesis of a graphene/polyaniline/MCM-41 nanocomposite and its application as a supercapacitor, New J. Chem. 37 (2013) 2203, https://doi.org/10.1039/c3nj00108c.
[44] S.K. Lai, C.M. Luk, L. Tang, K.S. Teng, S.P. Lau, Photoresponse of polyaniline-functionalized graphene quantum dots, Nanoscale 7 (2015) 5338–5343, https://doi.org/10.1039/C4NR07565J.
[45] H. Aoki, M.S. Dresselhaus (Eds.), Physics of Graphene, Springer, New York, 2014.
[46] M. Hsiao, S. Liao, M. Yen, C. Teng, S. Lee, N. Pu, C. Wang, Y. Sung, M. Ger, C. Ma, M. Hsiao, Preparation and properties of a graphene reinforced nanocomposite conducting plate, J. Mater. Chem. 20 (2010) 8496.
[47] S. Ogawa, T. Yamada, S. Ishidzuka, A. Yoshigoe, M. Hasegawa, Y. Teraoka, Y. Takakuwa, Graphene growth and carbon diffusion process during vacuum heating on Cu (111)/Al 2 O 3 substrates, Jpn. J. Appl. Phys. 52 (2013) 110122.
[48] G.H. Le, A.Q. Ha, Q.K. Nguyen, K.T. Nguyen, P.T. Dang, H.T.K. Tran, L.D. Vu, T. V Nguyen, G.D. Lee, T.A. Vu, Removal of Cd $^{2+}$ and Cu $^{2+}$ ions from aqueous solution by using Fe–Fe $_3$ O $_4$/graphene oxide as a novel and efficient adsorbent, Mater. Res. Express 3 (2016) 105603, https://doi.org/10.1088/2053-1591/3/10/105603.
[49] G. Wu, C.M. Johnston, N.H. Mack, K. Artyushkova, M. Ferrandon, M. Nelson, J.S. Lezama-Pacheco, S.D. Conradson, K.L. More, D.J. Myers, P. Zelenay, Synthesis–structure–performance correlation for polyaniline–Me–C non-precious metal cathode catalysts for oxygen reduction in fuel cells, J. Mater. Chem. 21 (2011) 11392, https://doi.org/10.1039/c0jm03613g.
[50] M.V. Morales-Gallardo, A.M. Ayala, M. Pal, M.A. Cortes Jacome, J.A. Toledo Antonio, N.R. Mathews, Synthesis of pyrite FeS2 nanorods by simple hydrothermal method and its photocatalytic activity, Chem. Phys. Lett. 660 (2016) 93–98, https://doi.org/10.1016/J.CPLETT.2016.07.046.
[51] A.G. Volkov, S. Paula, D.W. Deamer, Two mechanisms of permeation of small neutral molecules and hydrated ions across phospholipid bilayers, Bioelectrochem. Bioenerg. 42 (1997) 153–160, https://doi.org/10.1016/S0302-4598(96)05097-0.
[52] Sept, Phenomenological theory of ion solvation (accessed March 8, 2018), https://pubs.acs.org/doi/pdf/10.1021/j150579a011, 1959.
[53] B. Akinwolemiwa, C. Peng, G.Z. Chen, Redox electrolytes in supercapacitors, J. Electrochem. Soc. 162 (2015) A5054–A5059, https://doi.org/10.1149/2.0111505jes.
[54] A. Laheäär, P. Przygocki, Q. Abbas, F. Béguin, Appropriate Methods for Evaluating the Efficiency and Capacitive Behavior of Different Types of Supercapacitors, 2015, https://doi.org/10.1016/j.elecom.2015.07.022.
[55] K.O. Oyedotun, M.J. Madito, A. Bello, D.Y. Momodu, A.A. Mirghni, N. Manyala, Investigation of graphene oxide nanogel and carbon nanorods as electrode for electrochemical supercapacitor, Electrochim. Acta (2017), https://doi.org/10.1016/j.electacta.2017.05.150.
[56] G. Godillot, L. Guerlou-Demourgues, P.-L. Taberna, P. Simon, C. Delmas, Original conductive nano-Co3O4 investigated as electrode material for hybrid supercapacitors, Electrochem. Solid State Lett. 14 (2011) A139, https://doi.org/10.1149/1.3609259.
[57] D.Y. Momodu, F. Barzegar, A. Bello, J. Dangbegnon, T. Masikhwa, J. Madito, N. Manyala, Simonkolleite-graphene foam composites and their superior electrochemical performance, Electrochim. Acta 151 (2015) 591–598, https://doi.org/10.1016/j.electacta.2014.11.015.
[58] H. Peng, Z. Mo, S. Liao, H. Liang, L. Yang, F. Luo, H. Song, Y. Zhong, B. Zhang, High performance Fe- and N- doped carbon catalyst with graphene structure for oxygen reduction, Sci. Rep. 3 (2013) 1765, https://doi.org/10.1038/srep01765.
[59] N. Daems, X. Sheng, Y. Alvarez-Gallego, I.F.J. Vankelecom, P.P. Pescarmona, Iron-containing N-doped carbon electrocatalysts for the cogeneration of hydroxylamine and electricity in a H $_2$ –NO fuel cell, Green Chem. 18 (2016) 1547–1559, https://doi.org/10.1039/C5GC02197A.
[60] X. Rui, H. Tan, Q. Yan, Nanostructured metal sulfides for energy storage, Nanoscale 6 (2014) 9889, https://doi.org/10.1039/C4NR03057E.
[61] M. Dirican, M. Yanilmaz, X. Zhang, Free-standing polyaniline–porous carbon nanofiber electrodes for symmetric and asymmetric supercapacitors, RSC Adv. 4 (2014) 59427–59435, https://doi.org/10.1039/C4RA09103E.
[62] H. MI, X. ZHANG, S. AN, X. YE, S. YANG, Microwave-assisted synthesis and electrochemical capacitance of polyaniline/multi-wall carbon nanotubes composite, Electrochem, Commun 9 (2007) 2859–2862, https://doi.org/10.1016/j.elecom.2007.10.013.
[63] S.K. Simotwo, C. Delre, V. Kalra, Supercapacitor electrodes based on high-purity electrospun polyaniline and polyaniline-carbon nanotube nanofibers, ACS Appl. Mater. Interfaces 8 (2016) 21261–21269, https://doi.org/10.1021/acsami.6b03463.
[64] M. Wu, G.A. Snook, V. Gupta, M. Shaffer, D.J. Fray, G.Z. Chen, Electrochemical fabrication and capacitance of composite films of carbon nanotubes and polyaniline, J. Mater. Chem. 15 (2005) 2297, https://doi.org/10.1039/b418835g.
[65] M.J. Bleda-Martínez, C. Peng, S. Zhang, G.Z. Chen, E. Morallón, D. Cazorla-Amorós, Electrochemical methods to enhance the capacitance in activated carbon/polyaniline composites, J. Electrochem. Soc. 155 (2008) A672, https://doi.org/10.1149/1.2956969.
[66] D. Salinas-Torres, J.M. Sieben, D. Lozano-Castelló, D. Cazorla-Amorós, E. Morallón, Asymmetric hybrid capacitors based on activated carbon and activated carbon fibre-PANI electrodes, Electrochim. Acta 89 (2013) 326–333, https://doi.org/10.1016/j.electacta.2012.11.039.
[67] K.S. Ryu, Y.-G. Lee, K.M. Kim, Y.J. Park, Y.-S. Hong, X. Wu, M.G. Kang, N.-G. Park, R.Y. Song, J.M. Ko, Electrochemical capacitor with chemically polymerized conducting polymer based on activated carbon as hybrid electrodes, Synth. Met. 153 (2005) 89–92, https://doi.org/10.1016/j.synthmet.2005.07.167.
[68] F. Chen, P. Liu, Q. Zhao, Well-defined graphene/polyaniline flake composites for high performance supercapacitors, Electrochim. Acta 76 (2012) 62–68, https://doi.org/10.1016/j.electacta.2012.04.154.
[69] G.A. Snook, P. Kao, A.S. Best, Conducting-polymer-based supercapacitor devices and electrodes, J. Power Sources 196 (2010) 1–12, https://doi.org/10.1016/j.jpowsour.2010.06.084.
[70] S. Bose, T. Kuila, A.K. Mishra, R. Rajasekar, N.H. Kim, J.H. Lee, Carbon-based nanostructured materials and their composites as supercapacitor electrodes, J. Mater. Chem. 22 (2012) 767–784, https://doi.org/10.1039/c1jm14468e.
[71] Y. Zhou, H. Xu, N. Lachman, M. Ghaffari, S. Wu, Y. Liu, A. Ugur, K.K. Gleason, B.L. Wardle, Q.M. Zhang, Advanced asymmetric supercapacitor based on conducting polymer and aligned carbon nanotubes with controlled nanomorphology, Nano Energy 9 (2014) 176–185.
[72] W. Sun, X. Chen, Preparation and Characterization of Polypyrrole Films for Three-Dimensional Micro Supercapacitor, vol. 193, 2009, pp. 924–929, https://doi.org/10.1016/j.jpowsour.2009.04.063.
[73] H. Li, J. Wang, Q. Chu, Z. Wang, F. Zhang, S. Wang, Theoretical and Experimental Specific Capacitance of Polyaniline in Sulfuric Acid, vol. 190, 2009, pp. 578–586, https://doi.org/10.1016/j.jpowsour.2009.01.052.
[74] T.M. Masikhwa, F. Barzegar, J.K. Dangbegnon, A. Bello, M.J. Madito, D. Momodu, N. Manyala, Asymmetric supercapacitor based on VS $_2$ nanosheets and activated carbon materials, RSC Adv. (2016), https://doi.org/10.1039/C5RA27155J.
[75] P.L. Taberna, P. Simon, J.-F.F. Fauvarque, Electrochemical characteristics and impedance spectroscopy studies of carbon-carbon supercapacitors, J. Electrochem. Soc. 150 (2003) A292–A300, https://doi.org/10.1149/1.1543948.
[76] L. Chen, H. Bai, Z. Huang, L. Li, Mechanism investigation and suppression of self-discharge in active electrolyte enhanced supercapacitors, Energy Environ. Sci. 7 (2014) 1750–1759, https://doi.org/10.1039/C4EE00002A.
[77] F. Barzegar, A.A. Khaleed, F.U. Ugbo, K.O. Oyeniran, D.Y. Momodu, A. Bello, J.K. Dangbegnon, N. Manyala, F. Barzegar, A.A. Khaleed, F.U. Ugbo, K.O. Oyeniran, Cycling and Floating Performance of Symmetric Supercapacitor Derived from Coconut Shell Biomass Cycling and Floating Performance of Symmetric Supercapacitor Derived from Coconut Shell Biomass, 2016, https://doi.org/10.1063/1.4967348, 115306.

4.2.3 Concluding remarks

The carbonized iron-polyaniline/nickel graphene foam (C-Fe/PANI/Ni-GF) electrode was successfully synthesized by pasting a mixture of iron-polyaniline (Fe/PANI) on nickel graphene foam (Ni-GF) and carbonized under the nitrogen. The electrode was tested both in three and two-electrode (i.e. symmetric) cell configurations using 1 M $NaNO_3$ electrolyte for electrochemical characterization. The as-fabricated symmetric device exhibited a maximum specific energy of 68.0 W h kg^{-1} and specific power of 718.2 W kg^{-1}, at a specific current of 1.0 A g^{-1} and the maximum potential of 1.7 V. The device further displayed long-term cycling stability with capacity retention of 91% over 10 000 galvanostatic charge-discharge cycles at 5 A g^{-1}.

4.3 Hybrid electrochemical supercapacitor based on birnessite-type MnO_2/carbon composite as the positive electrode and carbonized iron-polyaniline/nickel graphene foam as a negative electrode

4.3.1 Summary

The results for the synthesis of MnO_2-C with hierarchical nanostructures synthesized using $KMnO_4$ solution and spent printing carbon grains as described in chapter 4, confirms a successful synthesis of a MnO_2-C composite. Similarly, the results for the synthesis of C-Fe/PANI/Ni-GF electrode confirms a successful synthesis of C-Fe/PANI/Ni-GF as described in chapter 3, confirms a successful synthesis of the electrode which is expected to have strong metal-polymer/graphene interactions. The results for the MnO_2-C//C-Fe/PANI/Ni-GF asymmetric device, fabricated as described in chapter 3, shows the excellent electrochemical performance of the device.

The results are discussed in the attached published paper below in *AIP Advances*.

4.3.2 Publication

AIP Advances

Hybrid electrochemical supercapacitor based on birnessite-type MnO_2/carbon composite as the positive electrode and carbonized iron-polyaniline/nickel graphene foam as a negative electrode

Cite as: AIP Advances **10**, 065113 (2020); https://doi.org/10.1063/5.0011862
Submitted: 27 April 2020 . Accepted: 21 May 2020 . Published Online: 08 June 2020

M. N. Rantho, M. J. Madito, K. O. Oyedotun, D. J. Tarimo, and N. Manyala

Hybrid electrochemical supercapacitor based on birnessite-type MnO_2/carbon composite as the positive electrode and carbonized iron-polyaniline/nickel graphene foam as a negative electrode

Cite as: AIP Advances 10, 065113 (2020); doi: 10.1063/5.0011862
Submitted: 27 April 2020 • Accepted: 21 May 2020 •
Published Online: 8 June 2020

M. N. Rantho, M. J. Madito, K. O. Oyedotun, D. J. Tarimo, and N. Manyala[a]

AFFILIATIONS

Department of Physics, Institute of Applied Materials, SARChI Chair in Carbon Technology and Materials, University of Pretoria, Pretoria 0028, South Africa

[a]**Author to whom correspondence should be addressed:** ncholu.manyala@up.ac.za. **Tel.:** + (27)12 420 3549. **Fax:** + (27)12 420 2516

ABSTRACT

In this work, a birnessite-type MnO_2/carbon composite with hierarchical nanostructures was synthesized using $KMnO_4$ solution and spent printing carbon grains. A hybrid electrochemical supercapacitor device was fabricated based on the birnessite-type MnO_2–carbon composite electrode and carbonized iron-polyaniline/nickel graphene foam as positive and negative electrodes, respectively. At the lowest specific current of 1.0 A g^{-1} and cell potential of 2.2 V in 2.5M KNO_3 electrolyte, the device displayed a high energy and power density of 34.6 W h kg^{-1} and 1100.0 W kg^{-1}, respectively. The device further displayed long-term cycling stability with a capacitance retention of 98% over 10 000 galvanostatic charge–discharge cycles at 10 A g^{-1}. This device displays the overall excellent electrochemical performance.

I. INTRODUCTION

Today, there is a great development of power systems due to the increased demand for highly reliable electricity and the consumption of renewable energy technologies. Power supply is a critical issue due to the rapid increase in electronic loads. Energy storage systems with vital power utility are in high demand. Among different types of energy storage systems, supercapacitors (SCs) have received great attention owing to their attractive properties, such as long life cycle stability, high power density, high efficiency, fast charge–discharge capability, and operational safety.[1–7] In general, SCs exhibit low energy densities, and this was the motivation for this study. To overcome low energy densities of SCs, one of the approaches is to develop new electrode materials for SCs (e.g., carbon materials, metal oxides/hydroxides/disulfides, and conducting polymers). The focus has also been on developing hybrid supercapacitors using battery-like electrode materials and pseudocapacitive electrodes since they display high capacity/capacitance.[8,9]

Conducting polymers for electrochemical energy storage applications have been studied extensively due to their high potential window, high conductivity, high storage capacity, and low cost.[10–13] The conducting polymers commonly used in SCs are polyaniline (PANI), polypyrrole (PPY), and polythiophene (PT).[14] The composites of these conducting polymers have shown enhanced electrochemical performance in SCs. Recent reports have shown that iron–polyaniline (Fe–PANI) composites attain high electrocatalytic and electrochemical performance with long-cycling stability.[7,15–17] Moreover, the PANI/graphene composite shows much better capacitance performance, and the synergy effect

between the two materials greatly improves the retention life of the composite material.[7,18,19] Among several metal oxides, birnessite-type manganese dioxide (MnO_2) has been studied extensively for SC application because it is low cost, naturally abundant, highly redox-active, and environmentally friendly, and it exhibits high pseudocapacitive performance in aqueous neutral electrolytes.[20–23] Despite the high electrochemical performance displayed by MnO_2 in aqueous neutral electrolytes, it has low electrical conductivity resulting in low cycling stability.[21,24] The low cycling stability of MnO_2 is improved by using carbon-based materials with excellent conductivity as a support during MnO_2 synthesis.[25–30]

Although studies about birnessite-type MnO_2-based materials as the positive electrode and activated carbon (AC) as the negative electrode have been extensively reported in the literature,[20–22,25,29–44] there are rare studies done on carbonized iron–polyaniline/nickel graphene foam (CFe/PANI/NiGF) as a negative electrode. In this work, we report on a hybrid electrochemical supercapacitor device based on the birnessite-type MnO_2C composite as the positive electrode and carbonized iron–polyaniline/nickel graphene foam as a negative electrode. The as-fabricated asymmetric device was performed at a cell potential of 0–2.2 V in 2.5M KNO_3. At a specific current of 1 A g^{-1}, this device displayed energy and power densities of 34.6 W h kg^{-1} and 1100.0 W kg^{-1}, respectively. Additionally, for both cycling and voltage holding tests, the device exhibited excellent stability.

II. EXPERIMENTAL

A. Synthesis of the as-prepared electrodes

MnO_2C with hierarchical nanostructures was synthesized using $KMnO_4$ solution and spent printing carbon grains [Scheme 1(a)]. In the synthesis, 0.6 g of spent printing carbon grains were dissolved in 32 ml of 2M $KMnO_4$ solution.[47] The mixture was then transferred into a sealed 50 ml Teflon-lined autoclave and kept at 160 °C for 18 h. The recovered product [MnO_2C composite with nanowires/microsponges morphology, Scheme 1(a)] was collected as a brown precipitant by several centrifugation and ethanol washing cycles. Briefly, the hydrothermal solid–liquid reaction is proposed as

$$4MnO_4^- + 3C \rightarrow 4MnO_2 + 2CO_3^{2-} + CO_2. \quad (1)$$

Fei *et al.*[47] referred to this hydrothermal method as a one-pot environmentally friendly process that changes toxic carbon grains from a spent inkjet cartridge into transition metal oxide hierarchical nanostructures through a limited hydrothermal redox reaction. Therefore, this does not only avoid the disposal of toxic carbon grains but also provides metal oxide nanostructures for energy storage applications.

The CFe/PANI/NiGF used as the negative electrode was prepared via a similar method to that reported in our previous work[7] [Scheme 1(b)]. Briefly, 0.4 g of PANI and 0.2 g of iron nitrate

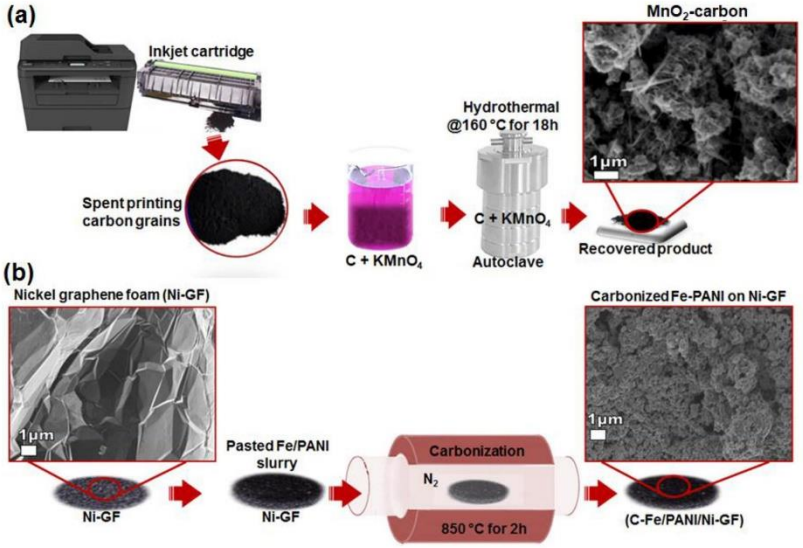

SCHEME 1. (a) The synthesis route for the MnO_2C composite using $KMnO_4$ solution and spent printing carbon grains. (b) The synthesis route for the carbonized Fe–PANI mixture on NiGF (CFe/PANI/NiGF).

nonahydrate [$Fe(NO_3)_3{\cdot}9H_2O$] were dissolved in 50 ml of ethanol and dispersed until the Fe–PANI slurry was formed. The slurry was pasted on graphene supported by nickel foam and carbonized at 850 °C (ramp rate of 10 °C min^{-1}) for 2 h under nitrogen gas. The difference between annealed NiGF (uncoated) and annealed material-coated NiGF gives the active material's substance load of the CFe/PANI/NiGF electrode.

B. Morphological, structural, compositional, and electrochemical characterization

The characterization of the as-prepared electrode materials was carried out using scanning electron microscopy (SEM, Zeiss Ultra Plus 55 field emission scanning electron microscope), energy-dispersive x-ray spectrometer (EDS), x-ray diffractometer (XRD), XPERTPRO diffractometer (PANalytical BV, Netherlands), Raman spectroscopy (WITec alpha300 RAS+ confocal Raman microscope with a 532 nm excitation laser and a laser power of 5 mW), and x-ray photoelectron spectroscopy (XPS) (Thermo Fisher photoelectron spectrometer fitted with a monochromatic Al Kα radiation x-ray source).

In the case of electrochemical characterization, a multi-channel Biologic VMP-300 potentiostat (Knoxville TN 37930, USA) was used in three- and two-electrode configurations. For three-electrode configuration, the MnO_2C composite electrode was obtained by coating a mixture of 80 wt. % MnO_2 (active material), 10 wt. % carbon black as a conductive additive, and 10 wt. % polyvinylidene fluoride (PVDF) binder dispersed in N-methylpyrrolidone (NMP) solution onto a nickel foam (1 × 1 cm^2). Thereafter, the electrode was dried at 60 °C overnight. The masses of the active materials of the MnO_2C composite and CFe/PANI/NiGF were 3.8 mg/cm^2 and 1.9 mg/cm^2, respectively. The CFe/PANI/NiGF working electrode was prepared as discussed in Scheme 1(b). The measurements were carried out in 2.5M KNO_3 electrolyte using a glassy carbon plate as the counter electrode, Ag/AgCl (saturated with 3M KCl) reference electrode, and MnO_2C composite and CFe/PANI/NiGF served as positive and negative working electrodes, respectively. For two-electrode configuration, masses of positive and negative working electrodes were 1.7 mg/cm^2 and 2.5 mg/cm^2, respectively. The asymmetric device was fabricated using 2.5M KNO_3 aqueous electrolyte. The specific capacitance (C_S) was calculated for both three-electrode and two-electrode configurations using Eq. (1),[7,48–50]

$$C_s = \frac{I\Delta t}{m\Delta V}, \tag{2}$$

where I/m is the specific current (A/g), m is the mass of the electrode material (g), Δt is the discharge time (s), and ΔV is the maximum potential. The mass balance between the two electrodes is expressed as[51]

$$\frac{m_+}{m_-} = \frac{C_{s(-)} \times \Delta V_-}{C_{s(+)} \times \Delta V_+}, \tag{3}$$

where $C_{S(+)}$, $C_{S(-)}$, m_+, m_-, ΔV_+, and ΔV_- are the specific capacitances, masses, and maximum potential windows of the active materials in positive and negative electrodes, respectively. The energy density E_d and the power density P_d of the device were calculated using the following equations:

$$E_d\left(\text{W h kg}^{-1}\right) = \frac{C_s\Delta V^2}{7.2}, \tag{4}$$

$$P_d\left(\text{W kg}^{-1}\right) = \frac{3600E_d}{\Delta t}, \tag{5}$$

where C_S is the specific capacitance, ΔV is the maximum cell potential, and Δt is the discharge time (s).

III. RESULTS AND DISCUSSION

A. Morphological, structural, and compositional characterization

The morphologies of the as-prepared materials were examined using SEM, as shown in Fig. 1. Figures 1(a) and 1(b) display the morphology of the MnO_2C composite at low and high magnifications, respectively. In these figures, the MnO_2C composite shows a combined morphology of nanowires and microsponges (sponge-like hierarchical nanostructures). Fei *et al.* have observed a similar morphology for MnO_2 prepared using the same synthesis method and conditions.[47] Figure 1(c) shows the morphology of NiGF, which shows graphene wrinkles and ripples on the Ni template.[52] The carbonized iron–polyaniline on nickel graphene foam (CFe/PANI/NiGF) shows a different morphology from NiGF, i.e., agglomerated nanograins [Figs. 1(d) and 1(e)].

The elemental composition of the as-prepared materials, MnO_2C composite, and CFe/PANI/NiGF was obtained using EDS, and the results are shown in Fig. 2. Figure 2(a) shows the average EDS spectrum of the MnO_2C composite, which displays the main elements Mn, O, and K, and a significant amount of C. In Fig. 2(a), the presence of K is from the synthesis, i.e., $KMnO_4$ solution. Figure 2(b) displays the average EDS spectrum of CFe/PANI/NiGF, which shows the main elements Fe, S, O, N, C, and Ni. The detected Ni is from the Ni template from which graphene was grown, and S is attributed to the PANI precursor (ammonium persulfate), which degraded during pyrolysis.[17]

Figure 3(a) shows the XRD pattern of the as-prepared MnO_2C composite, which displays the characteristic diffraction peaks of the birnessite-type MnO_2C composite with peaks corresponding to (121) and (002) planes. The matching Inorganic Crystal Structure Database (ICSD) Card No. 20227 was used to index the diffraction peaks. The diffraction peak at around 26° is associated with the (002) plane of graphitic carbon. Figure 3(b) shows the XRD pattern of the as-prepared carbonized iron–PANI (CFe/PANI) without NiGF, which matches the diffraction peak positions of the orthorhombic Fe_3C (ICSD No. 16593) and FeS (ICSD No. 35008). In addition, the diffraction peaks matching Fe (ICSD No. 64795) are also observed, which suggest that during the pyrolysis process, the Fe cations were reduced to metallic Fe.[53]

Furthermore, the Raman spectrum of the as-prepared MnO_2C composite [Fig. 3(c)] shows a broad peak at 640 cm^{-1} with a shoulder at 495 cm^{-1} and 570 cm^{-1}, which agree with the main vibrational features of the birnessite-type MnO_2.[54] The presence of carbon traces in the as-prepared MnO_2C composite is shown by the D (~1346 cm) and G (1587 cm^{-1}) peaks, which are characteristic of the disordered carbon and the tangential vibrations of the

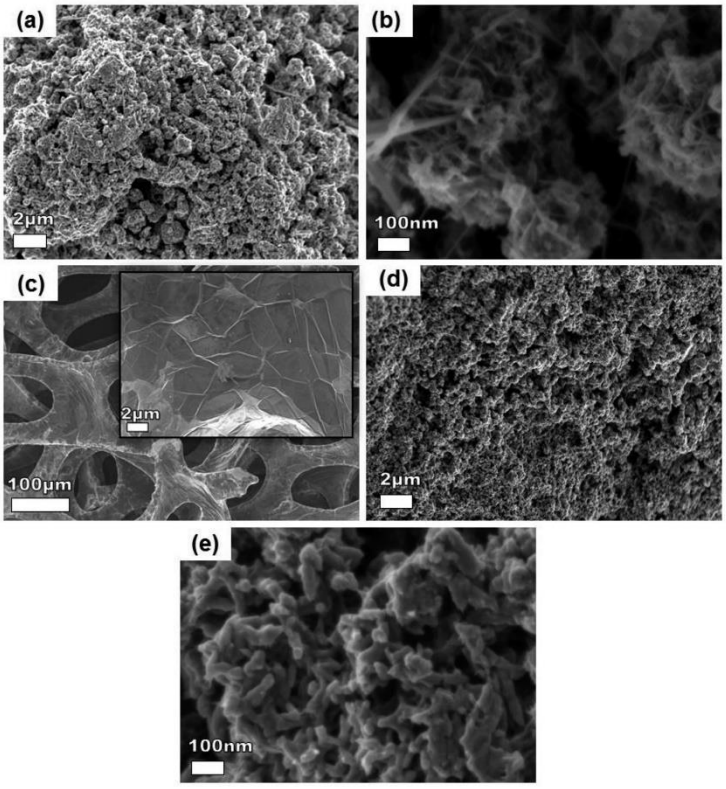

FIG. 1. SEM images: [(a) and (b)] low and high magnification images of the MnO_2C composite, respectively. (c) Low and high magnification images of NiGF (inset of the figure). [(d) and (e)] Low and high magnification images of CFe/PANI/NiGF, respectively.

sp^2-hybridized carbon, respectively.[55] Figure 3(d) shows the Raman spectrum of the as-prepared CFe/PANI/NiGF. From this figure, the D and G bands in the range of 1240–1700 cm^{-1} are observed, and these are attributed to the functional groups of PANI (i.e., CN at ~1210 cm^{-1} and 1346 cm^{-1}, CC at 1412 cm^{-1}, C=N at 1490 cm^{-1}, C=C at 1585 cm^{-1} and CC at 1610 cm^{-1}).[56,57] Additionally, the observed Fe–PANI vibration bands in the range of 100–700 cm^{-1} [Fig. 3(e)] are attributed to orthorhombic sulfur α-S_8 (153 cm^{-1}, 223 cm^{-1}, and 471 cm^{-1}),[58,59] FeS (191 cm^{-1}, 205 cm^{-1}, 265 cm^{-1}, and 290 cm^{-1}),[59,60] α-FeOOH (310 cm^{-1}), γ-FeOOH (360 cm^{-1} and 540 cm^{-1}),[59,61] Fe_3C (223 cm^{-1}, 290 cm^{-1}, 360 cm^{-1}, and 603 cm^{-1}),[62] and γ-Fe_2O_3/Fe_3O_4 (680 cm^{-1}).[61,63] It is worth noting that the phases observed in the Fe–PANI range [Fig. 3(e)] have x-ray diffraction peaks (α-S_8 ICSD No. 27261, α-FeOOH ICSD No. 77327, γ-FeOOH ICSD No. 93948, Fe_2O_3 ICSD No. 64599, and Fe_3O_4 ICSD No. 35000), which overlap with the diffraction peaks of the phases shown in the XRD pattern of the CFe/PANI/NiGF [Fig. 3(b)].[7] In Fig. 3(d), the characteristic Raman signature of graphene foam is not observed, and this is because the graphene is coated by Fe/PANI, as can be seen from the SEM images. Nonetheless, the interaction between the Fe/PANI and graphene foam during pyrolysis is energetically favorable owing to the unpaired π-electron in graphene and the high electronegativity of oxygen and sulfur present in the material.[7] Figure 3(f) shows the characteristic Raman spectra of as-prepared NiGF, which displays the main features of the Raman spectrum of graphene. These spectra are a characteristic Raman spectrum of a monolayer (top), bilayer (middle), and few-layer (bottom) graphene with 2D-to-G peak intensity ratios of >2, ~1, and <0.6, respectively.[7,64] Figure 3(f) reveals the layers of NiGF as discussed in our recent work.[7]

Figure 4(a) shows the core level spectra of C 1s, K 2p, Mn 2p, and O 1s obtained from the as-prepared MnO_2C composite. The core level spectrum of C 1s of the MnO_2C composite material shows a peak at 284.6 eV attributed to the C=C and C—C bonds,

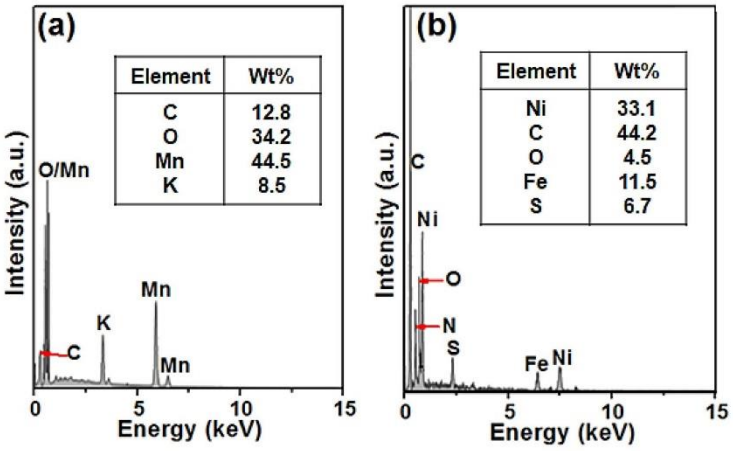

FIG. 2. Average EDS spectra: (a) MnO_2C composite and (b) CFe/PANI/NiGF.

and the broadness of the peak is due to the carbon-oxide components present in the sample. The core level spectrum of K 2p confirms the presence of potassium oxide in the material, which arises from $KMnO_4$ used in the synthesis of the MnO_2C composite. The core level spectrum of Mn 2p shows Mn $2p_{3/2}$ and Mn $2p_{1/2}$ peaks at the binding energy of 642.8 eV and 654.2 eV, respectively. The core level spectrum of O 1s shows a strong peak at 529.8 eV with a shoulder from ~530.9 eV to 534 eV, which could be predominantly due to MnO bonds. Furthermore, Fig. 4(b) shows the core level spectra of C 1s, S 2p, Fe 2p, N 1s, and O 1s obtained from the as-prepared CFe/PANI/NiGF. From these XPS core level spectra, the C 1s peak at 284.6 eV appears broad and asymmetric due to different carbon compounds/oxides (e.g., COH/CN at 286.5 eV, COC at 287.6 eV, C=O at 288.9 eV, etc.) present in the sample, which are attributed to the functional groups of PANI.[65,66] The core level spectrum of S 2p shows peaks at 160.7 eV and 161.9 eV corresponding to S $2p_{3/2}$ and S $2p_{1/2}$ levels, respectively. These peaks are attributed to the S^{2-} ions and also confirm the FeS, SC, SS, and SS/SC bond-related peaks, which appear at 161.9 eV, 163.2 eV, 163.8 eV, and 164.8 eV, respectively.[67] The Fe 2p spectrum shows one of the binding energy peaks at 706.8 eV, which corresponds to Fe^0, Fe^{2+}, and Fe^{3+} ions.[68] The N 1s spectrum shows nitrogencarbon bond-related peaks at 398.7 eV (pyridinic N), 400.4 eV (pyrrolic N), and 401.5 eV (graphitic N).[69] The spectrum of O 1s shows a broad and asymmetric peak at 532.3 eV due to oxygen components, such as COH/COC and C=O, which appears at 532.7 eV and 530.9 eV, respectively.[70]

B. Electrochemistry

The as-prepared electrodes were evaluated in three-electrode and two-electrode systems using 2.5M KNO_3 electrolyte. In three-electrode configuration, the CV curves of the as-prepared positive (MnO_2C composite) and negative (CFe/PANI/NiGF) electrodes at different scan rates (5–100 mV s^{-1}) in the potential window range of 0.0–1.1 V vs Ag/AgCl and −1.1 V to 0.0 V vs Ag/AgCl are presented in Figs. 5(a) and 5(b), respectively. Figure 5(a) shows the CV curves of the positive electrode, which show symmetric quasi-rectangular and reversible pseudocapacitive behavior. Similarly, the CV curves of the negative electrode displayed in Fig. 5(b) show pseudocapacitive behavior without obvious redox peaks.[7] The CV curves are in agreement with the GCD curves of positive and negative electrodes, which are presented in Figs. 5(c) and 5(d), respectively. The GCD curves of the as-prepared electrodes also show pseudocapacitive behavior. Due to this behavior, the specific capacitance of the as-prepared electrodes was calculated from GCD curves using Eq. (2). The plot of specific capacitance as a function of a specific current is shown in Fig. 5(e). The specific capacitances of the as-prepared electrodes (positive and negative) are 76.8 F g^{-1} and 114.4 F g^{-1} at a specific current of 2 A g^{-1}, respectively.

The as-prepared electrodes were further tested in two-electrode configuration; the electrochemical performance of the as-prepared electrodes was fully explored by fabricating an asymmetric device as shown in Fig. 6(a). The charge balance ($Q_+ = Q_-$) of the two electrodes is required since they have different specific capacitances [Fig. 5(e)], where $Q_+ = C_{S(+)} \times m_+ \times \Delta V_+$ and $Q_- = C_{S(-)} \times m_- \times \Delta V_-$ are charges stored in both positive and negative electrodes, respectively. The mass balance was expressed using Eq. (3). From Fig. 5(e), the mass ratio ($m_+/m_- \approx 0.7$) at a specific current of 2 A g^{-1} was used for mass balance. Consequently, the masses of the positive electrode and negative electrode were obtained as 1.7 mg/cm^2 and 2.5 mg/cm^2, respectively, which gives the total mass of the cell as 4.2 mg/cm^2.

The as-fabricated MnO_2C//CFe/PANI/NiGF asymmetric device was able to reach the potential of 2.2 V [Fig. 6(b)]. The CV curves of the device [Fig. 6(c)] show pseudocapacitive behavior; with the increase in scan rate, the CV curves do not change, hence suggesting

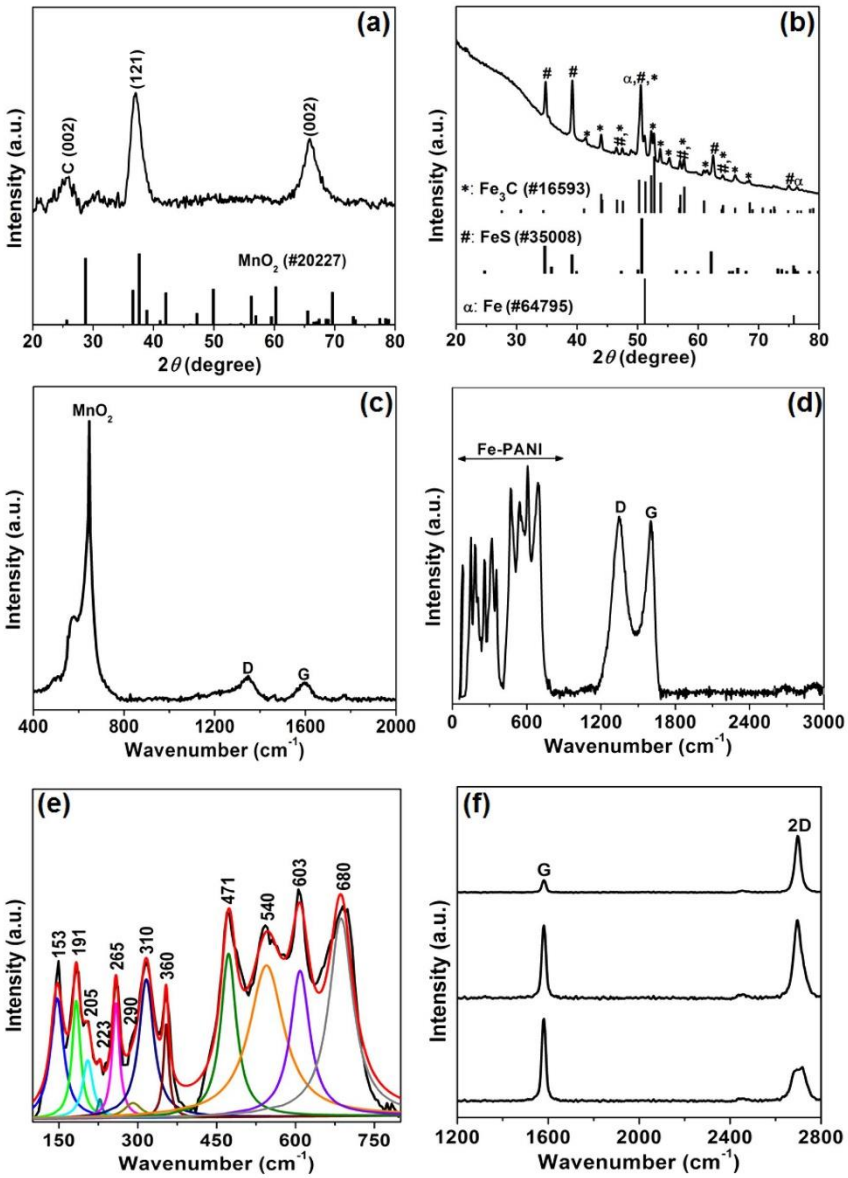

FIG. 3. [(a) and (b)] The XRD pattern and the matching ICSD cards of the as-prepared electrodes, MnO_2C composite, and CFe/PANI/NiGF, respectively. Raman spectra of (c) MnO_2C composites, [(d) and (e)] CFe/PANI/NiGF, and (f) NGF.

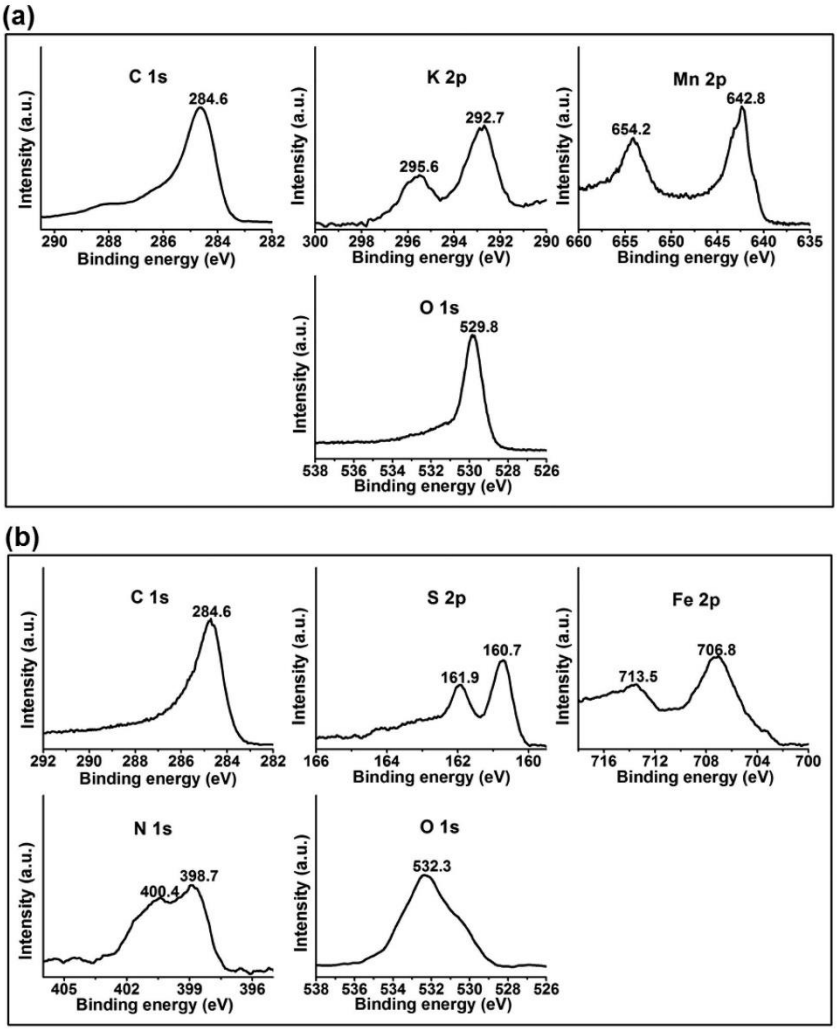

FIG. 4. The XPS core level spectra obtained from the as-prepared (a) MnO_2 and (b) CFe/PANI/NiGF.

that the device is stable. The GCD curves of the device at different specific currents in the range of 1 A g^{-1}–10 A g^{-1} are shown in Fig. 6(d). The specific capacitance of the device as a function of the specific current is shown in Fig. 6(e). At a low specific current of 1 A g^{-1}, the device exhibited a high specific capacitance of 51.5 F g^{-1}, and this is maintained at 30.6 F g^{-1} at a high specific current of 10 A g^{-1}.

The energy density (E_d) and the power density (P_d) of the device were calculated from the GCD curves using Eqs. (4) and (5), respectively. The Ragone plot in Fig. 7(a) shows the energy density

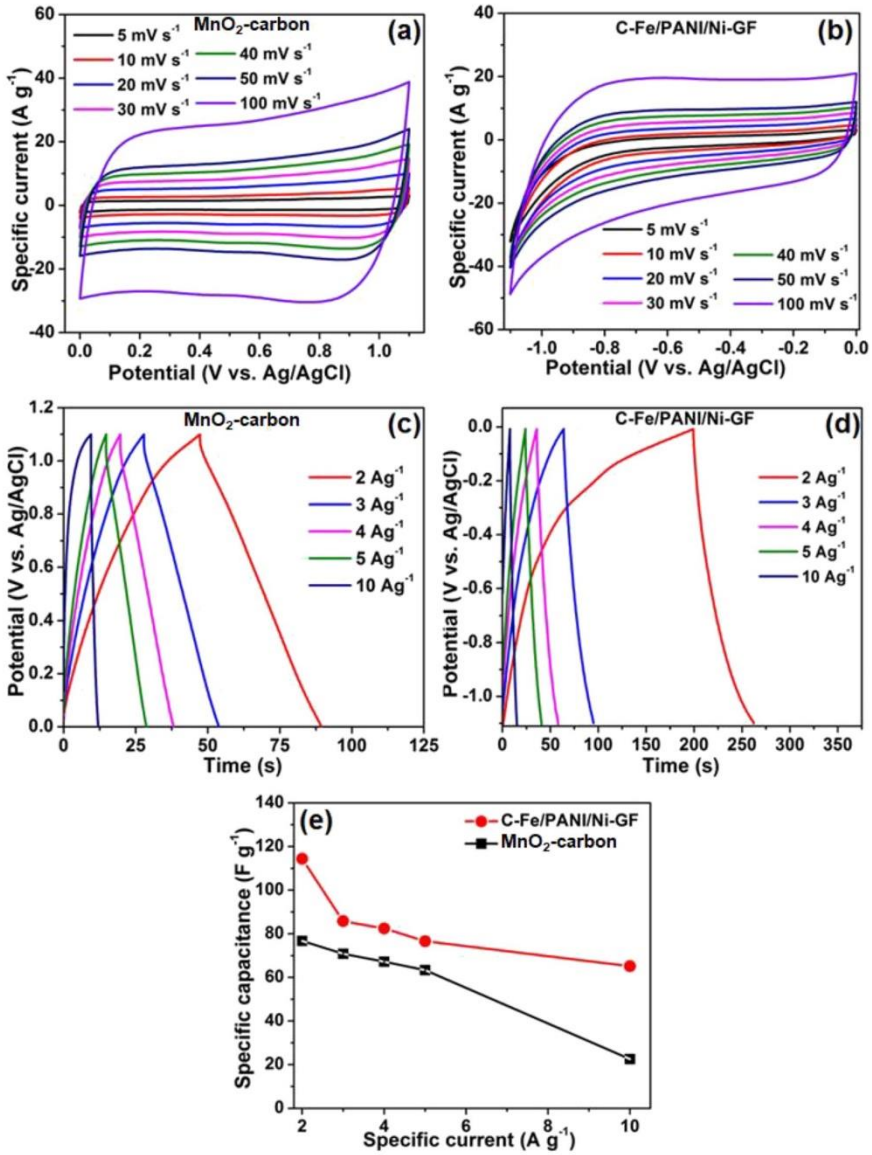

FIG. 5. [(a) and (b)] CV curves of positive and negative electrodes at different scan rates in the potential window range of 0.0–1.1 V and −1.1 V to 0.0 V, respectively. [(c) and (d)] GCD curves of the positive and negative electrodes at different specific currents in the range of 2 A g^{-1}–10 A g^{-1}, respectively. (e) The specific capacitance of both electrodes as a function of specific current.

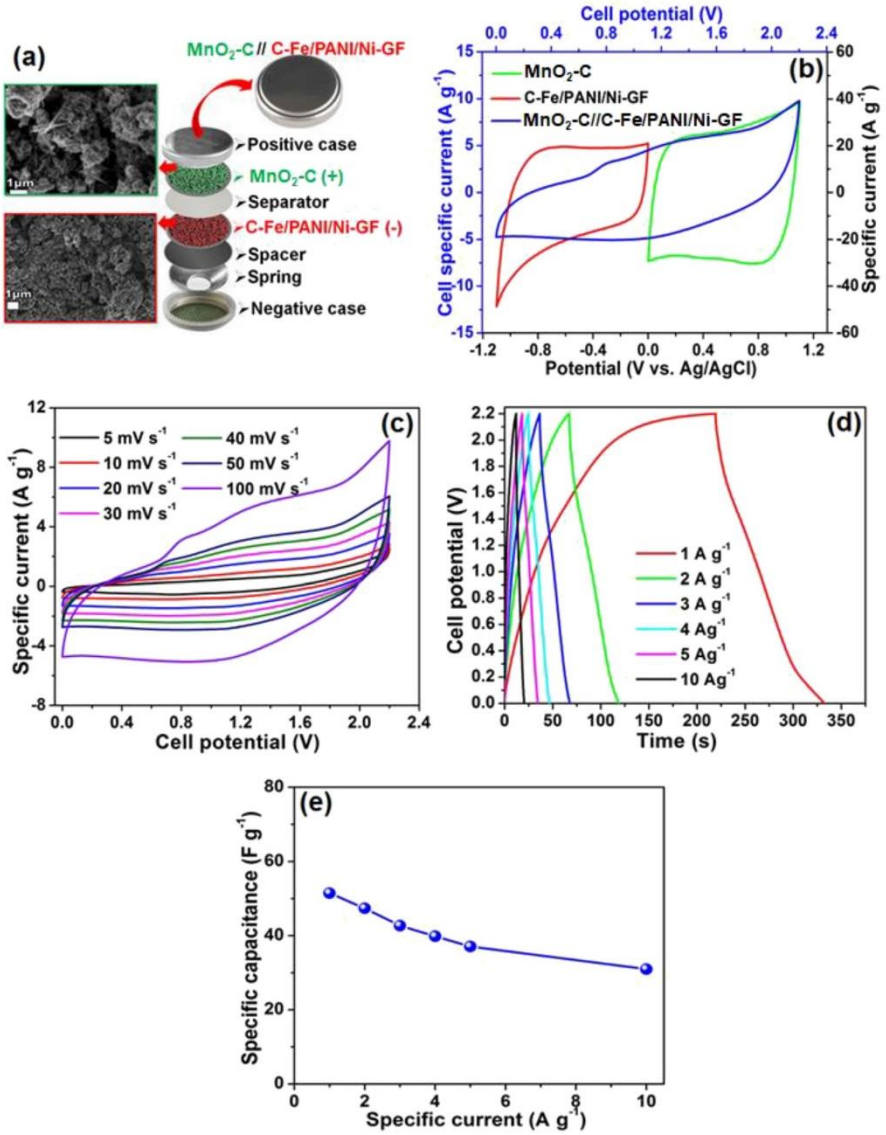

FIG. 6. (a) Scheme of the as-fabricated asymmetric supercapacitor device based on the MnO_2C composite as a positive and CFe/PANI/NiGF as a negative. (b) CV curves of both positive and negative electrodes at a scan rate of 100 mV s^{-1} evaluated in three-electrode and the as-fabricated MnO_2C//CFe/PANI/NiGF asymmetric device. For the as-fabricated asymmetric device: (c) CV curves at different scan rates in the range of 5–100 mV s^{-1}, (d) GCD curves at different current densities in the range of 1–10 A g^{-1}, and (e) the specific capacitance as a function of the specific current.

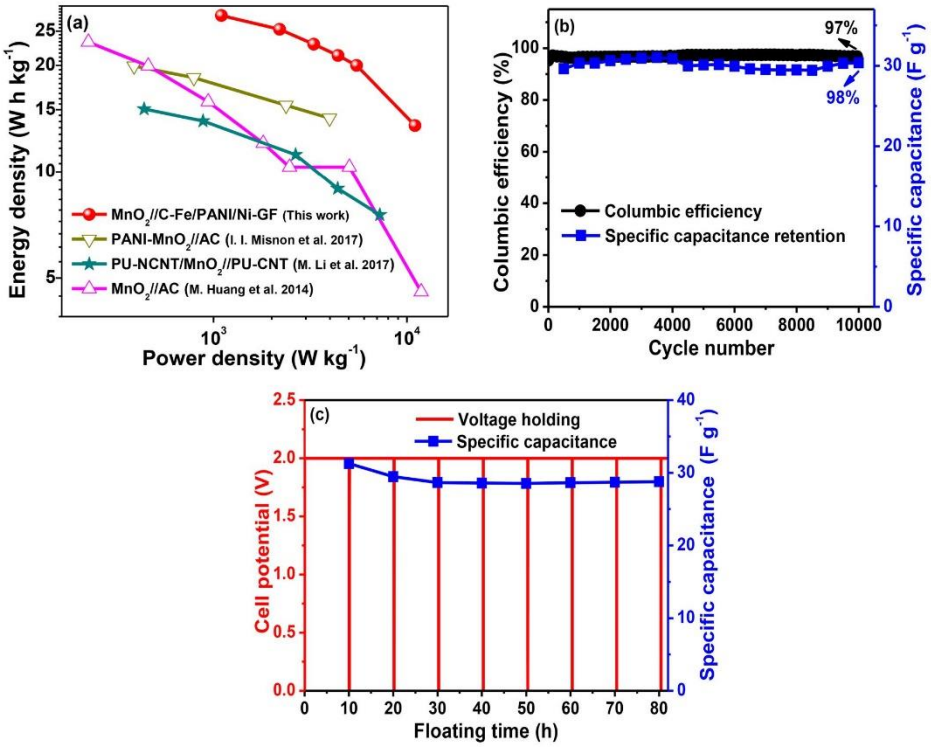

FIG. 7. (a) Energy and power densities of the MnO_2C//CFe/PANI/NiGF asymmetric device and MnO_2-based asymmetric devices reported in the literature. (b) The cycling stability test for the as-fabricated device at a specific current of 10 A g^{-1}. (c) Voltage holding and specific capacitance as a function of floating time evaluated at a specific current of 10 A g^{-1}.

as a function of power density. The as-fabricated asymmetric device exhibited a maximum energy density of 34.6 W h kg^{-1} and the corresponding power density of 1100.0 W kg^{-1}, at a specific current of 1.0 A g^{-1}. At a high specific current of 10 A g^{-1}, the device exhibited a high energy density of 20.6 W h kg^{-1} and the corresponding maximum power density of 11 661.7 W kg^{-1}. The as-fabricated asymmetric device exhibited energy and power densities that are higher than or comparable to MnO_2-based asymmetric devices reported in the literature as shown in Fig. 7(a) and Table I. These values of energy and power densities are quite impressive especially that at such high energy density values, the power density values are this high, which is not usually the case. Figure 7(b) shows the cycling stability test of the as-fabricated asymmetric device performed at a specific current of 10 A g^{-1}. The device exhibited a columbic efficiency of 97% and 98% capacitance retention after a 10 000th galvanostatic charge–discharge cycle. The stability of the device was further tested using voltage holding at 10 A g^{-1} and a maximum operating potential of 2.2 V for 80 h, as shown in Fig. 7(c). The figure shows excellent stability in the specific capacitance of the device over 80 h of voltage holding.

The electrochemical impedance spectroscopy analysis of the as-fabricated asymmetric device before and after cycling stability was carried out, as shown by the Nyquist plot in Fig. 8(a). The Nyquist plot shows a linear component in the low-frequency region, which is slightly tilted with bigger angle than 45° signifying a deviation from ideal capacitive behavior. An ideal supercapacitor exhibits a typical vertical line parallel to the y axis with a mass capacitance (Q_2). The intersection of the Nyquist plot on the x axis in the high-frequency region describes the equivalent series resistance (R_S), which is in series with the charge transfer resistance (R_{CT}) and Warburg impedance characteristic element (W) connected in parallel to the real capacitance (Q_1) [see the inset of Fig. 8(b)].[71]

TABLE I. Electrochemical performance comparison of MnO_x-based aqueous electrochemical capacitors.

Positive electrode	Negative electrode	Electrolyte	Current density ($A\ g^{-1}$)	Potential window (V)	Energy density ($W\ h\ kg^{-1}$)	Power density ($W\ kg^{-1}$)	References
MnO_2	AC	1M Na_2SO_4	0.1	2.0	17.1	100	Zhang *et al.*[41]
MnO_2	AC	1M Na_2SO_4	0.25	1.8	22.5	146 200	Huang *et al.*[20]
MnO_2	AC	0.1M K_2SO_4	0.55	2.2	17.3	605	Cottineau *et al.*[42]
MnO_2	AC	0.5M K_2SO_4	...	1.8	28.4	150	Qu *et al.*[43]
OLC/Mn_3O_4	AC	1M Na_2SO_4	0.1	2.0	19.0	45 000[a]	Makgopa *et al.*[44]
PANI–MnO_2	AC	6M KOH	0.5	1.6	20	400	Misnon and Jose[45]
MnO_2/CNT	AC	1M Na_2SO_4	0.25	1.8	27.0	225	Gueon and Moon[25]
MnO_2/CNT	AC	0.5M Na_2SO_4	1.0	2.0	13.9	...	Demarconnay *et al.*[22]
MnO_2/CNT	AC	2M KNO_3	0.1	2.0	21.0	123	Khomenko *et al.*[46]
Graphene/MnO_2	AC	1M Na_2SO_4	...	1.8	51.1[b]	102.2[b]	Fan *et al.*[31]
MnO_2/CNT	AC	1M Na_2SO_4	1.0	1.5	13.3	600	Li *et al.*[21]
MnO_2–CNT	AC	1M Li_2SO_4	0.5	2.0	24.58	500	Ochai-Ejeh *et al.*[32]
MnO_2graphene	Graphene	1M Na_2SO_4	2.23	1.7	10.03	2 530	Deng *et al.*[33]
Graphene/MnO_2	Graphene	1M Na_2SO_4	5.0	2.0	7.0	5 000	Wu *et al.*[34]
MnO_2	Graphene	0.5M Na_2SO_4	1.0	2.0	23.2	1 000	Gao *et al.*[35]
Graphene/MnO_2	Graphene/Ag	1M Na_2SO_4	...	1.8	50.8[b]	101[b]	Shao *et al.*[36]
MnO_2	CNTs	1M Na_2SO_4	0.2	2.0	47.4	200	Jiang *et al.*[37]
MnO_2	Bacterial cellulose	1M Na_2SO_4	1.0	2.0	32.91	284 630	Chen *et al.*[38]
PU–NCNT/MnO_2	PU–CNT	1M Na_2SO_4	1.0	1.8	14.76	~438	Li *et al.*[39]
OLC/MnO_2	OLC/MnO_2	1M Na_2SO_4	0.1	0.8	5.6	74 800[a]	Makgopa *et al.*[40]
MnO_2	Fe_3O_4	0.1M K_2SO_4	0.45	1.8	8.1	405	Cottineau *et al.*[42]
MnO_2C	CFe/PANI/NiGF	2.5M KNO_3	1.0	2.2	34.6	1 100	This work

[a]Calculation based on the EIS maximum power (P_{max}).
[b]Calculation from CV curves.

The Nyquist plot of the device before and after cycling stability shows a comparable R_S of ~1 Ω [see the inset of Fig. 8(a)] indicating that the electrodes have good chemical stability. The circuit diagram was used to fit the Nyquist plot [inset of Fig. 8(b)]. The circuit diagram indicates that the deviation of the supercapacitor behavior from an ideal capacitive behavior is attributed to a leakage resistance (R_L), which is parallel to the mass capacitance (Q_2).[72,73]

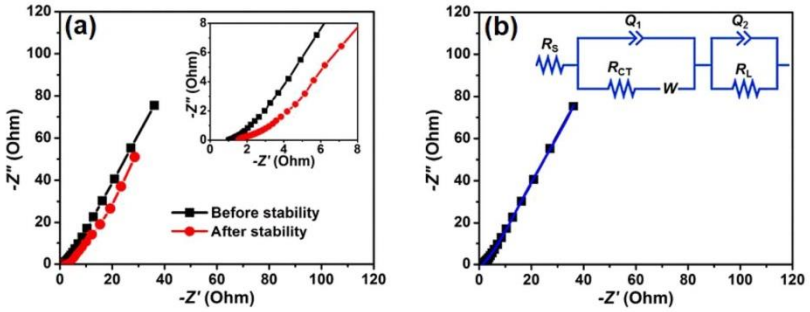

FIG. 8. (a) Nyquist plots of the as-fabricated asymmetric device before and after stability (the inset shows the enlarged high-frequency region). (b) The Nyquist plot and the fit of the equivalent circuit diagram in the inset of the figure.

IV. CONCLUSION

In this work, the CFe/PANI was grown on NiGF and showed improvement in electrochemical properties. The asymmetric device was fabricated based on the birnessite-type MnO_2carbon composite and the CFe/PANI/NiGF as positive and negative electrodes, respectively. The as-fabricated asymmetric device at a specific current of 1.0 A g^{-1} and cell potential window of 0.0–2.2 V exhibited maximum energy and power densities of 34.6 W h kg^{-1} and 1100.0 W kg^{-1}, respectively. At a high specific current of 10 A g^{-1}, the device exhibited a high energy density of 20.6 W h kg^{-1} and a corresponding maximum power density of 11 661.7 W kg^{-1}. The device displayed remarkable stability with a capacitance retention of 98% up to 10 000 constant GCD cycles. The stability was tested further using voltage holding at a potential of 2.2 V up to 80 h and still displayed excellent stability.

ACKNOWLEDGMENTS

This work was based on research supported by the South African Research Chairs Initiative (SARChI) of the Department of Science and Technology and the National Research Foundation (NRF) of South Africa (Grant No. 61056). Any opinion, finding and conclusion, or recommendation expressed in this material is that of the authors, and the NRF does not accept any liability in this regard. M. N. Rantho acknowledges the funding from the University of Pretoria and NRF through SARChI in Carbon Technology and Materials.

DATA AVAILABILITY

The data that support the findings of this study are available from the corresponding author upon reasonable request.

REFERENCES

[1]S. W. Zhang and G. Z. Chen, "Manganese oxide based materials for supercapacitors," Energy Mater. **3**, 186–200 (2008).
[2]E. Frackowiak and F. Béguin, "Carbon materials for the electrochemical storage of energy in capacitors," Carbon **39**, 937–950 (2001).
[3]H. Pan, J. Li, and Y. P. Feng, "Carbon nanotubes for supercapacitor," Nanoscale Res. Lett. **5**, 654–668 (2010).
[4]L. L. Zhang and X. S. Zhao, "Carbon-based materials as supercapacitor electrodes," Chem. Soc. Rev. **38**, 2520 (2009).
[5]E. Frackowiak, "Carbon materials for supercapacitor application," Phys. Chem. Chem. Phys. **9**, 1774 (2007).
[6]S. Mondal, U. Rana, and S. Malik, "Reduced graphene oxide/Fe_3O_4/polyaniline nanostructures as electrode materials for an all-solid-state hybrid supercapacitor," J. Phys. Chem. C **121**, 7573–7583 (2017).
[7]M. N. Rantho, M. J. Madito, and N. Manyala, "High-performance symmetric supercapacitor device based on carbonized iron-polyaniline/nickel graphene foam," J. Alloys Compd. **819**, 152993 (2019).
[8]W. Zuo, R. Li, C. Zhou, Y. Li, J. Xia, and J. Liu, "Battery-supercapacitor hybrid devices: Recent progress and future prospects," Adv. Sci. **4**, 1–21 (2017).
[9]F. Wang, X. Wu, X. Yuan, and Z. Liu, "Latest advances in supercapacitors: From new electrode materials to novel device designs," Chem. Soc. Rev. **46**, 6816–6854 (2017).
[10]G. Wang, L. Zhang, and J. Zhang, "A review of electrode materials for electrochemical supercapacitors," Chem. Soc. Rev. **41**, 797–828 (2012).
[11]K. R. Prasad, K. Koga, and N. Miura, "Electrochemical deposition of nanostructured indium oxide: High-performance electrode material for redox supercapacitors," Chem. Mater. **16**(10), 1845–1847 (2004).
[12]M. Kalaji, P. J. Murphy, and G. O. Williams, "The study of conducting polymers for use as redox supercapacitors," Synth. Met. **102**, 1360–1361 (1999).
[13]Y. Zhou, B. He, W. Zhou, J. Huang, X. Li, B. Wu, and H. Li, "Electrochemical capacitance of well-coated single-walled carbon nanotube with polyaniline composites," Electrochim. Acta **49**, 257–262 (2004).
[14]K. S. Ryu, K. M. Kim, N.-G. Park, Y. J. Park, and S. H. Chang, "Symmetric redox supercapacitor with conducting polyaniline electrodes," J. Power Sources **103**, 305–309 (2002).
[15]H. Mi, X. Zhang, X. Ye, and S. Yang, "Preparation and enhanced capacitance of core–shell polypyrrole/polyaniline composite electrode for supercapacitors," J. Power Sources **176**, 403–409 (2008).
[16]C. Portet, P. L. Taberna, P. Simon, E. Flahaut, and C. Laberty-Robert, "High power density electrodes for carbon supercapacitor applications," Electrochim. Acta **50**, 4174–4181 (2005).
[17]M. N. Rantho, M. J. Madito, and N. Manyala, "Symmetric supercapacitor with supercapattery behavior based on carbonized iron cations adsorbed onto polyaniline," Electrochim. Acta **262**, 82 (2018).
[18]H. Wang, Q. Hao, X. Yang, L. Lu, and X. Wang, "A nanostructured graphene/polyaniline hybrid material for supercapacitors," Nanoscale **2**, 2164 (2010).
[19]M. Yu, Y. Huang, C. Li, Y. Zeng, W. Wang, Y. Li, P. Fang, X. Lu, and Y. Tong, "Building three-dimensional graphene frameworks for energy storage and catalysis," Adv. Funct. Mater. **25**, 324–330 (2015).
[20]M. Huang, Y. Zhang, F. Li, L. Zhang, R. S. Ruoff, Z. Wen, and Q. Liu, "Self-assembly of mesoporous nanotubes assembled from interwoven ultrathin birnessite-type MnO_2 nanosheets for asymmetric supercapacitors," Sci. Rep. **4**, 3878 (2014).
[21]L. Li, Z. A. Hu, N. An, Y. Y. Yang, Z. M. Li, and H. Y. Wu, "Facile synthesis of MnO_2/CNTs composite for supercapacitor electrodes with long cycle stability," J. Phys. Chem. C **118**, 22865–22872 (2014).
[22]L. Demarconnay, E. Raymundo-Piñero, and F. Béguin, "Adjustment of electrodes potential window in an asymmetric carbon/MnO_2 supercapacitor," J. Power Sources **196**, 580–586 (2011).
[23]T. Brousse, P.-L. Taberna, O. Crosnier, R. Dugas, P. Guillemet, Y. Scudeller, Y. Zhou, F. Favier, D. Bélanger, and P. Simon, "Long-term cycling behavior of asymmetric activated carbon/MnO_2 aqueous electrochemical supercapacitor," J. Power Sources **173**, 633–641 (2007).
[24]Y. Jin, H. Chen, M. Chen, N. Liu, and Q. Li, "Graphene-patched CNT/MnO_2 nanocomposite papers for the electrode of high-performance flexible asymmetric supercapacitors," ACS Appl. Mater. Interfaces **5**, 3408–3416 (2013).
[25]D. Gueon and J. H. Moon, "MnO_2 nanoflake-shelled carbon nanotube particles for high-performance supercapacitors," ACS Sustainable Chem. Eng. **5**, 2445–2453 (2017).
[26]B. Brown, I. A. Cordova, C. B. Parker, B. R. Stoner, and J. T. Glass, "Optimization of active manganese oxide electrodeposits using graphenated carbon nanotube electrodes for supercapacitors," Chem. Mater. **27**, 2430–2438 (2015).
[27]J. Jiang, Y. Li, J. Liu, X. Huang, C. Yuan, and X. W. D. Lou, "Recent advances in metal oxide-based electrode architecture design for electrochemical energy storage," Adv. Mater. **24**, 5166–5180 (2012).
[28]G. Lota, K. Fic, and E. Frackowiak, "Carbon nanotubes and their composites in electrochemical applications," Energy Environ. Sci. **4**, 1592 (2011).
[29]X. Hu, H. Nan, M. Liu, S. Liu, T. An, and H. Tian, "Battery-like $MnCo_2O_4$ electrode materials combined with active carbon for hybrid supercapacitors," Electrochim. Acta **306**, 599–609 (2019).
[30]H. Tian, X. Lang, H. Nan, P. An, W. Zhang, X. Hu, and J. Zhang, "Nanosheet-assembled $LaMnO_3$@$NiCo_2O_4$ nanoarchitecture growth on Ni foam for high power density supercapacitors," Electrochim. Acta **318**, 651 (2019).
[31]Z. Fan, J. Yan, T. Wei, L. Zhi, G. Ning, T. Li, and F. Wei, "Asymmetric supercapacitors based on graphene/MnO_2 and activated carbon nanofiber electrodes with high power and energy density," Adv. Funct. Mater. **21**, 2366–2375 (2011).

[32]F. Ochai-Ejeh, M. J. Madito, K. Makgopa, M. N. Rantho, O. Olaniyan, and N. Manyala, "Electrochemical performance of hybrid supercapacitor device based on birnessite-type manganese oxide decorated on uncapped carbon nanotubes and porous activated carbon nanostructures," Electrochim. Acta **289**, 363–375 (2018).
[33]L. Deng, G. Zhu, J. Wang, L. Kang, Z.-H. Liu, Z. Yang, and Z. Wang, "Graphene–MnO_2 and graphene asymmetrical electrochemical capacitor with a high energy density in aqueous electrolyte," J. Power Sources **196**, 10782–10787 (2011).
[34]Z.-S. Wu, W. Ren, D.-W. Wang, F. Li, B. Liu, and H.-M. Cheng, "High-energy MnO_2 nanowire/graphene and graphene asymmetric electrochemical capacitors," ACS Nano **4**, 5835–5842 (2010).
[35]H. Gao, F. Xiao, C. B. Ching, and H. Duan, "High-performance asymmetric supercapacitor based on graphene hydrogel and nanostructured MnO_2," ACS Appl. Mater. Interfaces **4**, 2801–2810 (2012).
[36]Y. Shao, H. Wang, Q. Zhang, and Y. Li, "High-performance flexible asymmetric supercapacitors based on 3D porous graphene/MnO_2 nanorod and graphene/Ag hybrid thin-film electrodes," J. Mater. Chem. C **1**, 1245–1251 (2013).
[37]H. Jiang, C. Li, T. Sun, and J. Ma, "A green and high energy density asymmetric supercapacitor based on ultrathin MnO_2 nanostructures and functional mesoporous carbon nanotube electrodes," Nanoscale **4**, 807–812 (2012).
[38]L.-F. Chen, Z.-H. Huang, H.-W. Liang, Q.-F. Guan, and S.-H. Yu, "Bacterial-cellulose-derived carbon nanofiber@MnO_2 and nitrogen-doped carbon nanofiber electrode materials: An asymmetric supercapacitor with high energy and power density," Adv. Mater. **25**, 4746–4752 (2013).
[39]M. Li, Q. Chen, and H. Zhan, "Ultrathin manganese dioxide nanosheets grown on partially unzipped nitrogen-doped carbon nanotubes for high-performance asymmetric supercapacitors," J. Alloys Compd. **702**, 236–243 (2017).
[40]K. Makgopa, P. M. Ejikeme, C. J. Jafta, K. Raju, M. Zeiger, V. Presser, and K. I. Ozoemena, "A high-rate aqueous symmetric pseudocapacitor based on highly graphitized onion-like carbon/birnessite-type manganese oxide nanohybrids," J. Mater. Chem. A **3**, 3480–3490 (2015).
[41]X. Zhang, P. Yu, H. Zhang, D. Zhang, X. Sun, and Y. Ma, "Rapid hydrothermal synthesis of hierarchical nanostructures assembled from ultrathin birnessite-type MnO_2 nanosheets for supercapacitor applications," Electrochim. Acta **89**, 523–529 (2013).
[42]T. Cottineau, M. Toupin, T. Delahaye, T. Brousse, and D. Bélanger, "Nanostructured transition metal oxides for aqueous hybrid electrochemical supercapacitors," Appl. Phys. A **82**, 599–606 (2006).
[43]Q. Qu, P. Zhang, B. Wang, Y. Chen, S. Tian, Y. Wu, and R. Holze, "Electrochemical performance of MnO_2 nanorods in neutral aqueous electrolytes as a cathode for asymmetric supercapacitors," J. Phys. Chem. C **113**, 14020–14027 (2009).
[44]K. Makgopa, K. Raju, P. M. Ejikeme, and K. I. Ozoemena, "High-performance Mn_3O_4/onion-like carbon (OLC) nanohybrid pseudocapacitor: Unravelling the intrinsic properties of OLC against other carbon supports," Carbon **117**, 20–32 (2017).
[45]I. I. Misnon and R. Jose, "Synthesis and electrochemical evaluation of the PANI/δ-MnO_2 electrode for high performing asymmetric supercapacitors," New J. Chem. **41**, 6574–6584 (2017).
[46]V. Khomenko, E. Raymundo-Piñero, and F. Béguin, "Optimisation of an asymmetric manganese oxide/activated carbon capacitor working at 2 V in aqueous medium," J. Power Sources **153**, 183–190 (2006).
[47]J. Fei, J. Zhao, H. Zhang, A. Wang, C. Qin, P. Cai, X. Feng, and J. Li, "One-pot mass self-assembly of MnO_2 sponge-like hierarchical nanostructures through a limited hydrothermal reaction and their environmental applications," J. Colloid Interface Sci. **490**, 621–627 (2017).
[48]B. Akinwolemiwa, C. Peng, and G. Z. Chen, "Redox electrolytes in supercapacitors," J. Electrochem. Soc. **162**, A5054–A5059 (2015).
[49]A. Laheäär, P. Przygocki, Q. Abbas, and F. Béguin, "Appropriate methods for evaluating the efficiency and capacitive behavior of different types of supercapacitors," Electrochem. Commun. **60**, 21–25 (2015).
[50]P. Simon and Y. Gogotsi, "Materials for electrochemical capacitors," Nat. Mater. **7**, 845–854 (2008).
[51]F. O. Ochai-Ejeh, M. J. Madito, D. Y. Momodu, A. A. Khaleed, O. Olaniyan, and N. Manyala, "High performance hybrid supercapacitor device based on cobalt manganese layered double hydroxide and activated carbon derived from cork (quercus suber)," Electrochim. Acta **252**, 41–54 (2017).
[52]C. Mattevi, H. Kim, and M. Chhowalla, "A review of chemical vapour deposition of graphene on copper," J. Mater. Chem. **21**, 3324–3334 (2011).
[53]M. Zhao and H. Song, "Synthesis of carbon-encapsulated iron carbide/iron nanoparticles from phenolic-formaldehyde resin and ferric nitrate," Mater. Chem. Phys. **124**, 861–864 (2010).
[54]T. K. Gupta, B. P. Singh, V. N. Singh, S. Teotia, A. P. Singh, I. Elizabeth, S. R. Dhakate, S. K. Dhawan, and R. B. Mathur, "MnO_2 decorated graphene nanoribbons with superior permittivity and excellent microwave shielding properties," J. Mater. Chem. A **2**, 4256–4263 (2014).
[55]C. Röder, T. Weißbach, C. Himcinschi, J. Kortus, S. Dudczig, and C. G. Aneziris, "Raman spectroscopic characterization of novel carbon-bonded filter compositions for steel melt filtration," J. Raman Spectrosc. **45**, 128–132 (2014).
[56]J. Zhang, C. Liu, and G. Shi, "Raman spectroscopic study on the structural changes of polyaniline during heating and cooling processes," J. Appl. Polym. Sci. **96**, 732–739 (2005).
[57]M. Sawangphruk, M. Suksomboon, K. Kongsupornsak, J. Khuntilo, P. Srimuk, Y. Sanguansak, P. Klunbud, P. Suktha, and P. Chiochan, "High-performance supercapacitors based on silver nanoparticle-polyaniline-graphene nanocomposites coated on flexible carbon fiber paper," J. Mater. Chem. A **1**, 9630–9636 (2013).
[58]C. Avril, V. Malavergne, R. Caracas, B. Zanda, B. Reynard, E. Charon, E. Bobocioiu, F. Brunet, S. Borensztajn, S. Pont, M. Tarrida, and F. Guyot, "Raman spectroscopic properties and Raman identification of CaS-MgS-MnS-FeS-Cr_2FeS_4 sulfides in meteorites and reduced sulfur-rich systems," Meteorit. Planet. Sci. **48**, 1415–1426 (2013).
[59]J.-A. Bourdoiseau, M. Jeannin, R. Sabot, C. Rémazeilles, and P. Refait, "Characterisation of mackinawite by Raman spectroscopy: Effects of crystallisation, drying and oxidation," Corros. Sci. **50**, 3247–3255 (2008).
[60]E. B. Hansson, M. S. Odziemkowski, and R. W. Gillham, "Formation of poorly crystalline iron monosulfides: Surface redox reactions on high purity iron, spectroelectrochemical studies," Corros. Sci. **48**, 3767–3783 (2006).
[61]P. Colomban, S. Cherifi, and G. Despert, "Raman identification of corrosion products on automotive galvanized steel sheets," J. Raman Spectrosc. **39**, 881–886 (2008).
[62]X. Yang, C. Li, J. Huang, Y. Liu, W. Chen, J. Shen, Y. Zhu, and C. Li, "Nitrogen-doped Fe_3C@C particles as an efficient heterogeneous photo-assisted fenton catalyst," RSC Adv. **7**, 15168–15175 (2017).
[63]M. K. Nieuwoudt, J. D. Comins, and I. Cukrowski, "The growth of the passive film on iron in 0.05M NaOH studied *in situ* by Raman micro-spectroscopy and electrochemical polarisation. Part I: Near-resonance enhancement of the Raman spectra of iron oxide and oxyhydroxide compounds," J. Raman Spectrosc. **42**, 1335–1339 (2011).
[64]N. M. Ndiaye, B. D. Ngom, N. F. Sylla, T. M. Masikhwa, M. J. Madito, D. Momodu, T. Ntsoane, and N. Manyala, "Three dimensional vanadium pentoxide/graphene foam composite as positive electrode for high performance asymmetric electrochemical supercapacitor," J. Colloid Interface Sci. **532**, 395–406 (2018).
[65]X. Feng, Z. Yan, N. Chen, Y. Zhang, X. Liu, Y. Ma, X. Yang, and W. Hou, "Synthesis of a graphene/polyaniline/MCM-41 nanocomposite and its application as a supercapacitor," New J. Chem. **37**, 2203 (2013).
[66]S. K. Lai, C. M. Luk, L. Tang, K. S. Teng, and S. P. Lau, "Photoresponse of polyaniline-functionalized graphene quantum dots," Nanoscale **7**, 5338–5343 (2015).
[67]M. V. Morales-Gallardo, A. M. Ayala, M. Pal, M. A. Cortes Jacome, J. A. Toledo Antonio, and N. R. Mathews, "Synthesis of pyrite FeS_2 nanorods by simple hydrothermal method and its photocatalytic activity," Chem. Phys. Lett. **660**, 93–98 (2016).
[68]G. H. Le, A. Q. Ha, Q. K. Nguyen, K. T. Nguyen, P. T. Dang, H. T. K. Tran, L. D. Vu, T. V. Nguyen, G. D. Lee, and T. A. Vu, "Removal of Cd^{2+} and Cu^{2+} ions from aqueous solution by using Fe–Fe_3O_4/graphene oxide as a novel and efficient adsorbent," Mater. Res. Express **3**, 105603 (2016).

[69]G. Wu, C. M. Johnston, N. H. Mack, K. Artyushkova, M. Ferrandon, M. Nelson, J. S. Lezama-Pacheco, S. D. Conradson, K. L. More, D. J. Myers, and P. Zelenay, "Synthesis–structure–performance correlation for polyaniline–Me–C non-precious metal cathode catalysts for oxygenreduction in fuelcells," J. Mater. Chem. **21**, 11392–11405 (2011).
[70]Y. Luo, D. Kong, Y. Jia, J. Luo, Y. Lu, D. Zhang, K. Qiu, C. M. Li, and T. Yu, "Self-assembled graphene@PANI nanoworm composites with enhanced supercapacitor performance," RSC Adv. **3**, 5851–5859 (2013).
[71]Y. Zhou, H. Xu, N. Lachman, M. Ghaffari, S. Wu, Y. Liu, A. Ugur, K. K. Gleason, B. L. Wardle, and Q. M. Zhang, "Advanced asymmetric supercapacitor based on conducting polymer and aligned carbon nanotubes with controlled nanomorphology," Nano Energy **9**, 176–185 (2014).
[72]W. Sun and X. Chen, "Preparation and characterization of polypyrrole films for three-dimensional micro supercapacitor," J. Power Sources **193**, 924–929 (2009).
[73]H. Li, J. Wang, Q. Chu, Z. Wang, F. Zhang, and S. Wang, "Theoretical and experimental specific capacitance of polyaniline in sulfuric acid," J. Power Sources **190**, 578–586 (2009).

4.3.3 Concluding remark

The birnessite-type MnO_2/carbon composite with hierarchical nanostructures was successfully synthesized using $KMnO_4$ solution and spent printing carbon grains. Birnessite-type MnO_2/carbon composite was used as positive electrode and C-Fe/PANI/Ni-GF as a negative electrode. The device was fabricated based on positive and negative electrodes using 2.5 M KNO_3 electrolyte. At the lowest specific current of 1.0 A g^{-1} and cell potential of 2.2 V, the device displayed a high specific energy and specific power of 34.6 W h kg^{-1} and 1100.0 W kg^{-1}, respectively. The device further displayed long-term cycling stability with capacitance retention of 98% over 10 000 galvanostatic charge-discharge cycles at 10 A g^{-1}.

Chapter 5

General conclusions and future work

5.1 General conclusions

In this work, the electrochemical properties of both MnO_2-C composite and C-Fe/PANI/Ni-GF electrode materials were investigated for supercapacitor applications. The birnessite-type MnO_2-C composite with hierarchical nanostructures was successfully synthesized using $KMnO_4$ solution and spent printing carbon grains. The C-Fe/PANI/Ni-GF electrode material was successfully synthesized by pasting a mixture of iron-polyaniline (Fe/PANI) on nickel graphene foam (Ni-GF) and carbonized under the nitrogen.

The structural, morphological and compositional characterization of the as-synthesized electrode materials was carried out using scanning electron microscopy (SEM) and transmission electron microscopy (TEM) for morphology, energy-dispersive X-ray spectrometer (EDS) for elemental composition of the sample, X-ray diffraction (XRD) for crystal structure analysis, Raman spectroscopy for information on chemical structures, and X-ray photoelectron spectroscopy (XPS) for the elemental composition and chemical state of the elements within a sample.

The SEM images of the C-Fe/PANI/Ni-GF samples showed agglomerated nanograins. TEM images showed Fe/PANI on graphene foam (GF) which was grown on Ni substrate. EDS further confirmed the main elements of the sample (C, N, O, S, Fe and Ni). The XRD analysis of the as-synthesized C-Fe/PANI electrode material confirmed the diffraction peaks of Fe-compounds (Fe_3C, FeS, Fe) and (002) graphitic plane. The Raman spectroscopy of C-Fe/PANI/Ni-GF revealed features of the graphitized carbon material and Fe-PANI functional

groups. The XPS analysis confirmed the presence of Fe^{3+} and Fe^{2+} oxidation states in the samples which could be mainly due to iron-carbide, iron-sulfide and iron-nitride configurations. Similarly, the SEM images of the MnO_2-C composite sample showed combined morphology of nanowires and microsponges (sponge-like hierarchical nanostructures). EDS confirmed the main elements of the sample Mn, O and K, and a significant amount of C. XRD displayed characteristic peaks of MnO_2-C composite. Raman spectra showed the characteristic vibration bands of MnO_2-C composite, and D and G peaks confirmed the presence of carbon traces. The XPS analysis confirmed the core level spectra of C 1s, K 2p, Mn 2p, and O 1s obtained from the as-prepared MnO_2-C composite.

The electrochemical properties of the C-Fe/PANI/Ni-GF electrode were evaluated in a three-electrode configuration in both positive and negative potential window using 1 M $NaNO_3$ electrolyte and C-Fe/PANI/Ni-GF//C-Fe/PANI/Ni-GF symmetric device was successfully fabricated. The electrochemical properties of the working electrodes (birnessite-type MnO_2/carbon composite and C-Fe/PANI/Ni-GF) were evaluated in a three-electrode configuration using 2.5 M KNO_3 electrolyte, and MnO_2-C//C-Fe/PANI/Ni-GF asymmetric device based on MnO_2-C composite as positive electrode and C-Fe/PANI/Ni-GF as negative electrodes was successfully fabricated. Both devices (symmetric and asymmetric) showed excellent electrochemical performance.

5.2 Future work

Future research is necessary to fully explore the materials in this study to improve their properties. The materials can be explored further in other electrolytes, such as organic and ionic liquid electrolytes, to improve the specific energy and specific power of the materials and increase the operating voltage window. Explore different conducting substrates other than Ni foam to understand the role of the current collector in improving the SCs performance.